Quantum dot bioconjugates for the detection of extracellular vesicles in saliva and breath

Author:

Garima Dobhal

Supervisors:

Prof. Thomas Nann and Dr. Renee Goreham

A thesis submitted in fulfillment of the requirements

for the degree of Masters of Science

in Chemistry

at

Victoria University of Wellington

2019

Abstract

Nano-sized extracellular vesicles, released by most types of cells, contain information about the cell they originate from and have been shown to be involved in a variety of cellular processes. However, their detection and characterisation has been challenging and non-standardised, which makes comparisons across literature very challenging. While exosomes are known to exist in complex biological fluids such as saliva, breast milk, blood, and urine, their separation and identification from these media are time-consuming. Many researchers use techniques such as transmission electron microscopy for physical characterisation and western blot for protein identification, which are often not available in medical settings. Additionally, while these fluids can be easily obtained, acquiring similar samples from lung environments is a highly invasive procedure. While breath is known to transmit droplets from the lungs, the presence of exosomes in these condensates is unknown. In this project, functionalised InP/ZnS quantum dots (QDs) were used to target exosomes from a number of biological sources and provide a gateway to more fully characterise their ensemble properties. The InP/ZnS QDs were synthesised, and their size dependency on the band gap was investigated in accordance with the theoretical effective mass approximation model for quantum dots. The QDs were produced with hydrophobic oleylamine ligands, and therefore had to be ligand exchanged to be used in biological applications. A range of ligand exchange methods was surveyed to probe the best balance between retention of original quantum yields and best colloidal stability in aqueous systems.The QDs were further conjugated to an antibody specific for CD63, the protein found on exosomes. The conjugation was confirmed using dynamic light scattering and surface plasmon resonance. Finally, the binding of the QD-Antibody probe to the exosome was confirmed using surface plasmon resonance and confocal microscopy. Further modifications of the assay system could lead to multiplex-detection of the different proteins on the exosomes, their characterisation, and a method for the rapid detection of diseases.

Acknowledgements

I would like to acknowledge my supervisors Prof. Thomas Nann and Dr. Renee Goreham firstly. Without your help and constant encouragement, this thesis would probably not be complete. I will always appreciate the fact that the two of you were readily available to talk whenever, and have helped me aim a lot higher than I did previously.

I would like to acknowledge Geoffry Laufersky for the help with just about everything I needed help with which included the synthesis of the InP/ZnS quantum dots and the estimation of their shape using his modelling worksheet. Thanks also for reading and editing my thesis as harshly as possible, it was super useful and I do not know what I would do without you!

I would also like to thank Zeineb, for helping me work out how to use the flow cytometer, and your advice on this project and general TEMing was very invaluable. I would like to thank Deanna Ayupova for the THP-1 exosomes and doing the cell culture to isolate these.

The people in the SCPS department also helped me out in so many different ways. David Flynn, the TEM expert, your knowledge about microscopy and the machines are absolutely invaluable. Further to this, you were always available to answer questions and solve problems or just give me amazing coffee. Rachel Wallace, the chats we had and your constant help and openness was very much needed and appreciated.

The entirety of the Nann group was an amazing support system to have - Zeineb, Amrita, Jacob, Rohan, Nicolo, Shalini, Erin, Vaibhav, Fraser, Kathryn, and Sam. The group meetings were always something I looked forward to and getting advice about the use of equipment and other processes was something I would probably have picked up a lot slower if it was not for all of you. The chats in the lab about everything ranging from science to music to life stuff also helped get through all the stresses of things not working in the lab.

I would like to thank all of my family and friends for being amazing but specifically, to my mum and my dad for being the biggest support system I could possibly

ask for. You gave me the freedom to choose what I wanted and have always supported all my decisions and for that, I am grateful. Also, to my best friend, Ryan, I love complaining and you listened patiently (most of the time). To Amanda, for the great chats and being a generally great friend.

Finally, I would like to thank the Curtis Gordon Scholarship for funding me.

Further resources and funding for this project were provided by the Victoria University of Wellington and the MacDiarmid Institute for Advanced Materials and Nanotechnology.

Contents

List of Figures

List of Tables

List of Abbreviations

AAS	**A**tomic **A**bsorption **S**pectroscopy
Ab	**A**nti**b**ody
ATR	**A**ttenuated **T**otal **R**eflectance
DFT	**D**ensity **F**unctional **T**heory
DHLA	**Di**hydro**l**ipoic **A**cid
DLS	**D**ynamic **L**ight **S**cattering
DMSA	**Di****m**ercapto**s**uccinic **A**cid
DMSO	**Di****m**ethyl **S**ulf**o**xide
DNA	**D**eoxyribo**n**ucleic **A**cid
EBC	**E**xhaled **B**reath **C**ondensate
EDA	**E**thylene**di****a**mine
EDC	1-**E**thyl-3-(3-**d**imethylaminopropyl)**c**arbodiimide
EDS	**E**nergy **D**ispersive X-ray **S**pectroscopy
EMA	**E**ffective **M**ass **A**pproximation
EV	**E**xtracellular **V**esicle
FTIR	**F**ourier-**T**ransform **I**nfrared **S**pectroscopy
FWHM	**F**ull-**W**idth **H**alf-**M**aximum
HRTEM	**H**igh-**R**esolution **T**ransmission **E**lectron **M**icroscopy
ICPMS	**I**nductively **C**oupled **P**lasma **M**ass **S**pectrometry
InP/ZnS	**In**dium **P**hosphide/ **Z**inc **S**ulfide
miRNA	**Mi**cro **R**ibo**n**ucleic **A**cid
MPA	**M**ercapto**p**ropionic **A**cid
MSA	**M**ercapto**s**uccinic **A**cid
MUA	**M**ercapto**u**ndecanoic **A**cid
NHS	***N*-H**ydroxy**s**uccinimide

NMF	*N*-**m**ethyl **f**ormamide
NTA	**N**anoparticle **T**racking **A**nalysis
PEG	**P**olyethylene **g**lycol
PL	**P**hoto**l**uminescence spectroscopy
QCE	**Q**uantum **C**onfinement **E**ffect
QDs	**Q**uantum **D**ots
QD-Ab	**Q**uantum **d**ot-**A**nti**b**ody
QY	**Q**uantum **Y**ield
RNA	**R**ibo**n**ucleic **A**cid
RPS	**R**esistive **P**ulse **S**ensing
SMLM	**S**ingle **M**olecule **L**ocalisation **M**icroscopy
SPR	**S**urface **P**lasmon **R**esonance
STEM	**S**canning **T**ransmission **E**lectron **M**icroscopy
TEM	**T**ransmission **E**lectron **M**icroscopy
TMAH	**T**etramethyl**a**mmonium **h**ydroxide
TOP	**T**ri**o**ctyl**p**hoshine
UV-Vis	**U**ltraviolet-**V**isible
XPS	**X**-ray **P**hotoelectron **S**pectroscopy
XRF	**X**-**r**ay **F**luorescence

Chapter 1

Introduction

1.1 Background

The contents of this chapter have been published elsewhere with contributions from the author.[1]

Extracellular vesicles (EVs) of sizes ranging from 30 - 100 nm are released by different cell types and contain information about the cell they originated from in the form of protein, DNA and RNA.[2] EVs are found in most biological fluids and play a significant role in physiological processes ranging from the elimination of unused proteins from the cells[2] to the transfer of tumour-related information.[3] Therefore, they have the potential to be used as biomarkers for different diseases. Easy analysis and detection remains a challenge as they are difficult to observe with bulk techniques such as flow cytometry, dynamic light scattering and nanoparticle tracking analysis. Using fluorescent quantum dots (QDs) for their detection and characterisation is beneficial due to the wide array of sensor systems that can be incorporated with the dots.[4] However, the literature around QDs used for targeting purposes focuses on QDs made from toxic materials such as Cd or Pb. The focus of this thesis was on the synthesis and ligand exchange of indium phosphide with zinc sulfide shell (InP/ZnS) QDs and their application in biomedical therapeutics, in particular for targeting EVs.

1.2 Extracellular vesicles (EVs) as biomarkers

EVs are released by many different types of healthy and cancerous cells in the body, such as B lymphocytes, dendritic cells, platelets, neurons, and intestinal epithelial cells.[5,6] Different types of EVs are known to originate from a given cell, with the differences between them arising through size and their biogenesis. Exosomes are a type of EV that occur in the size range of 30 – 100 nm with a plasma membrane and they contain a specific set of information in the form of ribonucleic acid (RNA), deoxyribonucleic acid (DNA), lipids, and proteins. They have been shown to be involved in intercellular communication because they are able to enter other cells through the process of endocytosis.[3] These small EVs have been isolated from biological fluids such as blood plasma,[7] urine,[8,9] saliva,[6] breast milk,[10] and amniotic

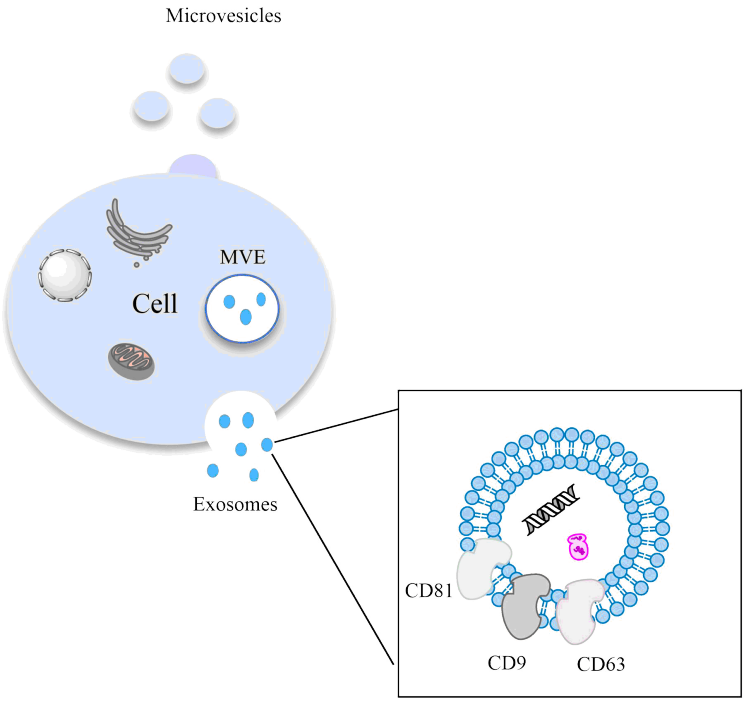

FIGURE 1.1: Exosome and microvesicle formation and (inset) proteins on the membrane of exosome.

fluid.[9] Their content is also affected by diseases such as asthma, allergy, cancer, and neurodegenerative diseases. Therefore, they have the potential to be biomarkers for disease.[11,12]

Exosomes are formed within the cell as intraluminal vesicles which then bud into multivesicular endosomes (MVE) and exit the cell with a part of the plasma membrane.[5] Another type of EV is the microvesicle that forms from the direct outward budding of the plasma membrane. The latter tend to be larger in size (>100 nm) and there is some evidence that their functions differ from that of exosomes (Figure 1.1) .[6] Due to the complex differences between exosomes and microvesicles and the significant overlap with the size range these vesicles can exist in, vesicles smaller than 100 nm will be called exosomes in this thesis. This is because the size of exosomes is said to be about the size of the MVEs that they originate from which is between 30-100 nm.[13] It is important to correctly differentiate between the two because it is possible that smaller vesicles may bud from the membrane; however, the investigation of their biogenesis is not within the scope of this thesis.[13]

The target and capture of all EVs is the first step towards an overall characterisation of protein expression and identification of disease-related EVs in a biological sample. The isolation of exosomes from complex fluids such as blood plasma, saliva, breast milk, and urine tends to be more complicated, as it is difficult to remove contaminants such as cells, proteins, and general debris. The origin of the EVs that are isolated from biological fluids is also not known because these usually contain a mixture of different cell types.[14] The majority of studies use EVs isolated from cell cultures to specifically examine those that originate from a single cell type.[7] Studies have shown that the proteins embedded in their plasma membranes can be targeted for characterisation and isolation, with CD63 and CD81 being the most well-known.[5] Therefore, the use of a molecule with high specificity for those proteins, such as an antibody (Ab) or an aptamer, can make it possible to target these proteins. Combining one of these with a fluorophore can further enable an easier way to observe the EVs based on their movement using live-cell microscopy.

1.2.1 EVs in biological fluids

The presence of EVs in complex biological fluids such as plasma and saliva merits the question of whether EVs can be derived from exhaled breath. As breath is a very non-invasive method of collecting a biological sample, it could help with the detection of lung-derived air and could further be used to detect lung diseases. Pinkerton *et al.* collected exhaled breath condensate (EBC) from individuals with chronic obstructive pulmonary disease and asthma as well as EBC from healthy individuals.[15] They were able to show the presence of micro ribonucleic acid (miRNA) in EBC and showed the difference between miRNA expression in healthy individuals and individuals with inflamed lungs.[15] Micro-RNA are small non-coding RNA molecules that play a significant role in post-transcription processes.[15] The presence of miRNA in EBC could therefore originate from two sources - either free miRNA or miRNA contained within vesicles. Along these lines, EVs further serve the purpose of being a stable method of transport to avoid exposure to RNAase.[13] A difference in miRNA expression levels has also been demonstrated between healthy patients and patients with non-small-cell-lung-cancer using exhaled breath.[16] Sinha *et al.* were

able to show that the miRNA in exhaled breath was predominantly in a membrane-enclosed form.[17] They found that exosomes were present in EBC with the use of latex beads coated with the anti-CD63 Ab which was then pelleted to separate the exosomal fraction.[17] However, they did not characterise these exosomes sufficiently. Their characterisation included coating latex beads with an anti-CD63 Ab incubated with concentrated EBC, and then measuring this using flow cytometry. In a separate experiment, the beads were incubated with the cell culture supernatant of THP-1 cells, and then the proteins associated with this were detected. This was used as a confirmation of the effectiveness of the beads in isolating exosomes. However, latex beads can adsorb anything biological such as proteins other than CD63 due to the spontaneous reaction between an aldehyde (on the beads) and amine (on the proteins). The above method used does not confirm the presence of exosomes. Furthermore, due to exosomes budding from the membrane of cells, the same proteins that are found on the surface of the exosomes can be found on the surface of the cells.[5] Additional strategies such as microscopy should have also been used to confirm the presence of the EBC derived EVs.

While EVs from lungs have not been identified, EBC might contain some as is evident from the literature discussed above. Because the EVs in saliva are well studied, we anticipate that their isolation methods may be applicable to EBC. The isolation of exosomes from biological fluids such as saliva has been optimised.[11] The generally accepted method of isolation of salivary exosomes is ultracentrifugation, however this method leads to lower purity, albeit higher concentration, of the resulting exosomal fraction and requires the use of expensive equipment.[18] Conversely, the use of commercial size columns such as the qEV (Izon Science Ltd.) has proven to be a quicker method to obtain pure exosome isolates with minimal effect on the exosome structure.[19] Furthermore, exosome precipitation kits such as ExoQuick (System Biosciences Ltd.) and Rosetta Exolute (Rosetta Exosome Inc.) are also alternative methods of isolation that have advantages based on the concentration and purity of the resulting sample.[20,21] The structural characterisation of exosomes in human saliva was done using techniques such as atomic force microscopy (AFM).[6,22] Sharma *et al.* were able to show that cancer exosomes exhibit significantly higher CD63 surface densities compared to normal exosomes using an anti-CD63 Ab-functionalised AFM

tip.[22] Therefore, the processes used to target exosomes in saliva could be transferred and applied to target exosomes in EBC. Finally, EBC could be used as a source of exosomes to detect lung diseases as it is a matrix of biomarkers and could contain EVs.

1.2.2 Methods of characterisation of exosomes

The presence of exosomes within EBC was suggested using a single method in literature.[17] However, there needs to be further characterisation of EBC exosomes to confirm their presence, concentration, and size distribution. There is a suite of methods available for the characterisation of EVs however, obtaining quantitative data about their size and concentration is difficult because of how heterogenous the population is.[23]

Flow cytometry

Flow cytometry is a technique that is used for counting and separating cells* according to their markers by utilising light scattering around the particle and particle fluorescence.[24] Fluid cell samples are flowed through a flow cytometer and passed through a laser beam. Size distribution and cell concentration can be quantified using the direction of the scattered light.[24] This is because the intensity of the forward scattered light is proportional to the diameter of the particle. There are two different types of scattering that are measured - forward and side. If the refractive index and structure information of the particles of interest is known, the side scattering signal can give important data for smaller objects (like EVs).[24,25] Most conventional flow cytometers have a lower detection limit of 300-500 nm which would give inaccurate data with respect to smaller particles that are of interest in this thesis. It is possible to tag the exosomes with fluorescent dyes however, to utilise the fluorescence detection ability of the flow cytometers. Stoner *et al.* showed that the voltage sensing dye, di-8-ANEPPS, could be used to accurately detect subpopulations of EVs and their size. Using an antibody, it was also shown to be possible to quantify the surface

*for cells with a diameter < 1 µm

markers on the EVs.[26] The effect of the dye attachment on the vesicle structure was not explored.

Dynamic Light Scattering (DLS)

A method commonly used for characterisation of EVs, DLS is used to determine relative size and size distribution of sub-micron sized particles suspended in a fluid. The Brownian movement of particles is defined by their collisions with solvent molecules. Brownian motion causes changes in light scattered, which is proportional to the hydrodynamic size of the particles. Therefore, a sample with monodisperse particles can be measured with ease using DLS.[24] However, polydisperse samples give rise to inaccurate results with high polydispersity indices. Despite this, several studies use DLS to characterise EVs.[27,28]

Nanoparticle Tracking Analysis (NTA)

NTA is used to detect and visualise particles of sizes between 50 nm and 1 µm. The particles are visualised with an optical microscope using the intensity of light they scatter.[24,25] The use of NTA is also plagued by inaccuracies related to smaller particles not unlike DLS, however it has been used to detect exosomes and other extracellular vesicles frequently.[24]

Resistive Pulse Sensing (RPS)

RPS is an electrical technique capable of determining size and concentration of an EV sample.[25] A RPS setup is based on the Coulter principle and contains two chambers with an electrolyte separated by a conductive aperture. As nanoparticles flow through this aperture, a change in conductance is observed, which can be related to the particle volume and therefore, the size.[25] The qNANO, a commercially available device, uses an elastic tunable pore that measures the drop in current.[25] However, this technique also sees limitations. For example, it is possible use smaller pores to measure smaller particles, however clogging of the instrument is possible with high protein or other debris. Another problem is that damaged membranes can lead to false values of conductivities.

Transmission Electron Microscopy (TEM)

Information about size, structure and morphology of the EVs can be obtained using TEM.[24,25] In electron microscopy, an image is formed using a beam of electrons that is transmitted through the sample. The image can be photographed with a camera. As electrons can be deflected, TEM is done in vacuum. This also means that the sample cannot be aqueous and needs to be dried. This has been shown to affect the morphology of the EVs wherein Chernyshev *et al.* showed distinct differences between hydrated and dehydrated EVs.[29] A high enough concentration of EVs is also ideally needed to be able to find them under the microscope. Additionally, biological samples are usually stained using a dye such as uranyl acetate to allow for contrast on a carbon-coated grid.

Atomic Force Microscopy (AFM)

AFM is an imaging technique that can be used to obtain size, elasticity, surface topography information.[25] A sharp tip is used to measure the feedback from its interaction with the particle. There are two main modes used in AFM: scanning and tapping. In the scanning mode, the tip is dragged over the surface of the sample. The movement of the cantilever (attached to the tip) is measured using laser deflection from the initially pre-set deflection value. Then, a certain voltage is applied to return the laser to its original deflection value. This voltage is a measure of the topography of the sample's surface. However, the tip creates friction when scanning thereby damaging the sample. Conversely, the tapping mode is recommended for biological samples such as EVs. The cantilever is oscillated at a certain amplitude vertically. A difference in the amplitude created by the tip's interaction with the surface of the sample is used to map the topography.[30] The substructure of human saliva exosomes was imaged using AFM with better resolution than TEM.[31] Aqueous samples can be measured on AFM but, obtaining statistically quantitative size results is a major limitation.[25]

1.2.3 Molecules for exosome capture

The various markers embedded in the exosome membrane can be targeted using molecules like antibodies, DNA, or RNA nucleotides. For example, the CD63 and CD9 proteins can be targeted using anti-CD63 and anti-CD9 proteins, respectively, and these are readily available commercially.[17] Antibodies are large, Y-shaped proteins and are also known as immunoglobins. They are produced by plasma cells and used by the immune system to target foreign antigens and neutralise them. Antibodies consist of 4 polypeptides – 2 heavy and 2 light chains. The variable region of the Ab is between the two short arms of the "Y" and is what gives it specificity for antigen binding.

The use of antibodies for targeting bulk exosome populations, and subsequently, the capture of cancer-related exosomes, has been demonstrated multiple times.[27,32,33] Usually, the antibodies can be immobilised on a detection platform, such as surface plasmon resonance (SPR)[32] substrate, but they can also be conjugated to nanoparticles.[33] As an Ab has primary amines and sulfhydryls, these can be used for conjugation to a fluorescent material such as QDs.

Aptamers are another kind of biomolecule used frequently for targeting of proteins and other bio-structures, and detection.[34,35] Similar to the Ab, they can be made specific to a target molecule. Aptamers are single-stranded DNA molecules also known as oligonucleotides. They are synthesised through rounds of selection and optimisation from a random sequence pool, but they have also been found to exist naturally. Aptamers tend to be smaller than antibodies, which can be advantageous as they will retain the small size of a QD conjugated to an aptamer, however, they can also degrade quite easily *in vivo* due to the presence of nucleases. This does not limit their use outside of the body. Aptamers also have high specificity but can target molecules with a similar structure. They tend to be cheaper than antibodies. Similar to an Ab, aptamers can also be conjugated to nanoparticles or immobilised to a surface.[36] For example, Jiang *et al.* showed the use of aptamers (specific to exosomes) to complex and stabilise gold nanoparticles in high salt concentrations.[37] The higher specificity of the aptamer for exosomes caused the gold nanoparticles to aggregate in the presence of exosomes leading to a colourimetric sensor. They also extended

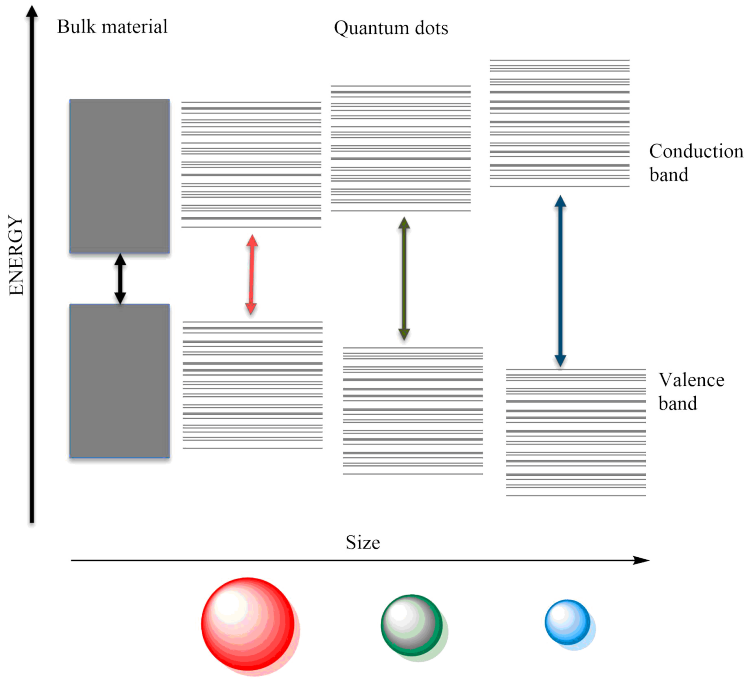

FIGURE 1.2: Quantum confinement effect demonstrated by the quantum dots that relates to the size of the band gap.

the multiplexing ability of their sensor to create a profiling platform for the different protein markers on the exosome.[37]

Here, we used the amine groups on the Ab and aptamer for conjugation to carboxyl-terminated QDs and further used these fluorescently-bound biomolecules to target exosomes in solution.

1.3 Quantum dots (QDs) as fluorescent probes

QDs are fluorescent, semiconducting nanoparticles that have a diameter typically ranging from 2-10 nm.[38] They consist of a core made out of CdS, CdSe, CdTe, InP, InAs, or PbSe, depending on the emission and application desired. Many syntheses also produce a wide bandgap shell, commonly ZnS, which is known to enhance the quantum yield (QY) of the QD sample synthesised, protect the core from oxidation, and can remove surface traps by passivating the core.[39]

Due to their small size, QDs exhibit quantum confinement effects (QCE) wherein a decrease in particle radius from the bulk exciton Bohr radius causes a change from continuous energy levels seen in the bulk to a discretisation or quantisation of the

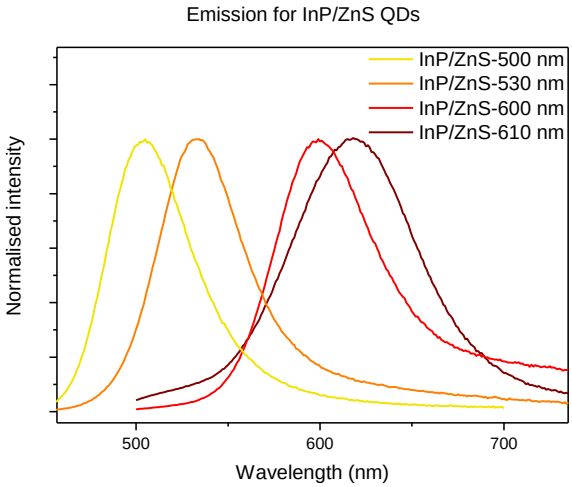

FIGURE 1.3: Emission spectra of different-sized QDs

energy levels. This means the optical properties of QDs differ from bulk material properties, and can be tuned based on how large or small the particles are, which can be seen in Figure 1.2. As the size of the nanoparticle decreases, the confinement strengthens and the transition energy between the valence and conduction band increases. This means that the QD emission wavelengths depend (non-linearly) on their size; with decreasing size comes increasing confinement (blue-shifted emission spectra), therefore allowing the tunability of emission wavelengths (Figure 1.3).[38]

QDs hold several advantages over organic dyes. The latter are prone to photobleaching, causing a rapid loss of fluorescence in high-intensity imaging studies such as confocal microscopy.[38,40] They have broad emission, which can make multi-parameter studies difficult.[4] In comparison, QDs have beneficial optical properties, like a narrow emission spectra.[38] The more advanced architectures of the QDs coupled with ligands and biomolecules can also be more stable than organic dyes, as a core/shell structure can prevent particle degradation over time.[38]

Functionalisation with any molecule of choice onto the QDs is also possible due to their surface ligands. Ligands are molecules that can coordinate to the surface of the QD, and based on the terminal functional group (either a carboxylic acid, amine or thiol) on the ligand, further chemistry can be conducted to enable functionalisation or conjugation to target-specific biomolecules and their use in fluorescence microscopy and bioimaging.[41]

Despite the known toxic nature of cadmium, bioimaging research has normally utilised cadmium-based QDs.[33,42,43] They are highly researched materials, so syntheses can produce samples that have narrow spectral full width at half maximum (FWHM) and high QYs. FWHM are used as a direct measure of size distribution of the nanoparticle sample due to the relationship between the size and the emission wavelength. Therefore, a narrow FWHM can be related to a more monodisperse sample. While cadmium is toxic to living organisms.,[44] the use of a ZnS shell can prevent the leaching of Cd^{2+} ions inside the body. The toxicity of cadmium also depends on the size of the QD as it was shown that 50% of the smaller Cd-based QDs (less than 6 nm diameter) will clear renally within 4 h.[45] In a comparison of toxicity of CdSe/ZnS QDs with InP/ZnS QDs, it was shown that while both the materials can leach core contents, indium's lower toxicity makes these QDs a safer alternative.[46,47]

1.3.1 InP QDs

InP QDs are potential candidates for the cadmium-free route, however their synthesis involves the use of unstable precursors and results in products that are easily oxidised.[48] QDs are generally prepared using high-temperature hot-injection syntheses, which has led to a search for suitably reactive phosphorus precursors as sources for P^{3-} which can result in QDs with a high QY and high stability without total decomposition of the phosphorus precursors.[49] More specifically, various phosphorus precursors like tris(trimethylsilyl)-phosphine[50] and phosphine (PH_3)[51] have been used and show good results with respect to size tunability. However, $P(TMS)_3$ is pyrophoric and PH_3 is a toxic gas. Therefore, these are difficult and often dangerous to handle. This problem was solved with the tris(dialkylamino)phosphine and indium halide precursors.[52,53] Further improvements of the syntheses using these phosphines has allowed for InP QDs with reported QYs that are higher than 55%[54] and improvements in size tunability.

Due to the high temperatures (of up to $\sim$300 °C) required in the syntheses of the QDs, a suitable coordinating solvent with high boiling points needs to be used.[53] Oleylamine is a popular choice for a solvent, however being largely nonpolar, it is

readily dispersed in organic solvents such as toluene and hexane. This renders the QDs hydrophobic, and will result in aggregation in aqueous environments. Therefore, they need to be chemically modified to become water-soluble for biomedical applications.

1.3.2 Water solubilisation and ligand exchange

Methods to obtain water-soluble QDs include replacing the original, hydrophobic ligands for hydrophilic ones or using ampiphillic polymers coats the surface of the particle with their nonpolar sides and exposes a hydrophilic functionality with the other. While it tends to preserve their photoluminescent properties, the polymer method causes the hydrodynamic radius of the QD to increase significantly.[38] As opposed to this, the ligand exchange strategy uses small molecule ligands which can retain the compact size of the QD. However, this strategy has disadvantages because the QYs significantly decrease due to a change in the surface properties. The resulting QDs are also often prone to aggregation if an incomplete ligand exchange occurs.[55]

Ideally, an efficient ligand exchange would replace all the ligands on the QD surface with the new ligands. However, if this is impeded, it can result in the trapping of the QDs at a phase boundary and poor water solubility. Furthermore, there is usually a decrease in the QY of the QDs by at least a factor of 2.[56] A lot of research efforts have therefore been involved in searching for an efficient ligand exchange strategy that can offer stable QDs that retain their QY.[56–58]

Mercaptocarboxylic acids are a popular class of ligands used to render the InP/ZnS QDs water soluble.[38] (Figure 1.4) These molecules have both a thiol and a carboxylic acid functionality, which should have affinities for the nanoparticle surface and biomolecules, respectively. However, free thiols may not react with the ZnS shell and need to be deprotonated using a basic reaction environment. This enhances the reactivity of the thiol group which can then coordinate to the ZnS shell.[59] Therefore, a number of single-step ligand exchange strategies use a base like tetramethylammonium hydroxide or ammonium hydroxide to control the pH.[41,59]

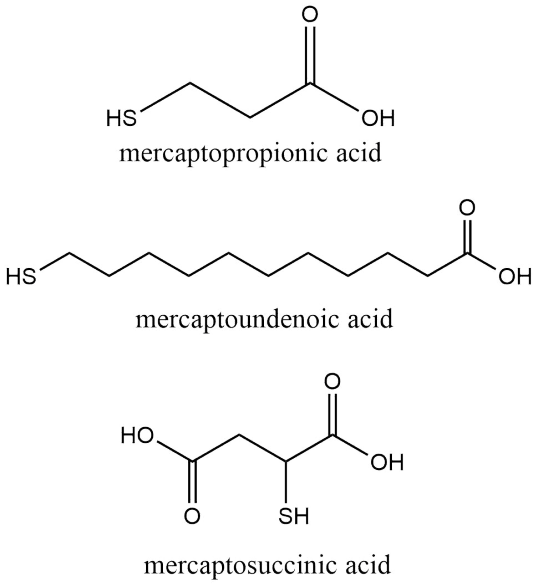

FIGURE 1.4: Different mercaptocarboxylic acids used for ligand exchanges

The use of ammonium hydroxide as a reagent and mercaptosuccinic acid as the ligand with InP/ZnS QDs has been shown to be effective.[41] This does however, cause a drop by about 40% in the QY. This is because the ammonium hydroxide can lead to surface etching despite the thiolated anion's ability to replace the original ligands.[56,58] Enhanced QY and more stable water-soluble QDs were reported with the use of Zn-mercaptocarboxylic acid/DHLA complexes which were made by mixing sodium hydroxide, zinc nitrate, and the desired ligand. They attribute this enhancement of optical properties to a reaction between the zinc complex and the original ligands (tetradecylphosphonic acid and trioctylphosphine oxide) on the QD surface that enables their gentle removal.[58]

The issues that arise with a ligand exchange done in a single step like the ones above can be attributed to the competition between the original ligands and the new ligands and their interaction with the solvent for a site on the surface of the QD. Ligand exchanges like these all introduce the final solvent (water) with the final ligand to the solution. This results in an incomplete ligand exchange because the process of absorption and desorption of the initial, sterically demanding oleylamine ligands is rapid at room temperature and this competes with the new, incoming ligands.[60]

To achieve a more complete ligand exchange, a two-step method can prove to be more beneficial as the crucial step for this is the introduction of a new (anti-)solvent and an intermediate, metastable ligand. The metastable ligand can replace the oleylamine ligand (similar to single-step) however, the introduction of a new anti-solvent accelerates the rate of exchange by precipitating the QDs into a new phase and aiding in the removal of oleylamine (which is not soluble in the anti-solvent). The anti-solvent therefore, creates favourable conditions for the new metastable ligand. The precipitate can then be redispersed in water, and the metastable ligand can be exchanged rapidly with the final ligand, which should be more stable.

Yung *et al.* reported a two-step ligand exchange strategy using ethylenediamine (EDA) that was easily adaptable with various mercapto-ligands such as mercaptosuccinic acid (MSA), mercaptoundenoic acid (MUA), mercaptopropionic acid (MPA) as well as dithiol ligands such as dihydrolipoic acid (DHLA) using CdSe QDs.[56] Their strategy involved the stripping off of the original ligands by EDA and the subsequent replacement of EDA with stronger mercaptocarboxylic acid ligands. This strategy saw a drop in QY from 60% to 35% with the use of MSA and a QD that fluoresced at 601 nm.

Further application of this two-step method is seen in the literature with the ligand exchange using iron oxide nanocubes[61] and PbSe nanocrystals.[62] With the iron oxide nanocubes, the nitrosyl tetrafluoroborate ($NOBF_4$) in dimethylformamide (DMF) was used to destabilise the organic ligands on the surface of the nanocubes. An alternate strategy was the use of dimercaptosuccinic acid (DMSA) and dimethyl sulfoxide (DMSO) which worked better due to the slight increase in acidity and the subsequent protonation of the organic ligands causing a more permanent and complete exchange of ligands. Both these strategies worked well for the iron oxide nanocubes but the $NOBF_4$ salt is corrosive, volatile, and forms nitrous acid when in contact with water. The DMSA/DMSO method is slightly gentler, however it uses DMSO which has been known to negatively affect cells and is difficult to get rid of due to its high boiling point (189 °C).[57,61]

As opposed to this, a gentler alternative method was presented recently, which used an ammonium halide in a mixture of *N*-methylformamide (NMF) and acetone

for the ligand exchange of CdSe[63] and PbSe[64] nanocrystals in hexane. These combinations were shaken and particles precipitated out as usual. After this, the precipitate was redispersed in NMF and washed with acetone to get rid of any unreacted ammonium halide and the organic ligands. The halide replaces the organic ligands and it was initially found that halide-capped nanocrystals dispersed in polar (non-aqueous) solvents showed good electronic properties. *N*-butylamine was then used to precipitate the halide-capped nanocrystals from the polar solvent while preserving the inorganic halide capping. Here, the *n*-butylamine works as a co-ligand that allows the nanocrystals to be precipitated in non-polar solvents such as chloroform and toluene. As *n*-butylamine is labile, it could be exchanged with a thiolated ligand with a carboxylic acid functionality to render the nanocrystals hydrophilic.[63,65]

1.4 QD-Biomolecule conjugates

A popular bioconjugation method is one that uses 1-ethyl-3-(3-dimethylaminopropyl) carbodiimide (EDC) and *N*-hydroxysuccinimide (NHS) ester (Figure 1.5). This method covalently bonds a carboxylic acid (obtained as structure **1** in Figure 1.5 via ligand exchange of the original oleylamine ligands with MSA) to a primary amine *via* a peptide bond, so can allow the binding of a primary amine of the biomolecule to the acid-terminated QD surface. However, this reaction is non-specific and there is potential for loss of antigen binding ability if the QD attaches to the active sites.[66] While NHS is not strictly necessary,[41] the intermediate can react with water to form the starting material **1** again, which is kinetically favoured. On the other hand, using NHS along with EDC aids in achieving higher yields of the conjugate by reacting with and stabilising intermediate **2** to form **4** which can then react with a primary amine to yield the bioconjugate, **3**.[67]

QD-Ab conjugates have been quite popular for specific imaging studies.[4,68] In this capacity, long-term imaging of live cells can be made possible.[69] InP/ZnS QD-Ab conjugates were used to image pancreatic cancer using specific cancer markers.[41] QD-Ab conjugates can also be incorporated into sensor systems such as an immunochromatography test strip.[70] and an novel-ELISA like assay.[71] The smaller size

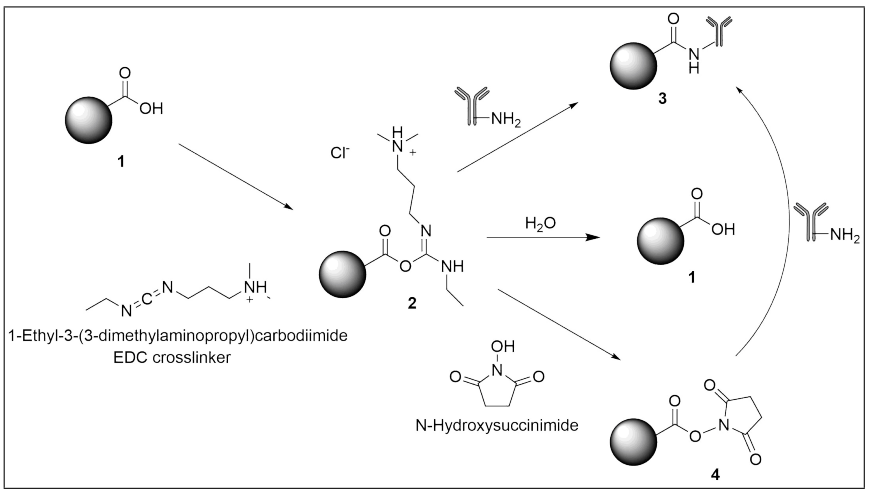

FIGURE 1.5: EDC/NHS coupling mechanism

of aptamers enables a QD-Aptamer conjugate to be further used for FRET-based sensors.[72]

1.5 Detection and capture of exosomes using QD-biomolecules

Exosomes and microvesicles isolated from saliva have been shown to be potentially useful for the detection of diseases like pancreatic cancer[12] and head and neck cancer.[6] Sina *et al.* were able to construct a sensing platform that could quantify the amount of disease-specific exosomes using spectral shifts in the surface plasmon resonance (SPR) of a gold substrate with bound exosomes. In their setup, an exosome-specific Ab (anti-CD63 or anti-CD9) was immobilised on a SPR gold chip. This Ab captured all exosomes in their sample which changed the mass on the surface and led to the first resonance shift. These bound exosomes were then exposed to a second Ab that was breast-cancer specific, which further shifted the SPR. This could then be used to identify the proportion of all exosomes that were tumor-specific in patient serum samples.[32]

CdSe QDs functionalised with interleukin-13 protein were used to detect cancer-cell derived exosomes. An altered binding pattern was observed when the QDs bound to cancer-cell markers using AFM which could be utilised for the early detection of cancer.[73] While they comprehensively characterised the physical differences in the samples, the changes in optical properties post-binding to the exosome

have not yet been reported and these would be interesting to investigate as well. Electrochemical detection of disease specific exosomes using QDs was also done by Boriachek *et al.*[33]

The capture and identification of all exosomes in a sample can lead to information about all cell- and disease-types in breath.

This work aims to investigate and optimise the ability of the InP/ZnS QDs for their further use in labeling exosomes. Chapter 2 focuses on the synthesis and the characterisation of the QDs, which was done using different methods such as TEM, PL, and UV-Vis. This is followed by concentration studies for the nanoparticles which provides a groundwork for more accurate quantification of the InP QDs. After a suitable ligand exchange (Chapter 3), to result in water-soluble QDs, the QDs were conjugated to biomolecules such as a anti-CD63 Ab and a CD63 aptamer. Subsequently in Chapter 4, these conjugates were applied on pre-isolated cell-culture THP-1 exosomes first, after which they were used for the detection of exosomes isolated from saliva and breath condensate. We probed different methods of confirming the binding of the exosomes to the QDs including TEM, and DLS. The conjugates were also used for confocal microscopy - a technique used by biologists frequently - to show that it is possible to use the QDs as an alternative to fluorophores. The InP/ZnS QDs are also be applied for the accurate detection of exosomes and incorporated into SPR-based systems for the accurate and instantaneous detection of exosomes.

Chapter 2

QD Synthesis and Characterisation

2.1 Synthesis of InP/ZnS quantum dots

The main objective of this work was to synthesise and fully characterise InP/ZnS QDs as a safer alternative to cadmium-based QDs. Specifically, characterising their physical and spectral properties will aid with further studies of these QDs related to the concentration. This information is necessary to enable the most efficient phase transfer and conjugation.

The main synthetic method used for this work yields red-emitting QDs with strong absorption features at 480 nm and 590 nm.[53] These QDs were used in the later chapters involving biological studies because their excitation wavelength of 480 nm is similar to popular dyes used in biological applications such as Fluorescein isothiocyanate (FITC, λ_{exc} = 494 nm), and Alexa-fluor 488 (λ_{exc} = 488 nm). In this chapter, both InP cores and InP/ZnS core/shell materials are examined in order to determine the shell thicknesses and the contributions both have on the final properties of the QDs. The cores for this size are labelled as InP-600 nm, and core/shells are labelled as InP/ZnS-600 nm according to the emission wavelength of the core/shell. Similarly, other sizes of the QDs that were studied include QD-500 nm, QD-530 nm and QD-610 nm, where QD = InP or InP/ZnS for the core and core/shell materials, respectively. A different synthesis protocol was used for these three sizes by Geoffry Laufersky,[54] and they have been further detailed in Appendix A. Their subsequent analysis was then done using physical characterisation methods such PL, UV-Vis absorption, TEM and atomic absorption spectroscopy (AAS).

Generally in the synthesis, oleylamine is used as both a solvent and also a ligand which stabilises the QDs. $InCl_3$ and the tris(diethylamino)phosphine were the indium and phosphorus precursors, respectively. The inclusion of the zinc chloride $(ZnCl)_2$ in the reaction solution was known to improve the size dispersion and prevent surface traps, but it is also possible that it could have lead to the formation of indium-zinc alloys. However, this phenomenon was shown to be unlikely, so it is assumed there is a pure InP core.[52,74] This is difficult to prove using methods such as energy-dispersive X-ray spectroscopy because the core synthesis also involves zinc and therefore, its presence is evident in the sample. To produce the shell of ZnS around the core QDs, equal amounts of a trioctylphosphine-sulfur complex and a

solution of zinc (undecylenate)$_2$ were added to the reaction solution in alternating injections.

The different samples have different synthetic methods, with the QD-500 nm sample being made by changing $InCl_3$ for indium acetate and including cetyltrimethylammonium bromide, a common surfactant for nanoparticle synthesis, into the reaction. Otherwise, all other factors were held the same between the QD-500 nm and QD-600 nm syntheses. The QD-610 nm and QD-530 nm were produced using a 2-pot scheme, where the $ZnCl_2$ and the phosphorus precursor were left to reach equilibrium separately from the indium precursor according to a previously published methodology.[54] Further to this, a non-coordinating solvent octadecene was used with the indium solution to avoid the back-conversion of the zinc and the phosphorus after the hot-injection. Myristic acid was also used to aid in the dissolution of the In^{3+}. The use of octadecene led to QDs that were blue-shifted in the emission spectra, which was the reason this synthesis was used.

The investigation of the physical and optical properties of these materials are described below. Characterisation of QD size distributions and purity using TEM proved to be challenging for reasons that will be covered later in this chapter. While the cadmium alternative is easier to image, InP is a low contrast material and was difficult to discern due to being coated in organic ligands that reduce contrast. Therefore, there was a need to optimise the sample preparation to achieve clearer TEM images.

2.2 Characterisation

The QD-600 nm samples emitted strongly at 600 nm when excited by 480 nm light. This process had a QY of 42.10% and produced an emission peak having a FWHM of 60 nm, which is fairly typical of these syntheses. Figure 2.1(a) shows the absorption and emission profiles of a InP/ZnS sample. The PLQY was calculated using an integrating sphere and a direct excitation method. This is shown in Figure 2.1(b). The scatter region is shown as the higher intensity peak which is higher for the solvent and lower for the sample. A significant drop in QY was observed after 5 months of storage in the dark at room temperature which was down to 25.45%. This has been

previously attributed to a degradation in the shell thickness[74] or loss of ligands over time.[75] Future work would therefore involve investigating the validity of this claim through the use of methods such as thermogravimetric analysis to probe ligand loss.

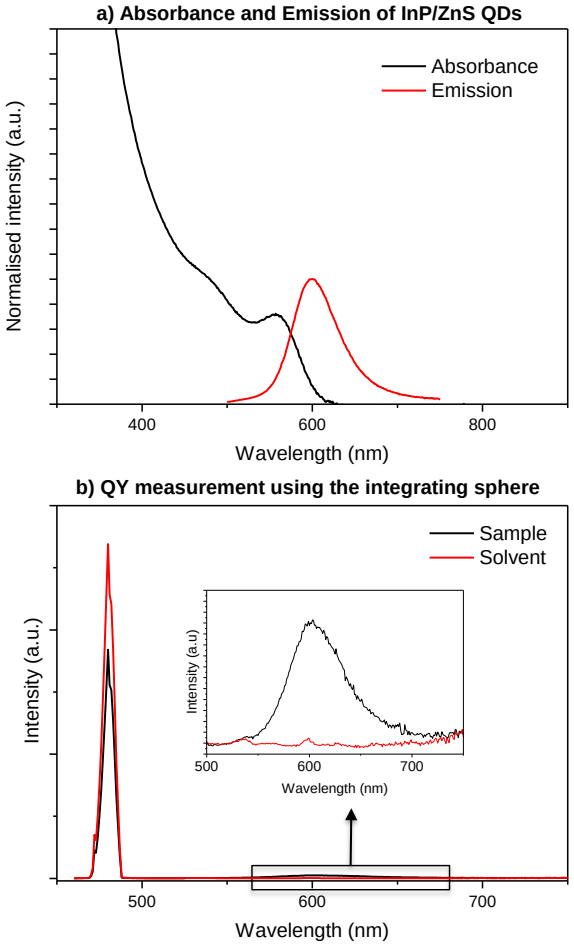

FIGURE 2.1: a) Absorption and emission of InP/ZnS QDs. These were normalised to 1. The PL was run with the excitation wavelength at 480 nm. b) Scatter and emission peaks using an integrating sphere with the solvent and sample spectrum.

Figure 2.2 shows initial TEM images of the particles that are spherical in shape and around 15-25 nm in diameter. This was larger than expected from the synthesis from which the anticipated diameter was about 3.2 nm from literature.[53] Further scanning transmission electron microscopy (STEM) mapping of the QDs (Figure 2.3)

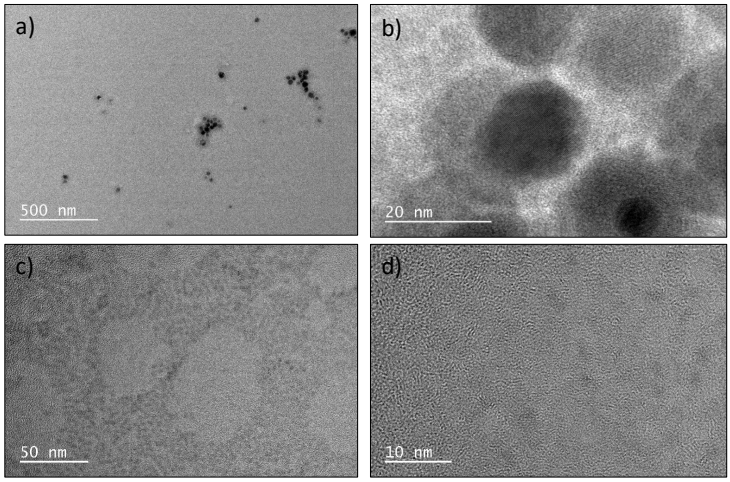

FIGURE 2.2: a) and b) Large spherical particles observed with the TEM of the InP/ZnS QDs. c) and d) Image taken after cleaning the sample using a size column. All four images were taken on the TEM2010.

showed localisation of S, Cl, and Si and high background counts for the other elements. Indium, zinc, and phosphorus are present on these particles but their quantites were not very high. Energy dispersive X-ray spectroscopy (EDS) also confirmed this with high quantities of S and Cl.(Figure 2.4) While S is expected to be present in the final product, the presence of Cl is surprising as the sample was washed using the precipitation/redispersion technique several times. Silicon is a contaminant within the machine, however it also showed localisation on the larger nanoparticles, so this may arise from the grease used to connect the synthesis glassware. In the literature, large agglomerates (of 30-1000 nm) were visible under scanning electron microscopy of CdSe QDs even after 3 cycles of precipitation and redissolution, which typically removes these large groupings.[76] While, the number of aggregates that are visible improves after every cycle step, overusing this traditional method of purification has further been shown to affect the ligand environment by severely depleting the surface coverage on the particles leading to lowered QY and surface defects.[77]

Instead of using this cleaning procedure, the sample was purified again using a size-exclusion column, which is becoming more common in nanoparticle literature.[78] Using this setup, the larger particles should be eluted first, after which the smaller particles and molecules can pass through. The QDs could further be tracked along

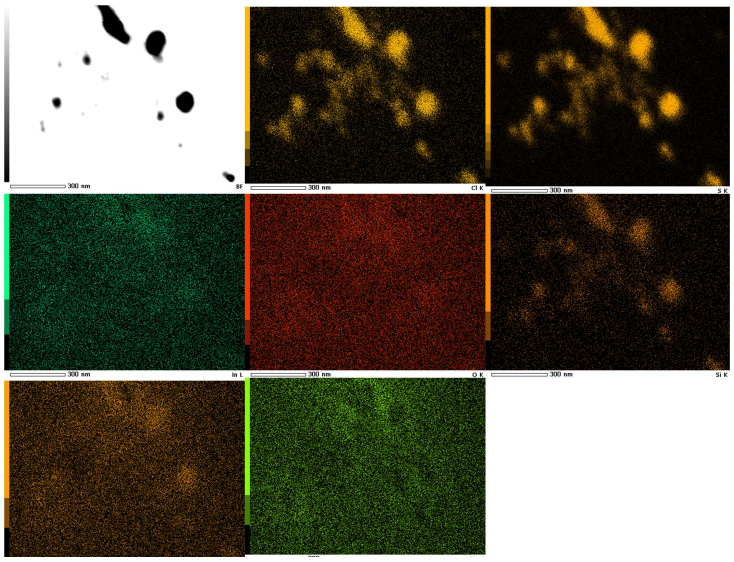

FIGURE 2.3: STEM of the large aggregates visible in the sample on TEM show large quantities of S and Cl.

the size column visually, or using a UV-lamp, and subsequently collected in a vial. However, this method also yields QDs with lowered QY due to the stripping of loosely bound ligands from the surface of the QD. Therefore, this should not be applied to bulk QD sample to be used for further applications. Regardless, this method provided the best balance between good visibility under the TEM and avoidance of any large aggregates, as seen in Figure 2.2(c) and (d).

Better contrast could also be achieved by imaging the QDs on the high-resolution TEM2100F (HRTEM) (Figure 2.8(c)). This enabled characterisation of the size distribution of the QDs, which were around 3.6 nm in their longest dimension. EDS data also showed the presence of In, P, Zn and S with atomic ratios of 0.08, 0.35, 0.42 and 0.14, respectively. EDS is a type of spectroscopy where the sample is hit with a focused electron beam and results in emitted X-rays with element-specific energies. A comparison of the X-ray energy intensities can then yield information about the atomic composition of the sample. It was expected that the In:P ratios would be roughly stoichiometric at 1:1 or metal-rich due to the excess indium precursor present during the synthesis. For similar syntheses, Kim *et al.* was able to show an In:P ratio of 1.32:1 using inductively coupled plasma mass spectrometry (ICP-MS)[79] and Tessier *et al.*'s synthesis yielded QDs with an In:P atom ratios of 4.8:1

Atom ratios of core and core shell QDs						
Sample	In	P	Zn	S	Zn:In	In:P
InP-500 nm	0.13	0.57	0.24	0.06	1.79:1	0.24:1
InP/ZnS-500 nm	0.06	0.39	0.51	0.04	7.89:1	0.16:1
InP-530 nm	0.09	0.64	0.22	0.04	2.41:1	0.14:1
InP/ZnS-530 nm	0.04	0.39	0.40	0.17	9.21:1	0.11:1
InP-600 nm	0.17	0.50	0.16	0.17	0.96:1	0.34:1
InP/ZnS-600 nm	0.08	0.35	0.42	0.14	5.27:1	0.23:1
InP-610 nm	0.09	0.62	0.25	0.03	2.85:1	0.14:1
InP/ZnS-610 nm	0.04	0.44	0.36	0.15	8.26:1	0.10:1

TABLE 2.1: Atom ratios of indium, zinc, phosphorus and sulphur as measured using TEM-EDS.

respectively using X-ray fluorescence analysis.[53] Ignoring precursor mechanics, the maximum amount of phosphorus based on the precursor ratios should be a P:In ratio of 3.6:1. However, the final product (according to EDS) contained roughly 10 times more phosphorus, which was seen across all of the QD samples used. More quantitative analysis of the atomic ratios shows that EDS cannot be used in isolation. This is seen from the AAS data of the Zn:In ratios (Table 2.3) when compared to the EDS data of these ratios as shown in Table 2.1. For example, in the 600 nm emitting core/shell QDs, the Zn:In ratio according to EDS is 5.27:1, when the AAS results revealed a ratio of 2.09:1. Due to the intense calibration and bulk dissolution of AAS, this is a more accurate technique for the detection of the metal concentrations and ratios. Further to this, Table 2.1 shows the respective ratios of each of the atoms that make up the QD for each of the samples that were used in further concentration studies. The synthetic protocol for the core InP QDs did not involve the use of any sulfur-based reagents, but high atom ratios of this were observed for all of the core InP QDs. This can therefore, be attributed to possibly contamination as the glassware was cleaned with only clean solvent. Further cleaning would therefore be necessary in strong acids to avoid this contamination. As is seen in Figure 2.4, while the core/shell QDs consist of a significantly visible EDS peak for sulfur, the core QDs (inset) consist of a negligible one. However, more in-depth and accurate quantitative analysis like ICP-MS or XPS will be needed to investigate the In:P stoichiometry as well as the sulfur content.

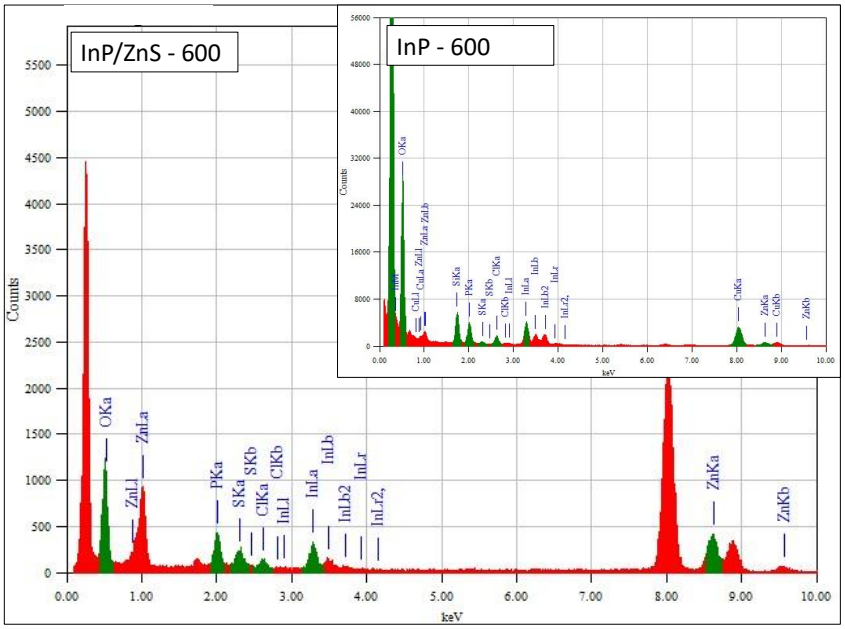

FIGURE 2.4: EDS of the core/shell InP/ZnS QDs. (Inset) EDS of core InP QDs.

2.3 Atomic absorption spectroscopy (AAS) to measure concentration

For the further use of these QDs for ligand exchange and conjugation, their concentration was an important factor to consider. To achieve a complete ligand exchange, knowing the size and number of particles per mL of solvent would aid in estimating how many ligand molecules there should be in the solution. The same goes for achieving an efficient conjugation of molecules to the particles.

Particle concentration can be calculated using Beer's law, $A = \epsilon * C * l$, where A is absorbance at the first exciton peak, ϵ is the extinction coefficient (or absorbance/particle), and l is the path length (in cm). This requires the ϵ value to be known and the size dependency of this can be analysed. While the absorbance for a known volume of particles can be measured with ease, the concentration of a dispersion of an unknown number of particles is more challenging. In the literature, this problem is generally approached by first determining the concentration of the atoms that make up the QD core and shell.

For this purpose, AAS was used here as well. It is a popular quantitative method for the determination of atomic concentrations with accuracy. It is used analytically

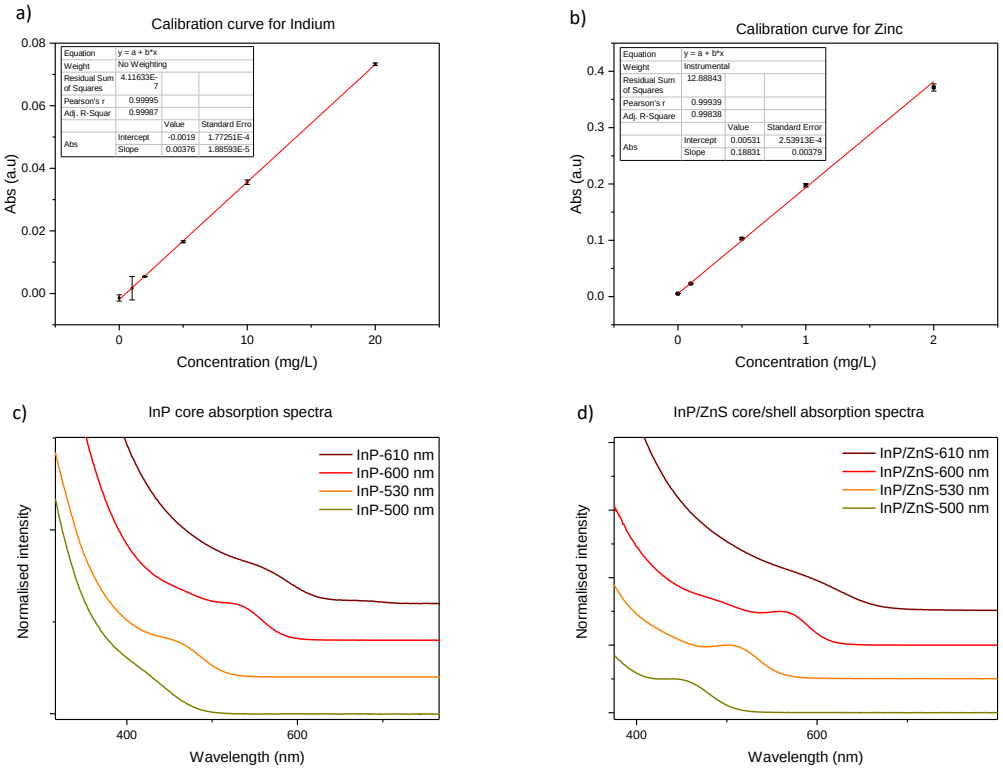

FIGURE 2.5: (a) Calibration curve for In. (b) Calibration curve for Zinc. (c) InP core QDs absorption spectra. (d) InP core/shell QD absorption spectra

to determine concentrations of free atoms in their gaseous state by measuring the absorption of the metal atoms. As each metal atom has its own absorption pattern, the detection of specific metal atom can be facilitated through the use of a hollow cathode lamp that can provide emission lines specific for the element's absorption spectrum. The only requirement for AAS is that the sample needs to be atomized, which is done with the help of an air-acetylene flame (in this case), which turns the sample into a vapor of free atoms. Prior to measuring the sample, a calibration is run using standards of known concentrations for the metal atom of interest. This is shown in 2.5(a) and (b).

Once the concentration of the metal atoms (In and Zn, in this case) and the absorbance of the particular sample are known, the estimation of the average number of In and Zn atoms per crystal results in a QD/L concentration with extinction coefficients calculated. The extinction coefficient for QDs have also been found to

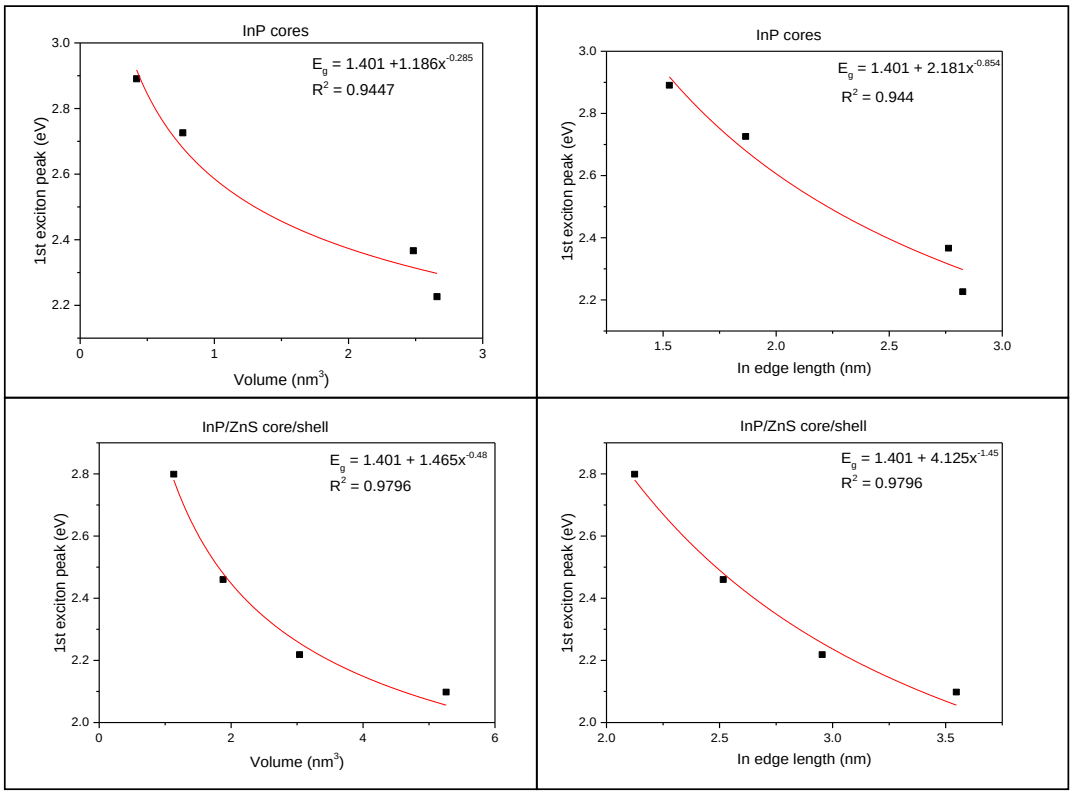

FIGURE 2.6: Size dependency of the first exciton for InP cores and InP/ZnS core/shells. In all instances a non-linear curve fitting was used

be dependent on the size of the QD, so a firm knowledge of the size and shape of the particles is necessary to make estimations.[80,81] This method has been frequently applied to determine QD concentrations for materials such CdSe and $CuInS_2$.[81,82] Additionally, Kucur *et al.* were able to show the effectiveness of AAS for determining nanoparticle concentrations in comparison to other methods as well.[83] Interestingly, the extinction coefficient is also larger for the QDs as compared to organic fluorophores (of the order 10^6 M^{-1} cm^{-1}) which further gives them an added advantage for biological imaging applications. This is because the QDs can retain their fluorescence for a longer period of time.

The various QD materials (of different sizes) were digested using conc. HNO_3 overnight after which they were diluted with Milli-Q water and analysed on the AAS to obtain In and Zn content in each of the samples. Corresponding UV-Vis spectra of each of known amounts of the QD samples were also measured to be able to relate the absorbance to the respective concentration measured using AAS. This

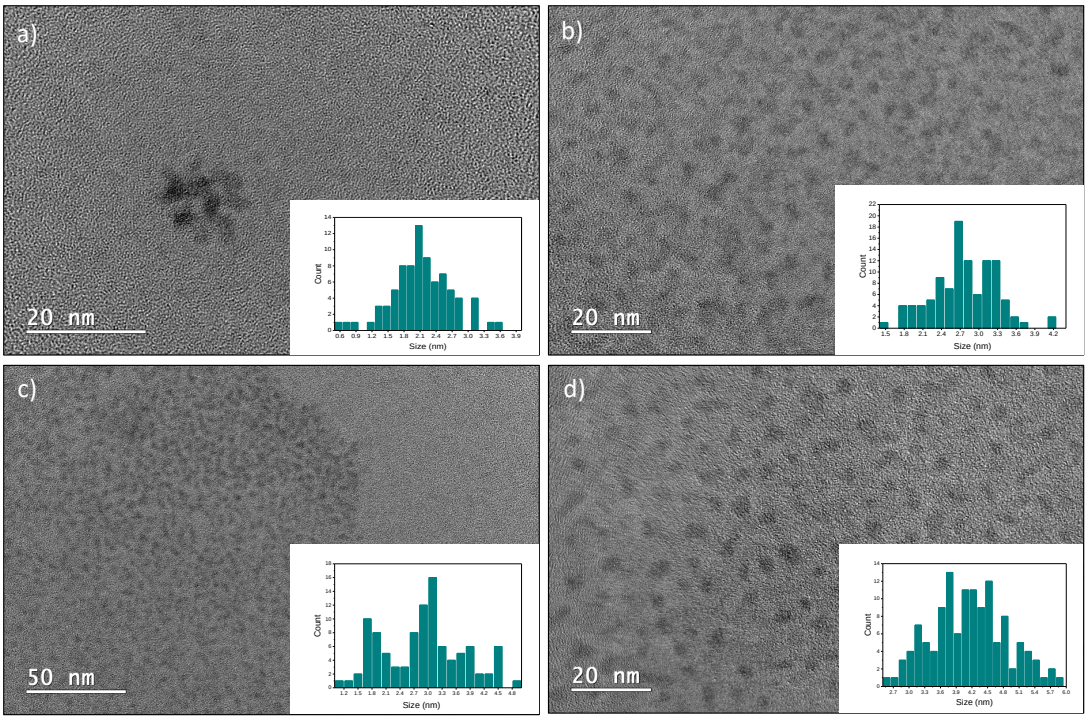

FIGURE 2.7: High resolution TEM images of InP cores their corresponding size distributions (inset) (a) InP core- 500 nm (b) InP core-530 nm (c) InP core-600 nm (d) InP core- 610 nm.

process was done for the InP cores as well as the InP/ZnS core/shell materials.

2.4 Size dependency and extinction coefficient

It is known that the optical properties depend on the size of the QD is due to the quantum confinement effect.[84,85] Because the InP QDs are viable alternatives to CdSe-based QDs, it is important to study the relationship between their size and absorption properties, as UV-Vis absorption is one of the fastest and easiest bulk analytical methods.[46] While the theory related to this includes multiple solutions, the effective mass approximation (EMA) is the least demanding.[84] The EMA, which is derived using the particle-in-a-box model, proposes that the additional band gap energy E_g (on top of the energy of the bulk band gap $E_{g,bulk}$) is inversely proportional to the square of the diameter (d) of the QD.[86] The model therefore implies that there should be a linear relationship between the energy of the band gap and $1/d^2$.

$$E_g = E_{g,bulk} + C/d^a \tag{2.1}$$

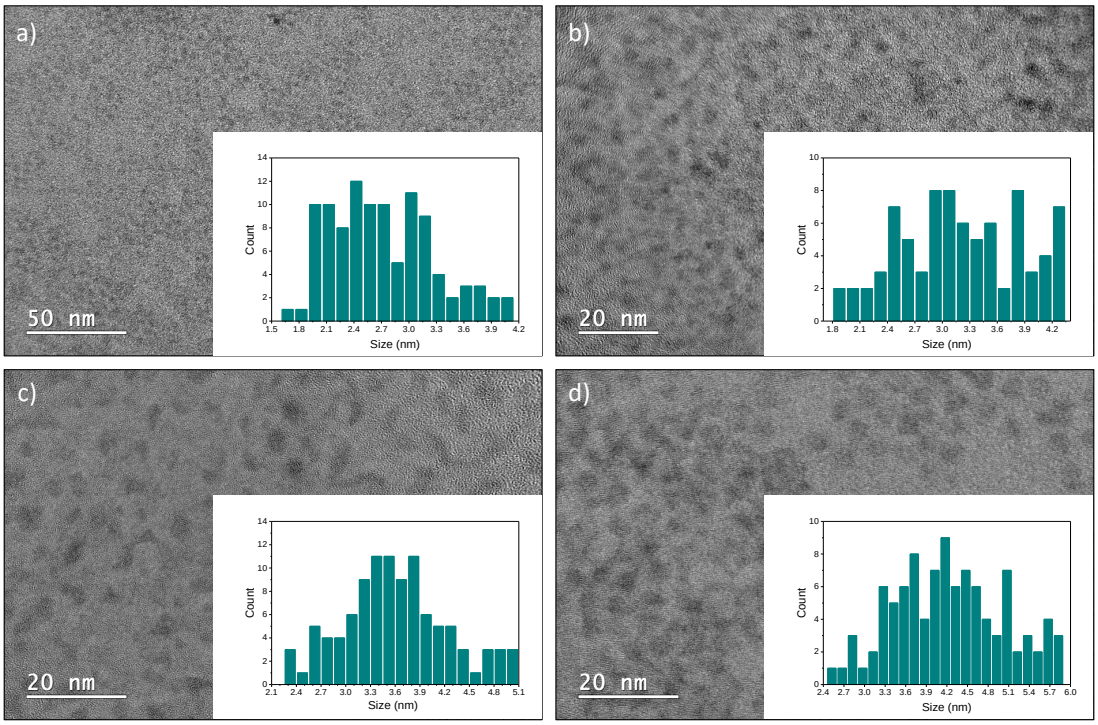

FIGURE 2.8: High resolution TEM images of InP/ZnS core/shell emitting at specific wavelengths and their corresponding size distributions (inset) (a) InP core/shell- 500 nm (b) InP core/shell-530 nm (c) InP core/shell-600 nm (d) InP core/shell- 610 nm

This can be simply described in Eq. 2.1 where C is a proportional constant and a is a real number.[85] However, the experimental data related to QCE can be quite different to theory, especially when a shell is involved, which can change the confinement behavior of the QDs. While the sizes should be relatively monodisperse, this is challenging to determine using electron microscopy as only a very small subset of particles can be examined at a time.

Cho *et al.* showed through their density functional theory (DFT) study on the electronic properties of the InP QDs that the a was actually closer to 1 (1.172) and not 2, as has been described by the EMA. Furthermore, the first principles calculation that were conducted assumed a spherical QD shape. The work recently by Kim *et al.*[79] has shown that the InP cores by themselves appear more tetrahedral. However, the core/shells in this work were observed to be more ambiguous in shape. Therefore, for the size calculations, a tetrahedron model was assumed for the core QDs and the ZnS shell was assumed to grow spherically over them.

To get an idea for InP sizes, each of the cores were imaged as soon as they were

synthesised, as the InP cores do not stay stable in air for more than 1 day and this would affect the measurement of their size. Table 2.2 shows the median size measured for 100 QDs per sample, which match well with the increasing wavelength of the exciton peak in the UV-Vis spectra of the materials, which are shown in Figure 2.5 (c), corresponding to the larger diameter of the particles. The size histograms also show core sizes that have a broad full-width half maximum (FWHM). The broader size histograms are also due to the nanoparticles being low-contrast and difficult to image, therefore, the manual element of image processing may have introduced errors in the measurement of each of the sizes.

Each of the sample sizes further show an increase from the corresponding core/shell sizes with a difference of 0.56 nm, 0.48 nm, 0.62 nm and 0.05 nm for the 500 nm, 530 nm, 600 nm and 610 nm emitting QDs. One monolayer of ZnS with the zinc blende structure is 0.541 nm thick. Therefore, the first three QD shell thicknesses relate to a roughly one monolayer of ZnS thickness. The last shell thickness relates to the largest QDs synthesised using the same amount of shell precursors as all the other three. So, it is possible that the shell for these is really thin. However, the core and core/shell QDs that emit at 610 nm had a very broad size distribution as well and their respective sizes were quite challenging to manually measure.

Once the sizes were determing, the concentration of the metals in each of the QD samples was investigated. To determine the concentration of the QD samples, calibration curves were developed using the element lamps for the cations, In and Zn, and their respective calibration standards. These curves are shown in Figure 2.5 (a) and (b) and have excellent linearity. The working range of concentration of In that can be detected is a minimum of 2 mg/L and maximum of 20 mg/L. Contrasting this, the Zn can be detected at lower concentrations ranging from 0.01 mg/L to 2 mg/L. The QD samples were diluted in order to achieve appropriate concentrations that fit within the calibration curves for In and Zn.

The Zn:In ratios could be calculated using the AAS measurement which is shown in Table 2.3. Even though the cores were not shelled, the synthesis involves the use of $ZnCl_2$ as a catalyst, and therefore, minimum concentrations of Zn were measured in all of the core materials as well. The different Zn:In ratios show the difference between the core and core/shell materials as well with all the cores having nearly 1

Sample name	InP cores (nm)	InP/ZnS (nm)
QD-500 nm	2.09 ± 0.57	2.65 ± 0.73
QD-530 nm	2.73 ± 0.51	3.21 ± 0.74
QD-600 nm	2.97 ± 0.87	3.59 ± 0.80
QD-610 nm	4.19 ± 0.83	4.24 ± 0.87

TABLE 2.2: Table of the median diameters of each of the QD core and core/shell samples measured using high-resolution TEM

zinc atom for every 3 indium atoms. The least zinc was observed for the cores in the one-pot synthesis that yielded InP-600 nm. The other three syntheses are modified from this optimized one, so differences in solution polarities may account for these discrepancies.[54] The variation of ratios shows that the final product was sensitive to the method used. Expectedly, the core/shell materials show higher Zn:In ratios with nearly 2 zinc atoms for every 1 In atom, which further explains the increased QYs of the core/shell materials.

After determining the mean size and number of In and Zn atoms per sample, there needed to be an estimation of the number of In and Zn atoms per QD. Despite the energy dispersive X-ray Specstroscopy (EDS) elemental ratios of In and Zn, the materials were modelled as In-terminated tetrahedrons with a shell of 1:1 ZnS. The sizes of the core and core/shell were optimised using a reduced gradient algorithm, such that the total particle size and Zn:In ratios matched the experimental values. As the InP cores had edge lengths outside the bounds of a perfect tetrahedron, these values were taken as weighted averages of the closest two sizes.

The In edge length calculated in this manner was then used to calculate the volume of a tetrahedron for the cores and spherical shell. The edge lengths and volumes were both plotted against the energy of the first exciton peak (eV) and displayed in Figure 2.6. The curves were then fit to a polynomial with the band gap of the bulk InP at 1.40 eV as calculated by Cho *et al.*.[85] The core and core/shells were fitted separately as it has been shown that the size dependency is affected by the surrounding environment of the cores.[85]

The size dependency of spherical QDs follows the Brus equation outlined below in Eq. 2.2:

$$E_g = E_{g,bulk} + (h^2/8r^2)(1/m_e^* + 1/m_h^*) \tag{2.2}$$

where, E_g is the energy of the band gap, E_g, *bulk* is the energy of the band gap of the bulk material, h is Planck's constant, r refers to the radius of the QD, and m_e and m_h are the effective masses of the excited electron and hole. While, this shows that the energy of the band gap is dependent on $1/r^2$, Cho *et al.* were able to show that for InP QDs, this dependency trends more like $1/d$. The curves here were fit to the equation:

$$E_g = E_{g,bulk} + Cd^a \tag{2.3}$$

Therefore, the a values on all the curves are negative, which further confirms the inversely proportional relationship. In addition to this, both the core and core/shell indium edge length plots have an a value close to 1 (cores: $a = -0.85$, and core/shell: $a = -1.45$). The larger a value indicates that the band gap depends on the size more sensitively for the core/shell materials. Using the In edge length, a value is 2.18 and 4.13 eV nm^{-a} for cores and core shell. C was previously reported for InP to be 3.90 eV nm^{-a}[87] using a theoretical approach. All of these fits are only legitimate assuming that the In tetrahedron fit perfectly in a sphere of shell material grown around it.

The extinction coefficient of the QDs was also calculated using the number of In atoms per nanocrystal and the moles of In measured using AAS. This is also shown in Appendix A (Section A.3). This yielded a number of QDs in the sample that were measured. The absorbance intensity was then divided by this number of particles to calculate extinction coefficient. The extinction coefficients however, do not follow the size dependency as was expected. A reason for this could be that the extinction coefficient depends more sensitively on the size, and the difficulty with the measurement of the sizes of the QDs as well as the resulting polydispersity could have lead to a poorer fit. Further studies on this are therefore needed along with a more accurate size measurement and measuring QDs that result from the same synthesis protocol. Due to the time commitment of obtaining these results, they were not carried forward for the rest of the thesis which was focussed on the 600 nm-emitting QDs and their use in biological applications.

Standard techniques for determining concentration of QDs use the weighing method which involves precipitation of the particles or evaporation of the solvent in a pre-weighed container, and weighing the solid. This is then typically reported as mg/ml concentration of QDs. While this method is quick and easy to do in comparison to the method developed here, it has several drawbacks. For obvious reasons, it is inaccurate as it does not quantify the number of nanocrystals in a solution. Therefore, for further use of the nanocrystals in ligand exchange and bioconjugation, the efficiency of the ligand exchange and conjugation would be difficult to determine. This will limit their application for more quantitative detection applications as well. The precipitation method enables a different weight of nanoparticle precipitation everytime it is used making it inconsistent. This further impacts the final concentration calculated as the volume of the supernatant that is discarded could have contributed to the final weight of the dry QD powder. Additionally, the precipitation method uses ethanol and toluene which are discarded but some solvent left in the precipitate could contribute to the final weight. A similar problem arises with the evaporation method. Even though toluene is relatively easy to evaporate, some solvent may still be left in the QD powder further complicating the final concentration value. In conclusion, the method developed here is therefore still a more accurate way to calculate concentrations, especially for the particles synthesised using the protocols used in this thesis because it uses nanocrystals concentration values and absorbance of the sample as opposed to the weight of the dry sample.

2.5 Materials and methods

All reagents were purchased from Sigma Aldrich, unless specified otherwise. Purity is stated in brackets.

2.5.1 InP/ZnS QD synthesis

The method used to synthesise the QDs has been published previously.[53] The shelling precursor tri-octylphosphine-sulfur TOP-S was made by mixing 0.71 g of sulfur in 10 mL of tri-octylphosphine (TOP) (technical grade, 90%) until the sulfur was dissolved fully. The zinc shelling precursor Zn-ODE was made by mixing 5.17 g zinc

Core InP QDs					
Sample	[In] (mol/L)	[Zn] (mol/L)	Zn:In N/A	A (a.u.)	λ_{max} (nm)
InP-500 nm	0.0062 ± 0.0002	0.0017 ± 0.00002	0.27	0.053	412.04
InP-530 nm	0.0176 ± 0.001	0.0079 ± 0.0001	0.45	0.267	458.94
InP-600 nm	0.0132 ± 0.002	0.0009 ± 0.00003	0.07	0.204	529.94
InP-610 nm	0.0063 ± 0.0002	0.0042 ± 0.00007	0.67	0.059	552.97

Core/shell InP/ZnS QDs					
Sample	[In] (mol/L)	[Zn] (mol/L)	Zn:In N/A	A (a.u.)	λ_{max} (nm)
InP/ZnS-500 nm	0.07945 ± 0.0002	0.2338 ± 0.02	1.96	0.230	444.99
InP/ZnS-530 nm	0.0506 ± 0.002	0.1927 ± 0.02	2.53	0.158	508.01
InP/ZnS-600 nm	0.0708 ± 0.001	0.2219 ± 0.001	2.09	0.726	561.97
InP/ZnS-610 nm	0.04063 ± 0.001	0.1266 ± 0.0006	2.08	0.144	587.95

TABLE 2.3: AAS concentrations of In and Zn content correlated with the first excitonic absorption and its intensity

undecylenate (98%) with 5 mL of TOP and 25 mL of ODE (1-octadecene) (technical grade, 90%) and by heating the mixture at 120 °C until all the solid had dissolved. Both the precursors were flushed with nitrogen using Schlenk techniques.

The InP core was synthesised by mixing 0.45 mmol of indium(III) chloride (98%) and 2.2 mmol of zinc(II) chloride ($\geq$ 98%) in 5.0 mL of oleylamine (technical grade, 70%) at 120 °C under vacuum for 60 mins. After this, it was put under nitrogen atmosphere and heated to 180 °C. Tris-(diethylamino)phosphine (97%) (1.6 mmol, $P(DEA)_3$) was then quickly injected into the reaction mixture after the desired temperature was reached. The shelling precursors were then injected slowly after 20 mins of core growth. The TOP-S (1 mL) was injected slowly over a period of 10 min (at the rate of 0.1 mL/min). The temperature is ramped from 180 °C to 200 °C after 40 mins. After an 1 h, 4 mL of the zinc precursor was injected over a period of 10 mins (0.4 mL/min). The temperature was increased further from 200 °C to 220 °C. After 30 minutes, 0.7 mL of the TOP-S was injected slowly over a period of 10 mins (0.07 mL/min) and temperature was ramped to 240 °C. The zinc precursor (2 mL) was added after 30 mins (0.3 mL/min) and the temperature was further increased to 260 °C. The reaction was stopped after 30 mins and rapidly cooled down. The reaction mixture was diluted with 5 mL of toluene. The QDs were then precipitated in ethanol and centrifuged at 10,000g for 10 mins. The resulting pellet was resuspended in a minimum amount of toluene. The precipitation step was then repeated

one more time. These were dispersed in toluene. This synthesis yielded red QDs that emit at 600 nm.

2.5.2 Characterisation

Transmission electron microscopy (TEM)

The QDs dispersed in toluene were run through a toluene size column for purification which contained BioBeads SX-1 (200-400 mesh) after which 10 μL of the purified sample was loaded onto the carbon-coated copper grid. This was allowed to dry, after which the grid was plasma cleaned before loading into the TEM. The TEM2100F (JEOL) was used for imaging. The size was measured for a 100 QDs per sample using the ImageJ software.

Ultraviolet-Visible absorption spectroscopy (UV-Vis) and Photoluminescence (PL)

The UV-Vis of the QD samples was done using the Cary50 Bio instrument (Agilent Technologies). The concentration was adjusted until the absorbance the excitation wavelength was under 0.1 units. Fluorescence and QY measurements were done on the same concentration on the FLS980 (Edinburgh Instruments) at room temperature. Running a dilute sample (under 0.1 units) avoids any self-absorbance errors in the PL measurement. The QY was calculated using an integrating sphere using the direct excitation method.

AAS

The indium and zinc content of the nanoparticles were determined using flame AAS iCE3500 (ThermoFisher Scientific). A air-acetylene flame was used and the flow rate of the samples and the calibration standards was set to 1.1 mL/min. After each sample was run, the auto-sampler was washed for 10 seconds. For sample preparation, the toluene from 100 μL of the QD sample was evaporated off and the samples were heated to 60°C. After this, the solid was digested using 80 μL of conc. HNO_3 (70%). This process was aided with ultrasonication and the solutions were further diluted

to 2 mL with Milli-Q water. This was then diluted to 10 mL using 2% HNO_3. Further 10X, 20X and 100X dilutions were made for detecting the indium and zinc. The standards for calibration were purchased from Sigma Aldrich.

Chapter 3

Ligand Exchange Methods

3.1 Background and motivation

The InP/ZnS QDs syntehsised as reported in the last chapter are coated in oleylamine ligands that stabilise them and prevent aggregation. These amines with long hydrocarbon chains are hydrophobic, so the particles are only able to be dispersed in non-polar solvents such as toluene or hexane. Alkylamines such as oleylamine have been commonly used for the passivation of the surface of QDs. This is because of the affinity that the amine end has to metals such as the Zn in the ZnS shell. While this is a possibly through a chemisorption mechanism, the use of a thiolated ligand forms a covalent dithiol linkage with the S on the ZnS surface. To be applied in biological applications, the QDs need to be made hydrophilic and thereby, water dispersible. To conjugate to the targeting compounds, there also needs to be a carboxylic acid group pointing outwards to react with an amine group on the biomolecules.

A range of different ligands can provide the QDs with this property. To retain the small size of the QDs, low molecular weight mercapto-acid ligands are particularly advantageous.[59] Unfortunately, efforts to exchange the oleylamine ligands with other small-molecule ligands have normally led to a significant decrease in QYs and poor stability in water.[88,89] However, some select ligand exchanges published in the literature produced highly stable QDs that are water dispersible. As Zhang *et al.* reported high stability and high QY for QDs capped with MSA or MPA molecules, their method to obtain water dispersible QDs was one of the methods that was followed in the work presented here.[90] MSA has two carboxylic acid groups, producing exceptionally stable QD-MSA in solution for multiple weeks. The method for achieving QD-MSA includes the use of ammonium hydroxide to achieve a reactive thiol that can displace the oleylamine ligands. This was also used in the literature frequently as a single-step ligand exchange.[41,91] However, none of these articles probed the QY of the QDs after ligand exchange. Zhang *et al.* investigated the effect of the ligand exchange on fluorescence intensity but as fluorescence intensity depends on the concentration of the QDs used to obtain the measurement, this is difficult to compare with the results here. The reduced QY in all three of the above papers could be due to the use of ammonium hydroxide, which causes significant surface etching.

Avoiding the use of ammonium hydroxide altogether, Brunetti *et al.* used a pH

9 borate buffer and sonication over 2 h to achieve the same result. However, the change in QY after ligand exchange was not reported. Alternatively, tetramethylammonium hydroxide (TMAH) has also been used to aid in ligand exchange.[59,92] In fact, the approach used by Pong *et al.* utlising TMAH led to almost no change in the QY of their QDs when replacing the native trioctylphosphine ligands with MPA. They attributed this to the strong base being able to abstract a hydrogen from the thiol group of the molecule, thereby leading to a complete coverage of the QD with new ligands and forming a barrier against the water molecules.[59,93]

As opposed to the single-step ligand exchanges, multiple-step ligand exchanges may prove to be more efficient in removing hydrophobic oleylamine ligands, and thereby improving stability in water. Additionally, polyethylene glycol (PEG)-based polymer ligands have been known to improve stability due to their higher surface coverage.[94] Research has shown that using a single-step ligand exchange, only about 50-85% of the native ligands are removed from the surface. It is predicted that only 2-4 PEG molecules are needed to stabilise the surface of a 2 nm QD, so each ligand can electronically compensate a large area. This high surface coverage of the PEG molecules can overcome the unfavourable interactions of the remaining native ligands, which depend on the energy of the interaction between the native ligand and solvent, the energy of the interaction between PEG and the solvent, and the stability of the PEG in a solvent. They showed that the PEG ligands with some native hydrophobic ligands stayed stable in polar organic solvents such as chloroform, however, the unfavourable interaction between the native ligands and water still caused some aggregation of the particles. Therefore, using a multiple-step ligand exchange would mean that more of the native ligands have been removed from the QD surface, leading to a more stable dispersion in an aqueous environment.

This Chapter provides a survey of the popular ligand exchange methods used in literature to get an understanding about achieving the best balance between retention of QYs and colloidal stability. This is further be applied for conjugation of bio-molecules in Chapter 4 and obtaining a conjugate that is not affected by harsher biological conditions.

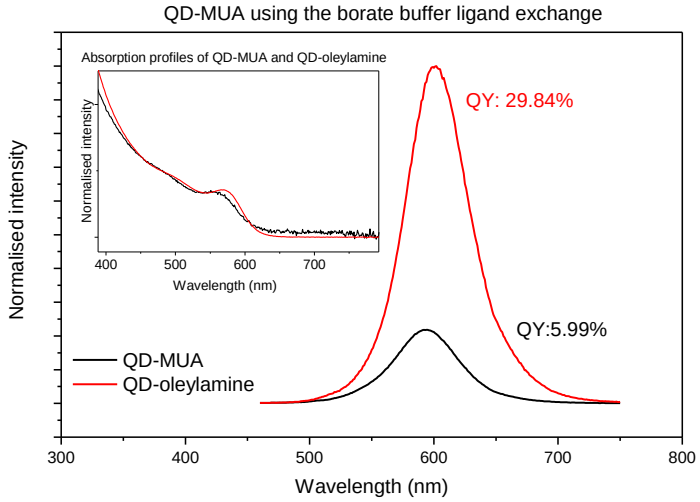

FIGURE 3.1: A decrease in QY was seen after the ligand exchange. The PL spectra was normalised according to the corresponding absorbance at the excitation wavelength of 480 nm to correct for concentration differences.(Inset) Absorption profiles of the aqueous QDs using the borate buffer route compared to the QD-oleylamine.

3.2 Results and Discussion

3.2.1 Single-step ligand exchange

The general principle behind the single-step QD ligand exchanges was the use of a basic pH environment to enable deprotonation of the thiol group on the mercapto-acids. Initially, this was accomplished by tuning the aqueous solution of thiols to pH 9 with a borate buffer and sonication with a small amount of the toluene-QD suspension. The exchanged QDs retained the original QD-oleylamine's absorption profile, which suggests there were minimal changes to the particle sizes 3.1 (inset). While this was the simplest method to follow, it resulted in water-dispersible QDs with a low QY of 6% as shown in Figure 3.1. These QDs also crashed out of solution within a few weeks and showed large aggregates in solution after a few days. This indicates they would be unsuitable for further use for conjugation to a biomolecule.

The use of an ammonia-based reactant such as ammonium hydroxide, tetramethylammonium hydroxide, or EDA serves the same purpose as the borate buffer by enabling a more basic environment and allowing for the deprotonation of the thiol. The TMAH method led to QDs that fluoresced at only 3.57% however, these stayed stable and in dispersion for months and retained the original exciton absorbance

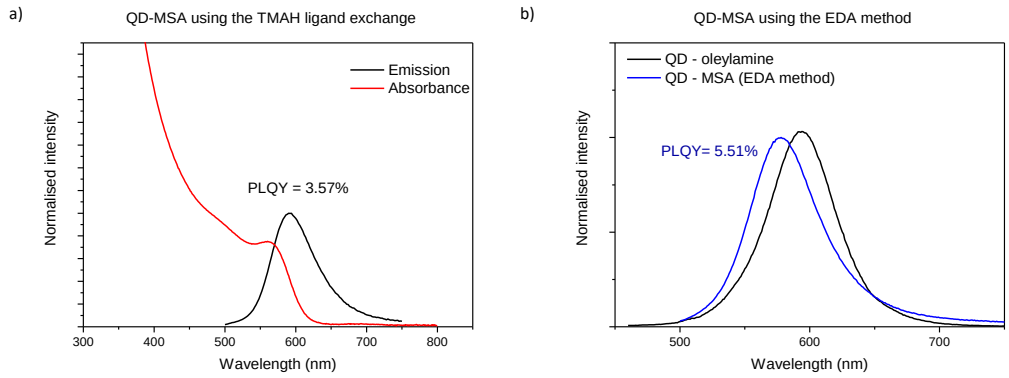

FIGURE 3.2: (a) Absorption and emission profiles of QD-MSA from the TMAH ligand exchange. (b) Emission comparison between the QD-MSA using the EDA method and the original QDs in toluene.

properties. The EDA method was a pseudo-two-step method that was supposed to replace the original oleylamine ligands with EDA as an intermediate ligand, after which the EDA could be replaced with a mercapto-acid more favourably. However, the initial exchange occurs without a phase change, so many of the native ligands are likely left on the surface. This method resulted in a reduced QY of 5.51% (Figure 3.2)(b)) as well and a slight blue shift in the peak emission. In addition to the slight shift, there is also an additional red-tail in the PL spectra of the EDA method QDs. The red-tail or skewing to one side usually indicates surface defects and could therefore imply that the EDA quite possibly etched the surface.[95] Unfortunately, the QDs synthesised using this protocol only stayed in dispersion for only 1 day, and the concentration of EDA and new ligand used did not have any effect on the final product's stability.

The use of ammonium hydroxide proved to be the most successful and resulted in a stable dispersion of water-dispersible QDs that stayed in dispersion for a long period of time. The QDs resulting from this ligand exchange retained the size of the original QDs as is observed in Appendix B (Figure B.1). However, the harshness of the ammonia and its effect on the QDs became quite evident. Shown in Figure 3.3 (a) and (b) are the absorption and emission profiles of different samples of QD-MSA made using the same ammonia method. In the red profile, are the QD-oleylamine which contains two absorption peaks at 480 nm and 550 nm. The exciton absorbance at 550 nm undergoes a shift as seen by the green asterisk in Figure 3.3, with the

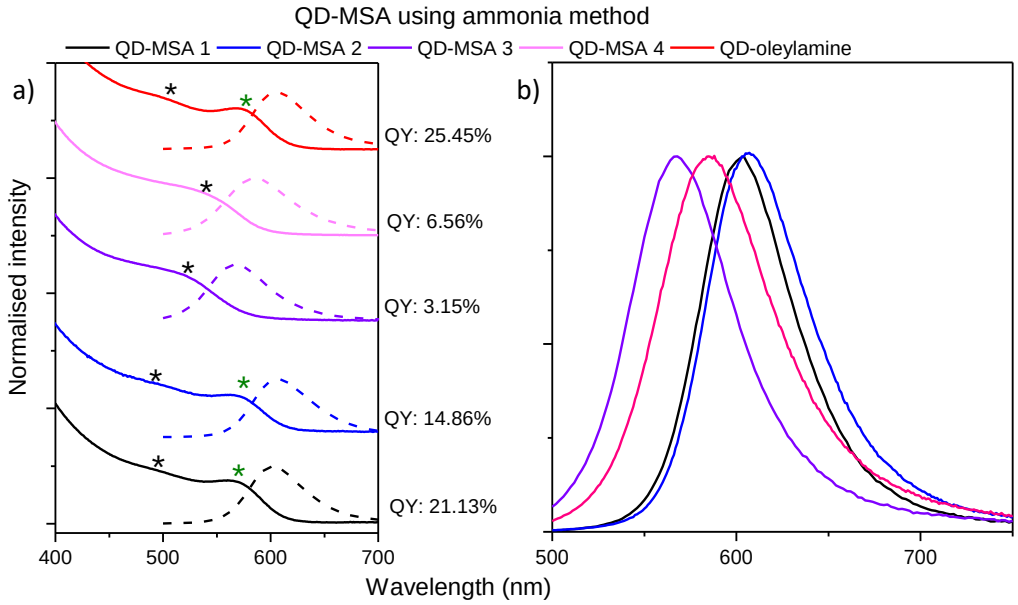

FIGURE 3.3: (a) Absorption (solid line) and emission profiles (dashed lines) of different QD-MSA samples from the ammonia-based ligand exchange. (b) Emission comparison between the different samples QD-MSA.

largest being seen in QD-MSA samples 3 and 4, and these changes are coincident with a loss in QY. For QD-MSA samples 1 and 2, this absorbance is retained and they possess higher QYs of 14.86% and 21.13%, respectively.

The efficiency of the ligand exchange can be investigated using Fourier-transform infrared spectroscopy (FTIR), which gives a "fingerprint" of the molecular vibrations in the sample. The changes in ligands can then be traced by the presence (or lack thereof) of certain features specific to the functional groups of the compounds. In Figure 3.4, the original QD-oleylamine sample shows sharp and strong C-H stretches at around 3100 cm^{-1}. The coordination of oleylamine to the QD is through the amine group, however it was difficult to see this through FTIR. Compared to that of QD-oleylamine, the QD-MSA spectrum does not show the sharp C-C peak or any of the amine-related stretches and bends either. The MSA trace shows the free thiol stretch at around 2500 cm^{-1}. This thiol stretch is completely eliminatd for the QD-MSA, which implies that the molecule is binding to the QD through the thiol instead of the carboxylic acid. Similarly, the thiol related H-C-S and C-S stretches that are visible in the 1000-500 cm^{-1} range for MSA, are not present for the QD-MSA spectrum.

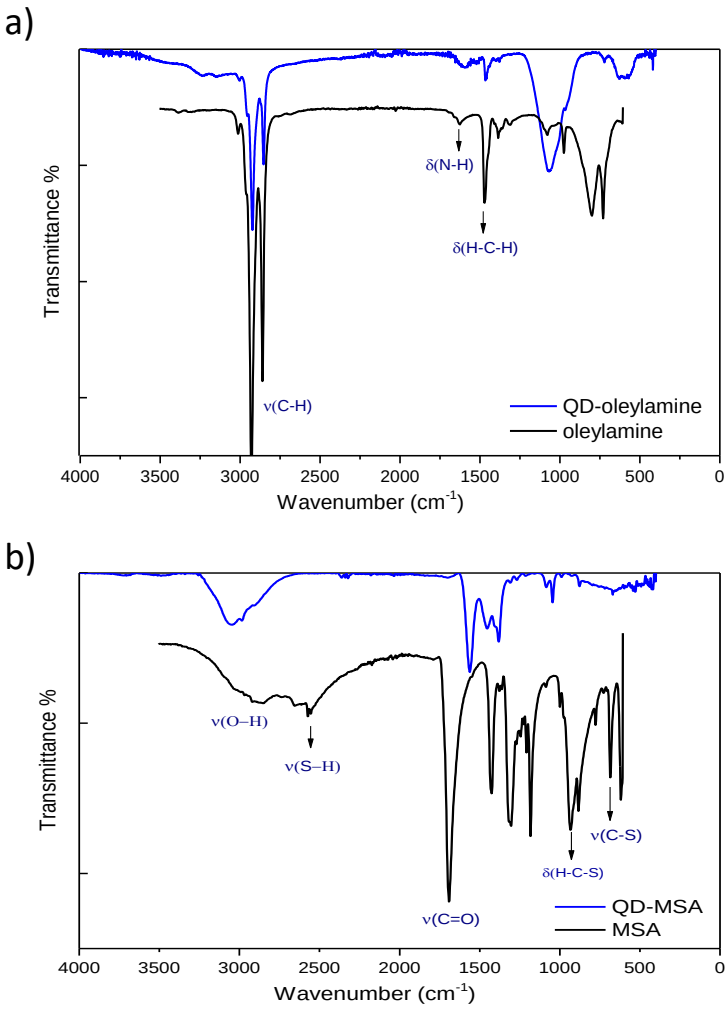

FIGURE 3.4: (a) FTIR of oleylamine and QD-Oleylamine. (b) FTIR of MSA and QD-MSA.

3.2.2 Multi-step ligand exchange

As there were several issues with the 1- and 2-step ligand exchanges, the effectiveness of multi-step ligand exchanges was probed. The process for the transfer of the nanoparticles into the aqueous phase was done by first using a similar protocol as published in the article by Guhrenz *et al.*.[65] The *n*-methylformamide (NMF) was mixed with acetone and ammonium chloride, after which the QDs (in toluene) were added to this mixture. This caused the native oleylamine ligands to be replaced with chloride ions. The acetone acted as as the mild flocculation agent which would aid in the rapid removal of the oleylamine ligands. This was then precipitated out using

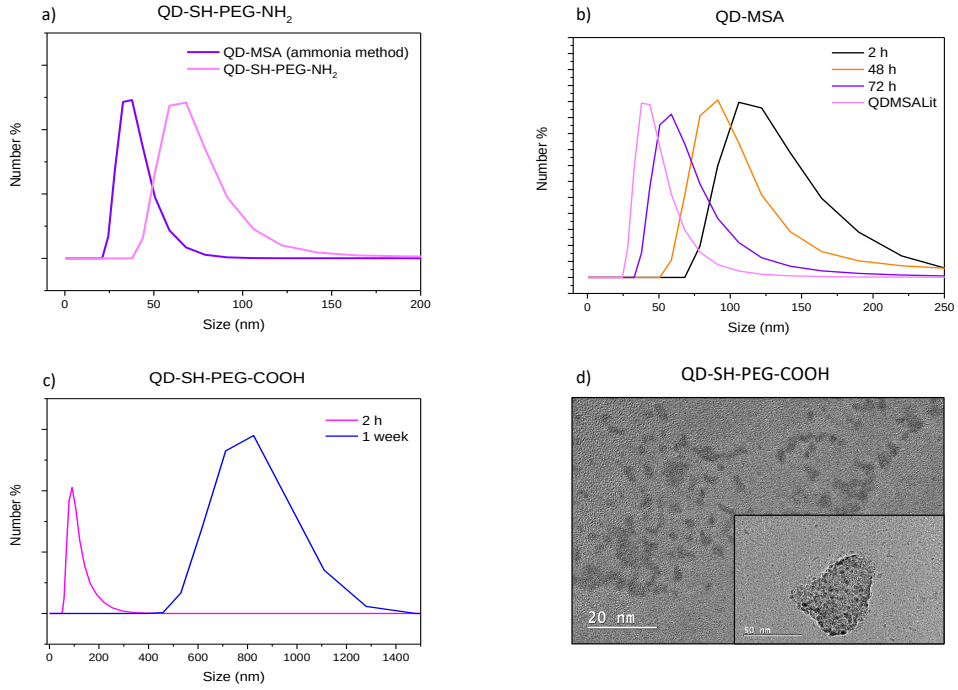

FIGURE 3.5: (a) DLS measurement of QD-SH-PEG-NH_2 made using three-step method compared to QD-MSA made using the ammonia method. (b) DLS measurements of QD-MSA made using the three-step method over time after transfer to the aqueous phase. (c) DLS measurement of QD-SH-PEG-COOH over time. (d) TEM image of QD-SH-PEG-COOH

n-butylamine which works as an intermediate ligand and coordinates to the chloride on the surface of the QD. The QDs was readily dispersed in chloroform. The FTIR of this is shown in Appendix B (Figure B.2). This shows amine-related N-H stretches and bends, as well as the C-H stretch from the butylamine. Some of the original QD stretches in the fingerprint region (1500-500 cm^{-1}) are retained, which was not the case for the QD-MSA spectrum seen in Figure 3.4. While the amine and the C-H-related peaks could be either from the butylamine or leftover NMF (initial solvent), it is more difficult to attribute the peaks in the fingerprint area.

After this, the authors describe the use of HS-PEG-NH_2 molecules to replace the butylamine and hypothesised that PEG coordinated *via* the amine group and not the thiol end. They were then able to redisperse their QDs in a basic dispersion of 0.1 M NaOH. In contrast to what they reported, the basicity of this dispersion should deprotonate the thiol and make the coordination through this end of the molecule more favourable. The bi-functional ligand HS-PEG-NH_2 worked quite well, with a

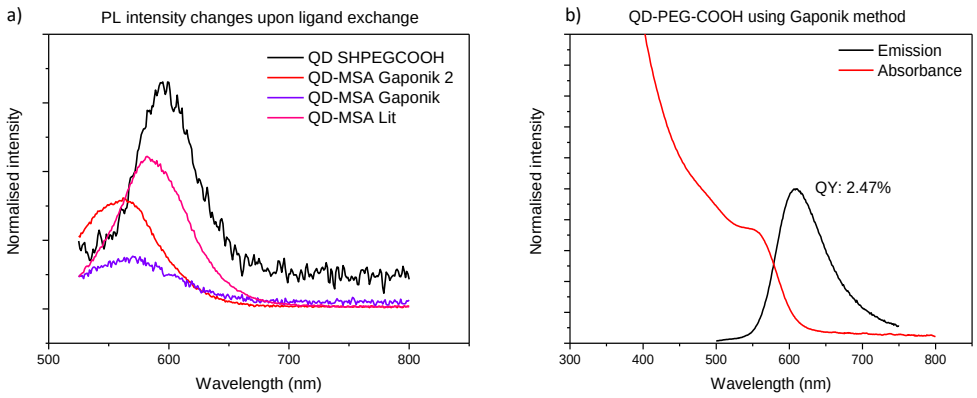

FIGURE 3.6: (a) PL intensity changes comparing the ammonia method and the three-step method as well as MSA and PEG-based ligand. (b) Absorption and emission profile of QD-PEG-COOH

size according to DLS of 70 nm (Figure 3.5) and a high zeta potential in pH 9 (Table 3.1). However, shown in the Appendix B Figure B.3 is the intensity distributions for the respective QD ligand exchanged samples. For QD-SH-PEG-NH_2, this shows a high distribution from a population of around 400 nm as well in addition to a population at 70 nm. This signifies the presence of aggregates. Zeta potential can be described as the potential difference at the particle-water interface. It is also therefore, a measure of the degree of attraction or repulsion between the particles and can be related to the stability of colloidal dispersions.[96] Guhrenz *et al.* showed that this ligand exchange with their nanoparticles gave rise to materials ranging in size from 10 nm to 51.4 nm for different types of shells.[65] The negative zeta value hints towards the thiol-end pointing outward.

Neither of these functionalities are useful for further conjugation using the EDC/NHS coupling, so at first, a H_2N-PEG-COOH ligand was used. This failed to work and the QDs were not dispersed in the aqueous environment at all. The reason for this is possibly the fact that the amine-end does not coordinate to the QD surface either as was predicted by Guhrenz *et al.*.

For a proof of concept, we used a mercapto-acid (primarily MSA) instead of the above molecules. Figure 3.5 (b) shows the size as measured using DLS over three

days after the dispersion of the QDs in water. After 2 h from synthesis, the mean size is at 120 nm which is on the larger end as it was already seen that QD-MSA synthesised using the ammonia method is around 30-40 nm. After 3 days however, there is a decrease in the hydrodynamic diameter of the QDs and they are quite close to the diameter of the QD-MSA made using the ammonia method. These number results are in good comparison to the intensity distributions shown in Appendix B Figure B.3.The size by number is the size for the maximum number of particles counted plotted against the size. While this can be usually reliable, it cannot be used for a sample which may have two (or more) size populations. Size by intensity gives rise to contributions from particles according to different scattering intensity. There are large aggregates present in the sample after 2h of synthesis. These aggregates completely disappear after 3 days of synthesis. Interestingly, the intensity distribution size of the sample after 2 days or 48 h of synthesis shows a significant reduction in size to about 10 nm, which increases to 200 nm after 3 days. This result further agrees with the intensity distribution of the QD-MSA sample made using the ammonia method.

In any case, applying a PEGylated molecule might lead to a more stable dispersion, as they are able to compensate more of the surface. Therefore, HS-PEG-COOH was implemented with the exact same protocol. While this worked just as well as the MSA initially, the particles aggregated in a week and completely precipitated out within two weeks. The DLS data from Figure 3.5 (c) shows the QD-SH-PEG-COOH was at about 120 nm after synthesis. However, after 1 week, the same QDs were yielding hydrodynamic diameters of 800 nm. Further TEM imaging of this sample (Figure 3.5(d)) showed QDs that were difficult to resolve individually, and typically formed aggregates (inset) of around 100 nm. Again, Figure B.3 reflects the presence of these aggregates as well as the sample shows particles of size 200 nm after 2 h of synthesis which then, increases to 800 nm aggregates.

As with the 1-step shemes, the multistep ligand exchanges also did not retain the QY from the original QDs. Figure 3.6 shows the PL intensity changes between the QD-SH-PEG-COOH and QD-MSA made using ammonia and the three-step method. The QD-SH-PEG-COOH showed a QY of 2.47% which is a significant reduction from the original 25.35%.

Sample name	Zeta potential (mV)
QD-MSA	-40.08
QD-MSA (Gaponik method)	-17.00
QD-SH-PEG-COOH (Gaponik method)	-0.60
QD-SH-PEG-NH_2	-22.80

TABLE 3.1: Table of zeta potentials for ligand-exchanged aqueous QDs at pH 7.

To conclude, the overall aim of this chapter was to find a ligand exchange method that did not comprimise QD QY, retained particle stability even with varying pH and produced materials that could be further conjugated. The ammonia-based methods tend to etch the surface more, but resulted in particles that are more stable dispersions. While it appeared promising in literature, the multi-step ligand exchange proved to be unsuccessful in retaining the QY and the particle stability. In comparison, the ligand exchange using ammonia showed the best balance between dispersion and QY despite discrepancies between different samples. As future work, it would be beneficial to test and optimise the amount of time given for the ligand exchange with the same QD-oleylamine sample to be able to avoid decreased QYs.

3.3 Materials and methods

All reagents were purchased from Sigma Aldrich, unless specified otherwise. Purity is stated in brackets.

3.3.1 Small molecule ligands

Two different types of ligands were used for ligand exchange. Small molecule ligands like MSA, MPA and MUA preserve the small size of the QD. As opposed to this, polymeric PEGylated ligands can achieve higher coverage and therefore, higher colloidal stability in aqueous conditions.

Ammonia-assisted ligand exchange

Mercapto-ligands used for these experiments were: MSA (97%), MPA ($\geq$ 99%) and MUA (95%) (2 mmol). This protocol has previously been published before but was used here with some modifications.[41] The mercapto-ligands were weighed out and stirred with 3 mL of toluene for 15 minutes. Then, 1 mL of a 10 mg/mL sample of the QDs in toluene was added. 0.7 mL of ammonium hydroxide (30%) was added to this mixture and this was further diluted down by adding 0.3 mL of deionised water. After 2 h of stirring, the QDs had moved to the aqueous phase (the coloured phase), and the top toluene phase was colourless. The aqeuous QD phase was washed by precipitation in ethanol, centrifugation and redispersion in 1 mL of water. The centrifugation was done at 10,000 RPM for 10 mins. The ligand exchange involving the MUA ligand failed to work while, the MPA ligand appeared stable initially, but the QDs precipitated out of the dispersion after storage overnight in the fridge. MSA was therefore used as a ligand for all of the below ligand exchanges due to its stability in dispersion for months after the ligand exchange.

Borate buffer method

This protocol has been published previously but used here with some modifications.[46] Butanol (800 μL), borate buffer (1 mL, pH 9, 0.2 M) and MSA/MPA (8 μL, 10 μmol) were added to the QDs (200 μL, 10 mg/mL) and this mixture was sonicated until the QDs changed phases. The QDs were purified using 10 kDa centrifugal filters and centrifuging at 15,000 rpm for 15 mins. It was found that the MPA-capped QDs precipitated out of the dispersion in a day again, whereas the MSA-capped QDs stayed stable in water for a few weeks while stored at 4°C.

EDA method

This protocol has been previously published and used here with some modifications.[56] The QDs were used at a concentration of 5 mg/mL. They were precipitated out of toluene using ethanol and redispersed in chloroform. EDA ($\geq$ 99%) (0.5 mL) was added to the QDs and stirred for 30 mins. Then, MSA (0.3 M) in 1 mL of deionised water was added which caused a phase separation. This was left stirring until the

phase transfer was complete (1.5 h). The aqueous QD phase was washed using precipitation and centrifugation.

TMAH method

A 0.2 M solution of MSA in 1 mL of deionised water was used. TMAH (25 wt % in water) was added to this until the pH of the solution was 11. The solution was then mixed with 1 mL of 10 mg/mL QDs in toluene for 2 h. The QDs were purified using 30 kDa centrifugal filters at 15,000 rpm for 20 mins.[92]

3.3.2 PEGylated ligands

Literature methods

Thiol-PEG-COOH (Nanocs Ltd., 2000 kDa) (8 mg) in 2 mL of chloroform was mixed with 100 μL of a 10 mg/mL QD solution in chloroform. This was stirred overnight after which the QDs were precipitated out with 5 mL of hexane and centrifuged at 10,000 rpm for 10 minutes.[94]

Three-step ligand exchange

This ligand exchange method was published recently.[65] Different concentrations of 100 μL ammonium chloride were mixed with 300 μL of *n*-methylformamide and 500 μL of acetone. This was added to 1 mL of the InP/ZnS QDs in toluene (20 mg/mL). This flocculated solution was vigorously stirred for 1 h and then centrifuged at 4800 rcf for 20 mins. The supernatant was discarded and an excess of acetone was added to the pellet and recentrifuged at the same settings as mentioned above.The pellet was then redispersed in 500 μL of NMF. These QDs were then washed with fresh hexane thrice and then precipitated using a 4:1 acetone:toluene mixture. The pellet was redispersed in 500 μL of NMF. These are further referred to as the chloride-capped QDs. Butylamine was then used as a capping molecule to transfer the QDs from NMF to chloroform. 200 μL of the above chloride-capped QDs were precipitated with varying amounts of butylamine (20, 30, 40 and 50 μL). They were then centrifuged at 20,000 rpm for 15 mins. The pellet was redispersed in 200 μL of chloroform. Finally, 50 μL of these chloride-butylamine capped QDs were mixed with

4.5 mg of thiol-PEG-COOH in 200 μL of chloroform for 10 mins after which the chloroform was evaporated off under vaccuum using schlenk techniques. The product was dispersed in 0.1 M NaOH (250 μL).

3.4 Characterisation

3.4.1 PL and UV-Vis

The Cary50 Bio (Agilent Technologies) was used to obtain absorbance measurements. The FLS980 (Edinburgh Instruments) was used for fluorescence and QY measurements using an integrating sphere. Before doing a fluorescence measurement, it was ensured that the absorbance of the sample was below 0.1 at the excitation wavelength.

3.4.2 Dynamic Light Scattering (DLS)

The ZetaSizer ZS90 (Malvern Instruments) was used for size and zeta potential measurements. Each measurement reported here was an average of 12 runs. The equilibration time for each sample was 2 mins and the temperature was set to 27°C.

3.4.3 TEM

For the water-based samples, the carbon-coated formvar grid was plasma cleaned for 5 minutes. Then, the sample was dropcasted onto the grid and left to dry for 30-45 minutes. After all the water has evaporated, the grid was washed with Milli-Q gently twice and further left to dry after blotting off excess water. This was then plasma cleaned again for 10 minutes. The TEM2100F (JEOL) was used for all imaging purposes.

3.4.4 Fourier-transform infrared spectroscopy (FTIR)

A 10 μL sample of QDs in their respective solvents be it water, chloroform or toluene was dropcasted onto the ATR (attenuated total reflectance) unit. This was left to dry before taking an IR absorbance measurement on the Alpha II FTIR Spectrometer (Bruker).

Chapter 4

Conjugation and Exosome Labeling

4.1 Background and motivation

The work in this Chapter has been published elsewhere by the author.[97]

The overall aim of this work was to produce InP/ZnS QDs for biological applications by making them water dispersible. The QD-MSAs produced in Chapter 3 were functionalised further with a biomolecule, such as an antibody (Ab) or aptamer. The carboxylic acid group on the surface of the QDs and the amine group present on the Ab or aptamer undergo carbodiimide coupling, the schematic for which is shown in Chapter 1, Figure 1.5. However, the challenge lies in achieving the highest possible reactivity and the ability to orient the biomolecules to be conjugated. Although the aptamer can contain a spacer so the orientation can only be one way, this reduces the efficiency of the conjugation as the fraction of "active" surface goes down. The orientation of attachment becomes more problematic for Abs, as they are proteins and can contain amine groups in the specific detection region as well.[71,98]

4.1.1 Confirmation of conjugation

In addition to the concerns outlined above, it is difficult to quantify the efficiency of the conjugation and optimise the purification process of QD conjugates to remove unreacted precursors (Ab, ligands or QDs). Han *et al.* used a sucrose density gradient to separate the QDs from the QD-Ab conjugates,[99] however, the low QY of InP/ZnS QDs and the diluted final product can create issues with detection using confocal microscopy or other fluorescence-based detection techniques. Therefore, to confirm the presence of conjugates, a number of techniques can be used. While largely a qualitative phenomenon, an increase in fluorescence intensity was reported upon conjugation of the Ab to a QD due to the Ab enhancing the fluorescence, so a change in intensity could be one indication of binding.[100] Gel electrophoresis can also be used to separate the different sizes in samples and thereby verify the presence of the conjugates.[101] DLS is another popular method to verify binding of the QDs to the Ab,[42,102] as attaching more compounds to the surface should lead to an increase in the hydrodynamic radius of the particles. Additionally, there should also be a change in the zeta potential of the QD with the change in surface chemistry. In Chapter 3, this parameter was related to stability of final water-dispersible QDs.

However, a change in zeta potential of the same particles denotes a change in the surface environment which can confirm attachment.[103]

4.1.2 Surface plasmon resonance

While the techniques above are useful for qualitative analysis, the use of surface plasmon resonance (SPR) spectroscopy should be a more quantitative method. The theory behind SPR depends on gold containing a sea of delocalised electrons within its lattice. The oscillation of these free electrons in metals is collectively known as a plasmon. When light hits the metal, the plasmons within the gold get excited. Usually, with the help of a prism, the light source is incident on the surface of the gold at a range of angles where total internal reflection can occur. The excited plasmon, at a certain resonant angle of incident light, causes a decrease in the intensity of the reflected light. The angle at which this decrease in intensity occurs is called the angle of resonance which changes based on changes occurring on the gold film (binding, adsorption, desorption). Therefore, SPR is a highly sensitive method to detect binding and the gold can further be functionalised further to allow for the immobilisation of antibodies or aptamers.[104] Here we used a commercial SPR device known as the Biacore X100 (GE Healthcare, Ltd.) which consists of a flow cell system. It converts the change in resonance angle from the differing surface environments to a change in response units upon binding of different molecules.

4.1.3 Detection of exosomes

SPR has been used in literature to detect exosomes in a clinical setting.[23,32,105] Grasso *et al.* showed that it was possible to generate large signals using SPR for the capture of exosomes. Sina *et al.* used SPR as a method to first detect bulk exosomes, and then used a breast cancer marker (HER2) to detect the proportion of the exosomes, that contained this marker. Rupert *et al.* used the Biacore instrument to quantitatively discern the exosome concentration by converting the SPR response into surface-bound mass. Interestingly, modifications to the systems above by incorporating QD-Abs can lead to signal amplification,[100] thereby making it possible to detect the dilute concentrations of exosomes that exist in raw biological fluids.

A sandwich-assay has been used previously, where the detection of all exosomes was done first, and then, using a tumour-specific Abs, the sub-population of the tumour-related exosomes was found.[32] A similar assay was done using QD-Abs for the detection of proteins, and should therefore be able to be applied to exosomes as well to lead to signal amplification.[100]

As expected, the work presented in the rest of this chapter showed only a small SPR shift for the attachment of the aptamer, as it is a small molecule when compared to an Ab. The resulting binding of the exosome to the aptamer was therefore not tested. As opposed to this, the binding of the exosomes to the QD-Ab conjugates was tested using SPR. This binding could also be confirmed using confocal microscopy. As the confocal microscope cannot be used for imaging the exosomes due to its low-magnification, protein-absorbing 4 μm beads were used to confirm the binding, the details of these will be mentioned below.

4.2 Results and Discussion

EDC/NHS coupling was used to attach the Ab or aptamer to the QD in a method described in Section 4.3. After the conjugation, the PLQY increased from the 6.56% of the orignal QD-MSA to 8.63% for QD-Aptamer and 13.12% for QD-Ab samples. The antibody QY is minimal and this was not investigated. Shown in Figure 4.1, there are also slight changes in the emission peak maximum of the QD-Ab compared to the original QD-MSA, but the overall shape doesn't appear to have changed too much. This means that the protocol used did not produce any more surface defects as was observed with the initial ligand exchange.

The difference in the amount of solvent displaced by the particles is more evident after the conjugation. Therefore, to prove that the biomolecules had conjugated to the QD, DLS was done. This showed an increase in size, as expected, from 40 nm (QD-MSA) to 70 nm (QD-Ab) (Figure 4.2). Interestingly, there was decrease in hydrodynamic size observed for the QD-Aptamer. The hydrodynamic size for the QD-Aptamer decreased to 20 nm, and the DLS measurement for this was quite varied through the course of 12 measurements. This could be a reflection of the way the

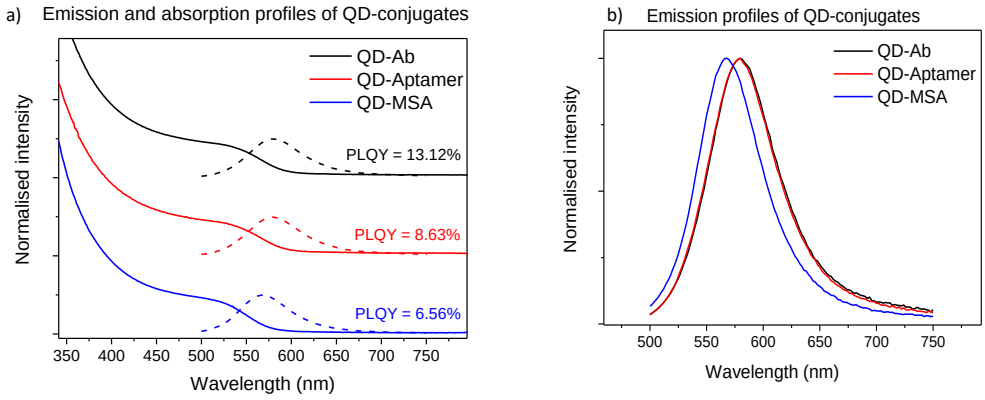

FIGURE 4.1: (a) Emission and absorption profiles of QD-conjugates. (b) Emission differences in QD-conjugates

Sample name	Zeta potential (mV)
QD-MSA	-40.08
QD-Ab	-7.53
QD-Aptamer	-15.5

TABLE 4.1: Table of zeta potentials for QD-conjugates at pH 7.

aptamer (which is a chain of nucleotide bases) varies its orientation when in solution and when attached to the QD as well.

Further evidence of the synthesis of QD conjugates was observed from the zeta potential measurements of the sample. Zeta potential reflects the net electric charge around the particle and a change in the surface environment of the nanoparticle would be detected through these measurements. The observed zeta potentials for QD-MSA, QD-Ab and QD-Aptamer conjugates were -40.08 mV to -7.53 mV and -15.5 mV, respectively (Table 4.1). The magnitude of the zeta potential measurement reflects the stability of the dispersion, therefore, it was found that the coupling reaction destabilised both the conjugate dispersions significantly. This is why it was important to have an initially stable dispersion made using an appropriate ligand exchange and was only achieved using the QD-MSA made using the ammonia method.

The THP-1 cell-line was used for the isolation of THP-1 exosomes. This cell line is derived from an acute leukemia patient and therefore, the exosomes isolated from this contain cancer markers on them. The exosomes were then characterised using

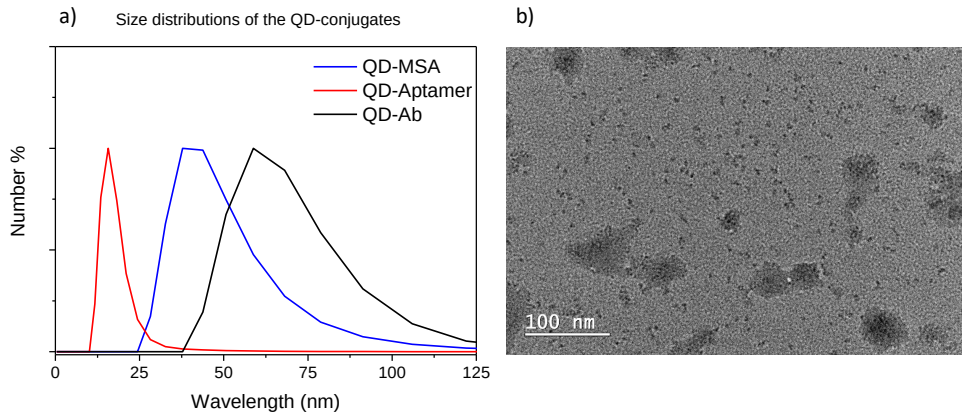

FIGURE 4.2: (a) Size differences as reported by DLS of the QD-conjugates. (b) TEM2100F image of QD-Ab

DLS which yielded a size of 37.8 nm (Figure 4.3(a)). TEM images (Figure 4.4(b) and (c)) confirm the presence of spherical shaped vesicles between 40-50 nm in size. The discrepancies in the measurement of size and imaging the exosomes arise from differences in storage. The exosomes were frozen and stored at -20 °C right after their isolation. Once thawed, they cannot be frozen again but can be refrigerated for 1 week. The effect of storage in the fridge was observed on DLS as well as TEM. DLS measured a size of 0.63 nm for the same sample that was previously 40-50 nm (Figure 4.3(b)). TEM imaging of this sample also showed that the spherical particles, were now different in shape as seen in Figure 4.4(a).The thawing or storage under a different temperature makes these particles unstable and could give rise to unreliable results in terms of the DLS size of 0.63 nm and function which in turn, would affect their measurement.

After this, the THP exosomes were incubated with QD-Ab for 2 h and a population size of 32.7 nm was measured using DLS (Figure 4.3(c)). This was smaller than the previous size of 37.8 nm for exosomes alone. For further confirmation of attachment, the size by intensity data was used. This plot shows two different populations - one at 50.7 nm and one at 295 nm (Figure 4.3(d)). The size by intensity plot of just the THP exosomes themselves also shows a population at around 300-400 nm in size, which could either indicate larger particles (dust) or microvesicles. A size measurement of 50.7 nm could therefore be attributed to the QD-Ab-THP exosome conjugate.

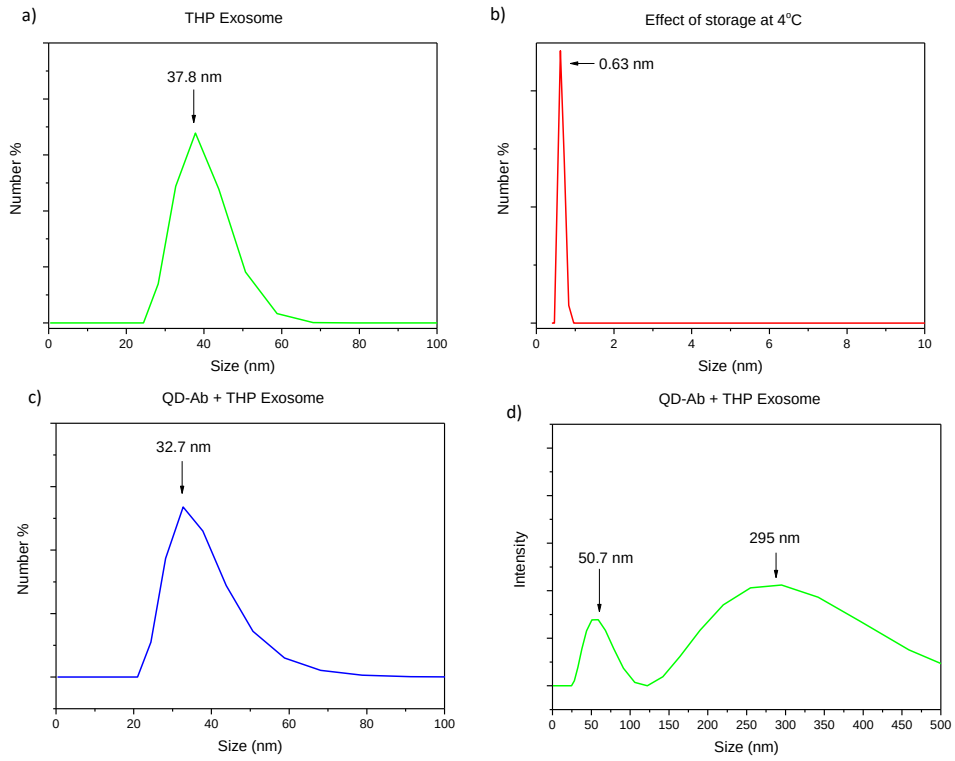

FIGURE 4.3: (a) Size of THP exosomes as measured using DLS. (b) Effect of storage of the exosomes in the fridge for a week. (c) A number % of size for a mix of QD-Ab and THP exosomes (d) Intensity-based distribution of a mix of QD-Ab and THP exosomes.

A similar measurement did not give reliable results for the QD-Aptamer-THP exosome conjugate. To confirm attachment for this the QD-Aptamer-THP exosome sample was imaged using the TEM2100F (seen in Figure 4.4(b) and (c)). While this showed the exosomes surrounded by particles of the correct size and shape, it is hard to prove that the binding to the exosome actually happened using TEM. However, the vesicles look darker with QDs mixed in the sample.

4.2.1 Detection of THP-1 exosomes using SPR

To confirm whether binding of the QD-conjugates to the exosome was actually occurring, SPR was used. The Biacore X100 uses the concept of SPR and has a constant flow-cell over a gold chip. It therefore converts the change in the SPR angle at which there is a drop in intensity of the reflected light to a change in response from the baseline after binding. The commercially available carboxymethyldextran-terminated gold chips (CM3) were used for this purpose. Figure 4.7 shows the method used for

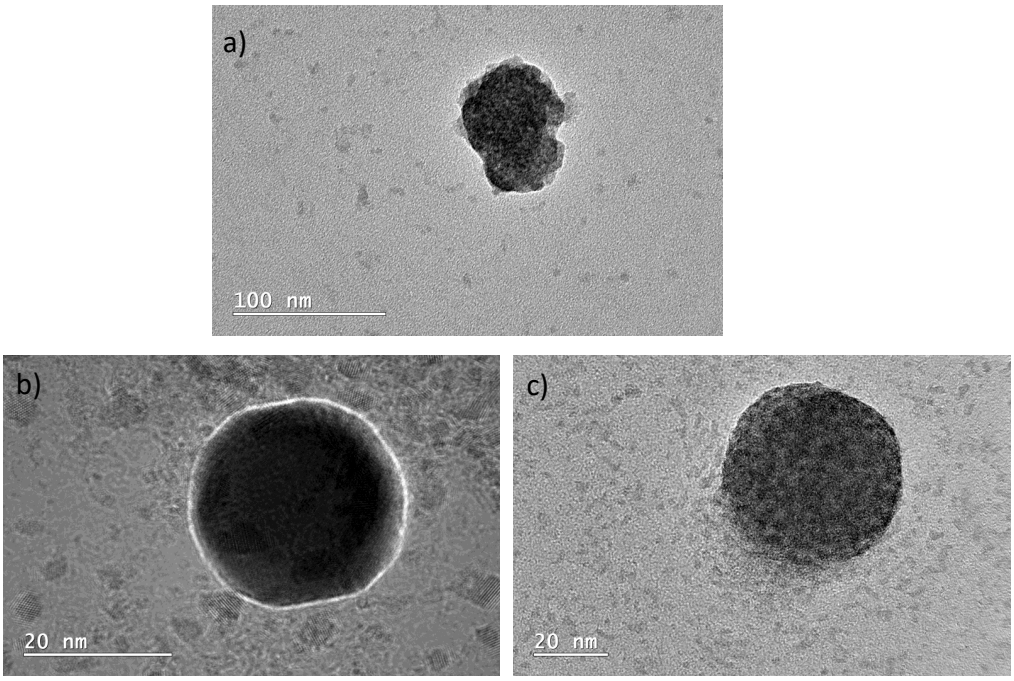

FIGURE 4.4: (a) TEM2100F image of a broken exosome (after storage in fridge for 1 week). (b) and (c) TEM2100F image of QD-Apt and THP exosomes.

the functionalisation of the CM3 gold slide on the Biacore X100. Further EDC/NHS coupling with a secondary Ab was done to permanently immobilise the targeting agent on the surface. Using a secondary Ab enables the detection of the primary Ab and provides a reusable gold surface, as the Ab-Ab interaction can be broken with a simple regeneration using an acidic buffer. The covalent bond made through this process cannot be broken and is not affected with the regeneration cycles. As the secondary Ab is specific for the primary anti-CD63 Ab, a binding event should lead to an increase in the relative response. Therefore, just the Ab on its own led to a response of close to a 100 R.U (Figure 4.6). Because the responses depend on the mass of the molecule attached to the surface and can scale according to this, it was expected that the response of the QD-Ab conjugate would be significantly higher due to the QD attached to the Ab. This was confirmed through the response of the QD-Ab, which was controlled so both injections had the same Ab concentration of 5 μg/mL. The response from this attachment was at 1400 R.U. and proved the viability of this detection method.

Figure 4.5 shows the plot for the immobilisation of the anti-mouse secondary Ab on the CM3 chip. Usually, a pre-concentration test is done first. In this test, the secondary Ab was dispersed in a pH 4.5 sodium acetate buffer, which ensures the carboxyl-groups of the surface are deprotonated while the amine-groups of the Ab are protonated. This is because the caboxylic acid has a lower pKa value compared to the amine, which means that it is easier to deprotonate. This improves the efficiency of the conjugation to the gold surface by drawing the two components together electrostatically and allows for the localisation of more antibodies. After this, an EDC/NHS mixture is injected, which activates the carboxyl groups and forms the covalent amide bond. This is shown in Figure 4.5 with the increase in response units as NHS-esters are formed. After this, the ligand is constantly injected over a time period in pulses. After a pre-set value of response units is reached, any unreacted NHS-esters are blocked off by using a small-molecule amine (ethanolamine). This leads to a huge rise in response units that reduces down as the the excess reagents are washed off the surface at the end of the run. The completed immobilisation then has a net response signal of $\sim$3000 R.U.

Finally, for the detection of the exosomes, two different methods were used, which have been outlined in Figure 4.7. For the exosomes isolated from a THP cancer cell culture, a pre-incubated mixture of primary Ab/QD-Ab and exosome were injected onto the secondary Ab-functionalised surface. The exosome concentration was varied, while the QD-Ab or Ab conc was kept the same.

For the detection of THP exosomes, it was expected that as their concentration increased, it would lead to an increase in response as more exosome-Ab conjugates bind to the surface. Instead, Figure 4.8 shows the response decreases as the concentration of exosomes increases, with the lowest concentration having the highest response and the highest concentration having the lowest response. This trend is further completed when a solution of just the QD-Ab at the same concentration as all the other samples is injected which shows a significantly higher response at 1400 R.U.. The mixture of the primary Ab and THP exosomes showed a similar pattern where as the THP exosome concentration was increased, there was a decrease in the response (Figure 4.9).

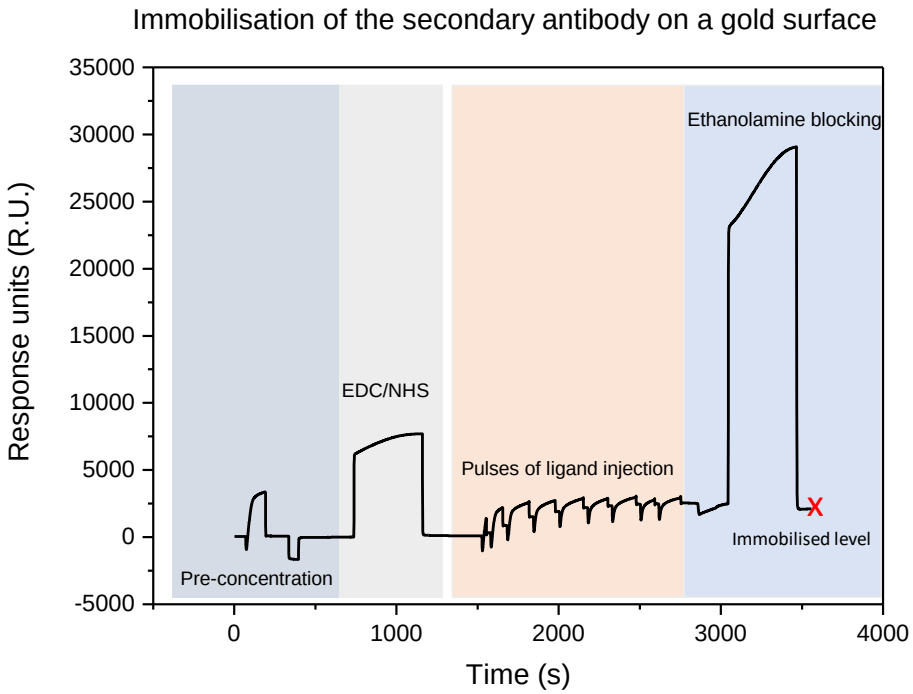

FIGURE 4.5: Response plot of the secondary Ab immobilisation on a gold chip

The possible explanation for the decrease in response with increasing concentration is because the surface is possibly responding to reduced binding with each increasing concentration, which turns into an inhibiting response rather than a binding response. With the lowest exosome concentration and the same Ab concentration of 5 μg/mL, there are more antibodies that do not bind to the THP exosome, and therefore bind to the secondary Ab on the gold surface. This increased amount of "free" primary antibodies then shows an elevated response. A control study ensured that the secondary Ab itself does not respond to the THP exosomes (Figure 4.10).

An alternative explanation for this inhibition behaviour could be due to the presence of more CD63 proteins embedded in the membrane of these cancer-cell derived exosomes as was seen by Sharma *et al.* who showed using AFM that cancer exosomes show increased CD63 surface densities.[22] This means that possibly a lot more antibodies are binding to a single exosome in this case. This could further cause a significant change in the size of the particle being detected. The inhibiting response

could therefore be caused from a simple steric hindrance due to a larger complex (exosome attached to multiple antibodies) being detected. This also means that there is absolutely no binding of the Ab-exosome complex to the surface, as the response is based on a change in mass. Therefore, with an exosome on the gold surface, the response should have been higher than the Ab on its own. As it is known that the Ab binds to the secondary Ab, it is possible that the exosome inhibits this binding completely due to a difference in surface chemistries or steric hindrances that may prevent the interaction with the surface.

To further prove the hypotheses above for the reverse trend observed here, several studies may need to be facilitated. These include comparisons of surface chemistries and morphologies of cancer-cell exosomes with normal exosomes. This would explain if the exosomes are in fact inhibiting the binding between the primary Ab and the secondary Ab due to a sterically hindering morphology as has been claimed above. While, TEM did not show any differences between the morphology observed between the two types of exosomes, other types of microscopy such as AFM could offer a better quantitative and qualitative look at the differences in surfaces, morphology and binding between the antibody and the exosome as has been previously studies in the literature.[73]

4.2.2 Detection of saliva and breath exosomes using SPR

The saliva and breath exosomes were isolated from raw samples of the author's saliva and breath condensate. This was rid of cell debris, and then they were precipitated out using the Rosetta Exolute kit. A different isolation strategy was used for these because it is difficult to obtain high concentrations of these samples using the size column. The Rosetta Exolute kit uses a precipitation method to achieve higher concentrations of exosomes. This was then imaged using the TEM2100F, and as can be seen from Figure 4.11, the saliva exosomes are around 50-60 nm in size. This is further confirmed by DLS (Appendix C). Interestingly, the breath exosomes are around 70-90 nm in size, which may already indicate they have different cellular origins.

The detection of breath and saliva exosomes by the QD-Ab conjugate was then

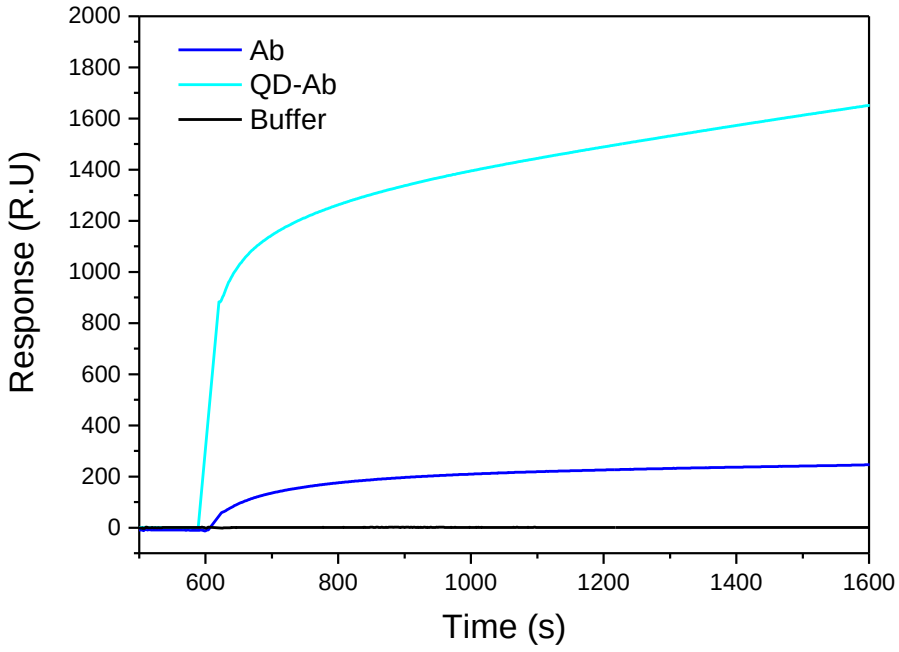

FIGURE 4.6: SPR response after capture of an Ab and a QD-Ab onto a Au chip coated with a secondary Ab.

tested using SPR. However, instead of injecting a pre-incubated mixture of Ab and exosome, a step-wise injection of Ab or QD-Ab first, and then the exosomes at different concentrations was done.

The breath and saliva exosome injections resulted in the predictable responses of an initial rise in response with the capture of the QD-Ab conjugate followed by an increase in response units as higher concentrations of exosomes were injected. This is shown in Figure 4.12, where the highest concentration of 0.1 mg/mL with the saliva exosomes gave rise to a response of about 200 R.U. whereas for the breath exosomes, this yielded a response of 40 R.U. The concentrations shown for the exosomes are total protein concentrations and not particle/mL concentrations. Therefore, for a protein concentration of 0.1 mg/mL, it is possible that there is a higher number of exosomes/mL in saliva compared to the breath. To ensure that no binding was happening between the secondary Ab and the exosomes, these exosomes at different concentrations were also injected directly onto the secondary Ab functionalised surface. This is shown in the Appendix Figure C.3 where all of the concentrations lead to a maximum response of 21 R.U. only. The above experiments function as

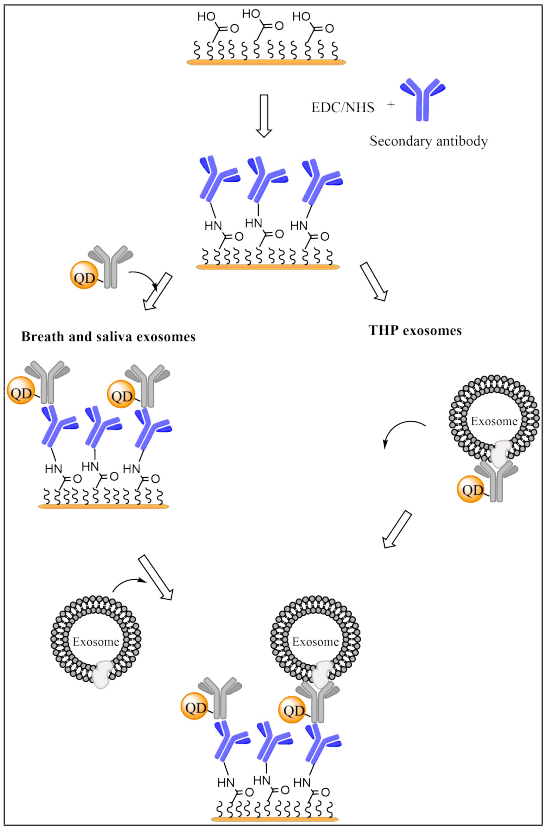

FIGURE 4.7: Method used for the functionalisation of the gold slide

a proof-of-concept that the QD-Ab conjugates are able to detect the exosomes from biological fluids. Furthermore, this could be applied to a more complex assay to allow for the characterisation and identification of different protein markers in the membrane of the exosomes.

This step-wise assay was tested using the THP exosomes, but it resulted in negative responses as is shown in Appendix C (Figure C.4). The figure demonstrates the binding of the antibodies first, after which the different concentrations of THP exosomes are injected. The smallest concentration gives rise to the smaller dip (50 R.U.), as opposed to the largest concentration which gives rise to the largest dip of nearly 1000 R.U.. This response indicates that the inhibition follows a trend with the concentration injected.

This difference in the trends of binding response between the breath and saliva exosomes and those derived from the cancer cell-line could be due to the difference in surface chemistries as has been suggested previously. This difference in chemistries could further arise from the different methods of isolation used for both

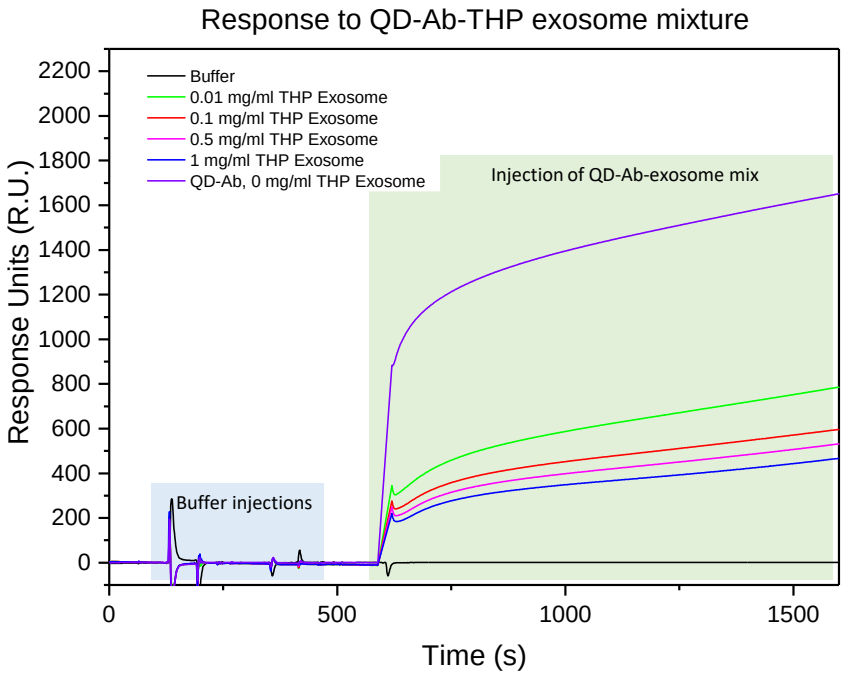

FIGURE 4.8: Detection of a mixture of QD-Ab and THP exosome on the secondary Ab-functionalised gold chip

the exosomes. For the THP-1 exosomes, the qEV size column was used. As opposed to this, for the isolation of the breath and saliva exosomes, the Rosetta ExoLute kit was used. The ExoLute kit contains a precipitant (unknown chemical composition) that causes the precipitation of the exosomes within the solution. As opposed to this, the qEV is just a size-exclusion column. Therefore, the precipitation-based method could change the surface environment of the exosomes and cause one type of exosomes (breath and saliva) to be more attracted to the negatively charged gold surface due to a more positive charge on their surface. As opposed to this, the size column causes a retention of the original, negative charge of the exosomes, which gives rise to the inhibition response as the like charges repel. To further explore whether this is the case, the isolation of the breath and saliva exosomes using the qEV kit and their subsequent detection could be done. Additionally, the measurement of their zeta potential using NTA could also prove to be useful. While, it is possible to use the ZetaSizer for this purpose, the high ionic conductivity of the buffer system that the exosomes are dispersed in can cause the electrodes to disintegrate.

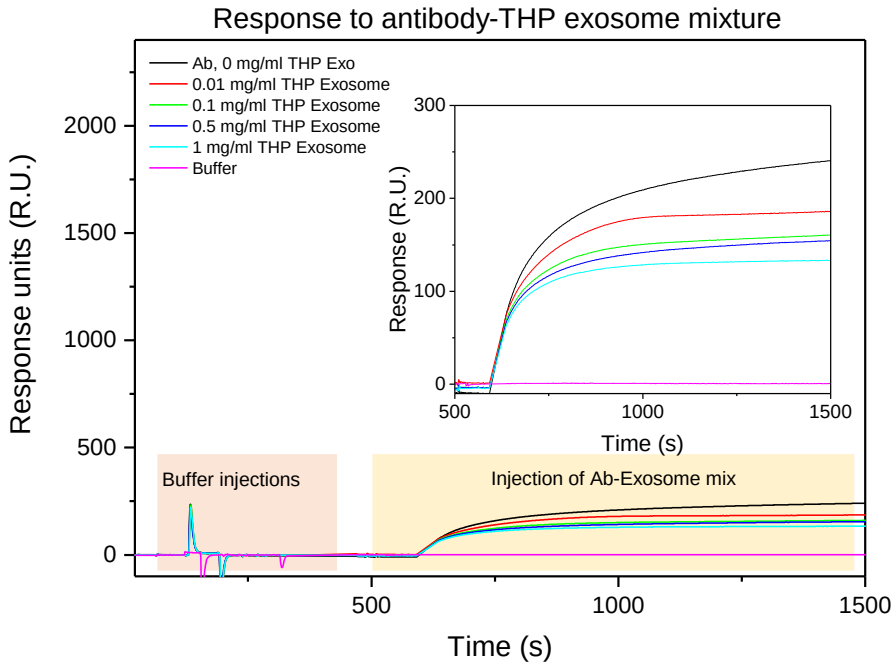

FIGURE 4.9: Detection of a mixture of Ab and THP exosome on the secondary Ab-functionalised gold chip

4.2.3 Confocal microscopy using aldehyde/sulfate beads

Further testing of whether the QD-bio-molecule conjugates binds to the exosomes was done using confocal microscopy. As the confocal microscope cannot go to high enough resolutions to image exosomes, aldehyde/sulfate latex beads of 4 μm size were used instead, as their larger sizes would be visible. These are commercially available and are made from polystyrene chains, which in turn, makes the microspheres inherently hydrophilic. The beads can also absorb proteins quite easily due to the high amount of aldehyde groups on the surface of the beads. The conjugation of the aldehyde to amine groups on the protein can then take place in a single step spontaneously. Additionally, they can be collected by centrifugation at a low rpm and washed with clean water or buffer.

Figures 4.13 and 4.14 show a complete summary of the different samples that were run on the confocal microscope. The beads themselves were fluorescent, as seen in Figure 4.13(a), so the laser power was kept at a level where minimal fluorescence could be seen from the beads and this setting was run for all the other

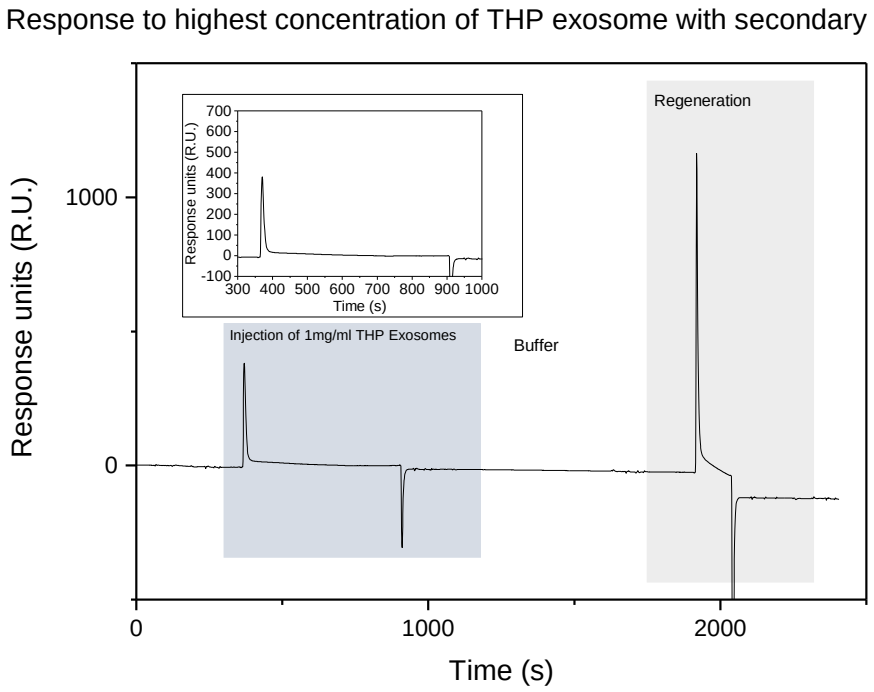

FIGURE 4.10: Response of the gold chip with secondary Ab to the highest concentration of THP exosomes

samples. Therefore, comparisons should be able to be made between each image based on the relative intensities-per-area which are outlined in Appendix C (Table C.1). The pixel intensities were obtained using the ImageJ software where the background intensities were averaged and divided by the selected area of interest. Similarly, a box was drawn around each of the beads, and the intensity for this was averaged and divided by the respective area. For the selected laser strength, the beads show a high intensity/cm^2 (26.62 intensity/cm^2) compared to their background (9.23 intensity/cm^2).

Figure 4.14(a) shows a solution containing the beads and QD-MSA-labelled saliva exosomes. Here, the QD-MSA/raw saliva mixture was put through a qEV size column to isolate the saliva exosomes before mixing with the beads. The fractions that were meant to have exosomes were collected, therefore, some of the exosomes non-specifically bound to the QD-MSA would also be present. The beads further attached to proteins found on the exosome's membrane, leading to specific fluorescence seen originating from the beads. This was further reflected by the intensities by area which showed the QD-MSA labelled exosomes to be at 8.24 intensity/cm^2

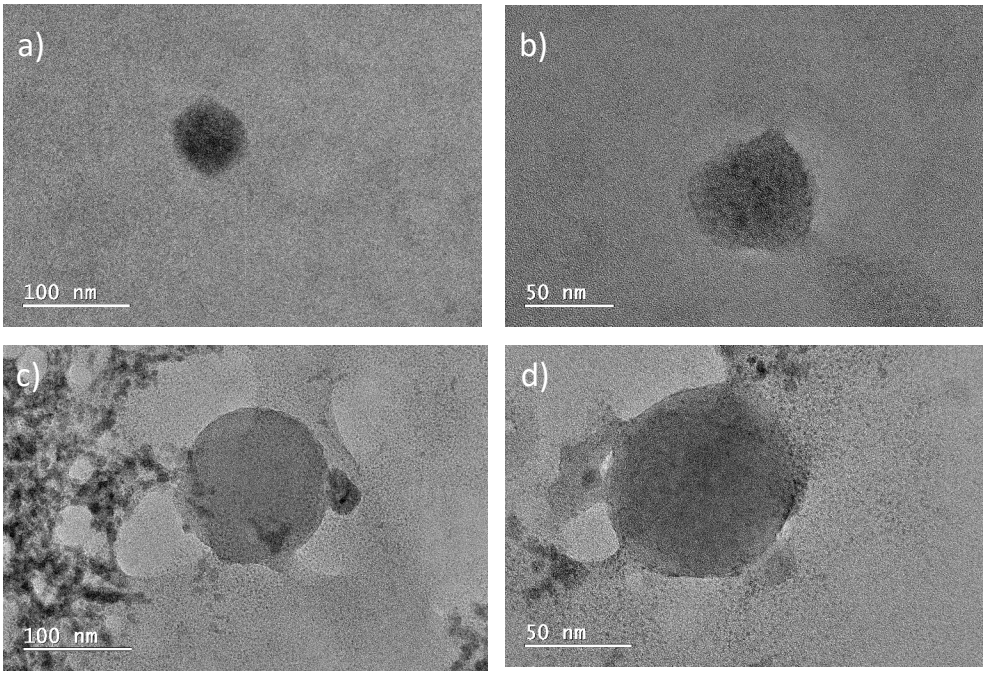

FIGURE 4.11: TEM2100F image of saliva ((a) and (b)) and breath ((c) and (d)) exosomes

with the background at 0.09 intensity/cm^2. This is important because this highlights that non-specific binding is happening, however it also is a method that can be used to label exosomes for further fluorescence studies without the need of a specific targeting biomolecule. Due to the above reason, this method could not be used as a way to confirm that the QD-Ab conjugate or the QD-Aptamer conjugate could target the exosomes.

Figure 4.14(b) shows QD-MSA that had been incubated with saliva exosomes for 2 h before being mixed with the beads. While the first image was taken after 2 h of mixing (called unwashed), the other is a washed sample where the beads were centrifuged and the supernatant was discarded. Anything that bound to the beads would collect at the bottom of the tubes, and anything that did not bind would be lost in the supernatant. In the unwashed sample, there is excess fluorescence originating from the QDs which are freely in solution and therefore, the background is high (15.91 intensity/cm^2 for the beads and 9.53 intensity/cm^2 from the background). The washed sample shows lower background fluorescence (0.02 intensity/cm^2), and very little fluorescence originating from the beads (2.85 intensity

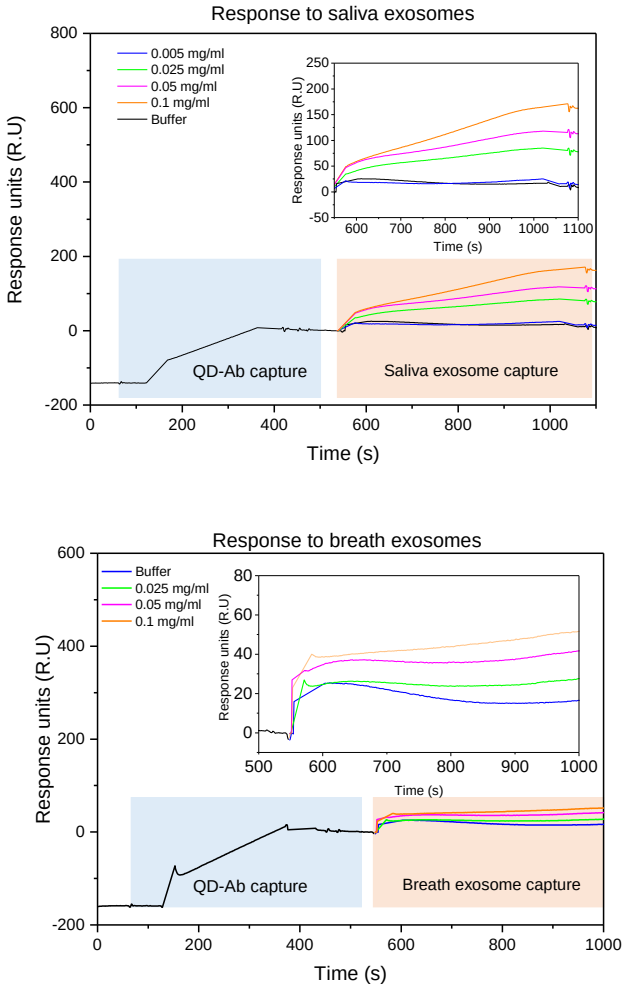

FIGURE 4.12: Detection of different concentrations of saliva (top) and breath exosomes (bottom) using the QD-Ab conjugate and a step-wise immobilisation assay.

/cm^2) which indicates that QD-MSA did not attach to the beads. This was expected, as there are no amine groups on the QDs to attach to the beads. Any fluorescence inside the beads can therefore be attributed to extremely low non-specific binding or the inherent fluorescence that was measured from the beads at that laser strength.

While the QD-MSA are able to label the exosomes (when incubated and collected using a size column), the use of a targeting agent should greatly enhance this. Further to this, it should make the process of targeting easier to view using confocal microscopy techniques as the exosomes and the QD-conjugate can just be mixed together.

It was expected that the QD-Aptamer sample would not bind to the beads at

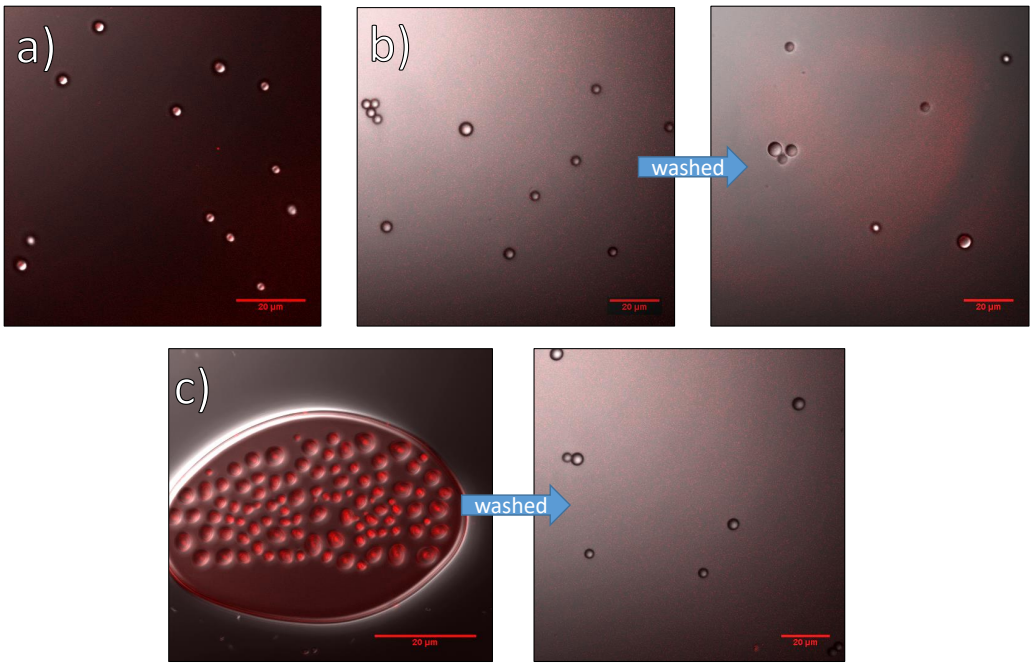

FIGURE 4.13: a) 4 μm aldehyde-latex beads fluorescing using a 480 nm laser. This was used as the base fluorescence for all the other images. (b) QD-Aptamer mixed with aldehyde-latex beads (unwashed and washed) (c) QD-Ab mixed with aldehyde-latex beads (unwashed and washed)

all on their own. When mixing just the two together with no exosomes present, Figure 4.13(b) show little specific fluorescence originating from the beads which is further confirmed by the intensities (Table C.1) where the beads have an intensity of 0.63/cm^2 and the background has an intensity of 0.01 per cm^2. The washed sample showed a slightly higher pixel intensity of 2.94 /cm^2 with the similar background intensities.

It was expected that the QD-Ab sample would attach to the beads on their own because of antibodies on the QD, and this would show through on the confocal microscope. But as seen with the mixture of just QD-Ab and aldehyde beads in Figure 4.13(c), this was not what occurred. While the unwashed sample showed non-specific and more concentrated fluorescence originating from the beads (9.68 intensity/cm^2) compared to the background (1.00 intensity/cm^2), the washed sample showed no specific fluorescence at all (0.32 intensity/cm^2) which showed that the QD-Ab do not bind to the beads and get washed away. Because the fluorescence of the beads in this sample was the least, these materials were further investigated.

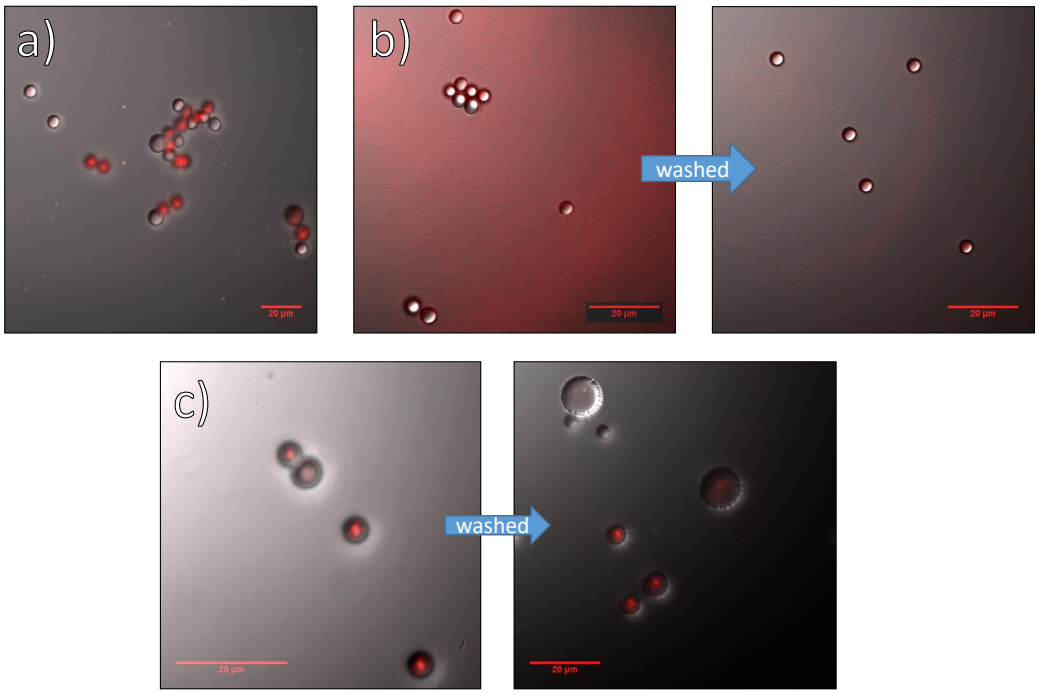

FIGURE 4.14: (a) QD-MSA labeled exosomes with the beads. This was using a mixture of QD-MSA and raw saliva flowed through a qEV size column to isolate QD-MSA labelled exosomes. (b) QD-MSA unwashed and washed with saliva exosomes (just mixed and incubated) with beads. (c) QD-Ab + saliva exosomes unwashed and washed (just mixed and incubated).

As the mix of QD-MSA and saliva exosomes (Figure 4.14(b)) showed little fluorescence from the beads, mixing QD-Ab with the saliva exosomes was done to see if this would lead to specific fluorescence. This is shown in Figure 4.14(c), where both the washed and unwashed sample showed a large amount of fluorescence originating from the beads (37.45 intensity/cm^2 and 29.51 intensity/cm^2 respectively) with little background fluorescence. As neither the beads-only or QD-Ab/beads samples gave rise to specific fluorescence, the bright emission has to be attributed to the binding of the QD-Abs to the exosomes, and their subsequent binding to the beads. This is a promising confirmation of the targeting abilities of the antibody and the retention of its targeting abilities post-conjugation to the QD. Future work would therefore involve using this as a rapid and easy method of confirming binding and confirming the presence of the exosomes in the sample.

A similar process was followed with the QD-Aptamer conjugate and exosomes,

but this did not show any fluorescence whatsoever with and without washing. Further to this, the conjugation of the QD-Aptamer similarly using Biacore X100 did not work, as the oligo was too small for a significant signal after attachment or immobilisation.

To conclude, different methods were used to test the binding between the QD-Ab and the exosomes. DLS showed an initial proof of binding with an increase in size for the QD-Ab conjugate and THP exosome mixture. Further to this, SPR was used to show an inhibiting behaviour for the THP-1 exosomes, with increasing concentration and decreasing response. This differed from the response direction for the breath and saliva exosomes, which showed an increasing response to increasing concentrations. This could further be applied to investigate the reason behind the difference in behaviour between the two types of exosomes. Confocal microscopy with aldehyde/sulfate latex beads was also done to probe how effective the imaging with the QDs would be. This showed specific fluorescence originating from the beads for the QD-Ab conjugates that were mixed with saliva exosomes. A similar protocol followed for QD-MSA and QD-Aptamer showed no such specific fluorescence. Furthermore, QD-MSA-labelled exosomes also showed specific fluorescence on the beads, which could be another method for the fluorescent labelling of the exosomes that does not rely on specific target molecules.

4.3 Materials and methods

All reagents were purchased from Sigma Aldrich, unless specified otherwise.

4.3.1 Conjugation of the biomolecules to the QD

For the conjugation of the biomolecules (antibody (Anti-CD63 antibody [TS63] (ab59479) purchased from Abcam and aptamer CD63 purchased from Integrated DNA Technologies with the sequence (NH_2C_6CAC CCC ACC TCG CTC CCG TGA CAC TAA TGC TA)) to the QD, EDC/NHS coupling was used. EDC (0.0 2M, 100 μL) and NHS (0.05 M, 100 μL) were added to a 1 mg/mL solution of the QDs (1 mL). This was then left to stir gently for 10-15 mins. After this, 10 μL of the biomolecule at a concentration of 1 mg/mL was added. This was further left to stir for 2 h. The QD-conjugate

was cleaned using 100 kDa centrifugal filters (if the conjugate was an Ab) or a 30 kDa centrifugal filter (if the conjugate was an aptamer).

4.3.2 Exosome isolation

THP exosomes were isolated from cell culture media using the qEV size columns by Deanna Ayupova.

Saliva samples of 6 mL were taken after having not consumed any food or drink for 2 hours. This was then centrifuged at 2000 g for 5 mins and 20,000 g for 20 mins to get rid of any cell debris. The supernatant was diluted in 1X phosphate buffered saline (PBS) (1:1). Breath condensate was collected using a syringe connected to a collection tube. The entire apparatus was wrapped with frozen gel packs wrapped and was frozen in liquid nitrogen before sample collection. The condensate that was collected was filtered using a 0.22 μm syringe filter. Rosetta ExoLute (Rosetta Exosome Inc.) kits were then used for the isolation of both the above exosomes following the manufacturer's protocols.

4.3.3 Characterisation

PL and UV-Vis

The Cary50 Bio (Agilent Technologies) was used to obtain absorbance measurements. The FLS980 (Edinburgh Instruments) was used for fluorescence and QY measurements using an integrating sphere. Before doing a fluorescence measurement, it was ensured that the absorbance of the sample was below 0.1 at the excitation wavelength.

SPR

The Biacore X100 was used for all of the SPR measurements. The flow rate used for all measurements was 5 μL/min. A secondary Ab was immobilised on a CM3 chip using 0.4 M EDC and 0.1 M NHS. All the experiments using an active and a reference flow cells which was kept blank to allow for refractive index changes from different solvent systems.

THP Exosome detection A mixture of QD-Ab (at a constant concentration) and THP exosomes (at varying concentrations) was injected for 18 mins. The same method was applied to the mixture of Ab and THP exosomes as well. The CM3 gold surface was regenerated using a pH 2.5 glycine-HCl solution to wash away any bound exosomes, primary antibodies and QD-Ab to leave a surface with just the secondary Ab again.

Breath and saliva exosomes For the breath and saliva exosomes, QD-Ab was first injected onto the gold slides at the same concentration. Then different concentrations of the breath and saliva exosomes were injected.

4.3.4 TEM

The TEM2100F (JEOL) was used for imaging at 200 kV. 10 μL of the sample was dropcasted on a carbon-coated copper grid. For any samples with buffer and exosomes, this was left until most of the water had evaporated. Then, 2% uranyl acetate was used for staining the biological samples in the dark for 6 mins. After this, the uranyl acetate and the grid were washed several times with Milli-Q water and left to completely dry.

4.3.5 DLS

The ZetaSizer ZS90 (Malvern Instruments) was used for size and zeta potential measurements. Each measurement reported here was an average of 12 measurements. A standard dip cell (Malvern Instruments) was used for zeta potential measurements.

4.3.6 Confocal microscopy

The Olympus FV1000 laser scanning confocal microscope was used for confocal microscopy. The 488 nm laser was used for excitation. Each sample was incubated with 4 μm aldehyde/latex sulfate beads overnight.

Chapter 5

Conclusions and Future Outlook

5.1 Summary

In conclusion, it was shown that InP/ZnS QDs can be used as an alternative to Cd-based QDs for the purposes of detection of EVs. Due to the ease of sample collection, targeting these vesicles have countless applications in the detection of diseases. There are a variety of biomarkers that exist on the exosome membrane, as well as internally (i.e. RNA, DNA, and proteins) that offer an abundance of information to understand.

However, in order for these results to be cohesive, there is a need to standardise the characterisation of exosomes as well as search for different detection systems. This work begins to solve this problem because it provides a groundwork towards targeting the markers on the exosomes and provides future scope with multiplexing abilities using the QDs size dependency as a barcode. Furthermore, it also opens the possibility of using InP QDs as a less toxic alternative to its cadmium counterparts.

In the beginning of this work, the InP/ZnS QDs were synthesised and characterised using a variety of techniques such as TEM, PL, and UV-Vis. The low contrast of the QDs meant that purification and sample preparation had to be optimised to enable TEM imaging. It was found that using a size column prior to imaging aided in visualisation of nanoparticles, however, this also significantly reduced the QY due to the stripping of the ligands from the surface. The low contrast also gave rise to inaccuracies with the measurement of the size using TEM. The errors from this potentially affected the resulting investigation of the dependency of the size of the energy of the exciton and extinction coefficient. From AAS and TEM, it was also shown that the energy of the band gap is inversely proportional to the particle size as opposed to the square of the diameter as predicted by EMA. This followed the observations in previous theoretical investigations conducted by Cho *et al*. Further to this, the size dependency was extended to core/shell QDs as well, as the exciton energy is affected by the environment of the core.

The hydrophobic oleylamine ligands on the QD were then exchanged with hydrophilic ligands to render the QDs water soluble. This has been challenging to achieve in literature due to the loss in QY of the resulting QDs, and the low resulting colloidal stability. It was shown that a basic environment is essential for the ligand

exchange, however a stronger base such as ammonium hydroxide and a ligand with two carboxy acid groups (MSA) resulted in QDs with a lowered QY, but exceptional colloidal stability with zeta values of -40.08 mV. As opposed to this, other ligand exchanges such as those based on EDA, borate buffer, or TMAH result in lowered QYs as well as less colloidal stability. The use of a multiple-step ligand exchange and polymeric PEG-based ligands was also attempted, where it was found that a molecule with a thiol and amine groups worked best. Using a molecule with thiol and carboxy functional groups such as MSA resulted in QDs that were stable but had low QYs again, whereas using a PEG ligand resulted in QDs with aggregates present.

Using the ammonia-based ligand exchange with MSA to produce QD-MSA, biomolecules such as the anti-CD63 Ab or aptamer were subsequently attached to the QD-MSA using EDC/NHS coupling. The conjugation was confirmed using DLS, PL, and SPR. The QD-biomolecule was then tested to check for binding to exosomes. SPR was implemented for this, which showed an inhibiting response for the THP exosomes, however, it yielded a binding response to exosomes isolated from the breath and saliva of the author.

Through this, we were able to confirm the binding of the Ab conjugates to those exosomes and confirm the presence of the breath exosomes as well. While saliva, urine, blood, and breast milk are all viable sources of EVs that are disease-related, this work further shows that breath could also be a potential and novel avenue for EVs that can be collected simply through breathing.

5.2 Future outlook

While the technique is very useful, SPR on a commercial instrument is expensive, with the single-use gold slides costing nearly $200 each. In order to be used in more practical applications, the detection of exosomes needs to be instantaneous and widely available. Therefore, it would be beneficial to conduct similar experiments done in this work to smaller home-made setups that can be scaled down and made specific to our application. Designs such as this would mean not having to purchase single-use gold slides, and provide a simpler and sensitive platform to aid

in the development of a rapid detection technology. Along these lines, SPR adapters have begun to be developed for smart-phone platforms, so the results in this thesis could be adapted towards one of these new and interesting technologies.[106] These could result in a more portable and cost-effective SPR system to enable quick and easy analysis for non-specialist end users.[106] This work will also enable more specific analysis of other biomarkers on the membrane of the exosomes that could be targeted using a multiplexed assay and lead to information about their origin and result in the rapid detection of related diseases.[107]

Chapter 4 attempted to prove the binding between the Ab/ QD-Ab and exosome complex. However, there was a reverse trend observed for the cancer-cell derived exosomes using SPR than to what was expected. The breath and saliva-derived exosomes gave rise to an expected trend of increasing response to increasing concentration of the exosomes. Different hypotheses were suggested to the differences in the response trends observed which include a potential difference in surface chemistries, density of CD63 proteins on the membrane or a difference in morphology of the two types of exosomes. These differences could be inherent or due to the difference in isolation methods. Therefore, first and foremost, the experiments should be repeated with a standardised exosome isolation protocol using the qEV size column instead of a precipitation-based kit to explore whether the difference in response is from the isolation. If not, the difference in morphology or surface chemistries can further be explored using a wide array of methods such as DLS, NTA but particularly AFM to probe morphology and surface density. This could further potentially give rise to a new method for the detection of early cancer through the detection of exosomes with specifically different morphology.

With respect to Chapter 2, it would be beneficial to repeat the size dependency and extinction coefficient study by using QDs from the same synthesis protocol. In this thesis, several different synthesis protocols were used, and although they generally resulted in similar molar composition, the differences between them may have complicated this analysis. Two were syntheses that were previously published, which resulted in QDs with emission at 600 nm[53] and 530 nm.[54] The other sizes were obtained using adaptations of these, which made it possible to obtain materials outside of the range of those in the literature. Because the two-pot protocol is very

different, it would be beneficial to examine more sizes using more consistent methods to avoid the inconsistencies arising in the extinction coefficient dependency as well as limiting the factors where errors could arise from.

Additionally, a lot of assumptions were used in the calculation of a concentration for the QDs which included assumptions on their ideal size and shape. This has introduced the inconsistencies and errors in the final results. A more complete study of the concentration and the size dependence would therefore involve minimising the sources of assumptions by using the true size and shape of the QDs.

The problem of lowered QYs, from 25% to 6%, post-ligand exchange was not solved fully. The results of the concentration study in Chapter 2 could further be applied to the ligand exchanges, particularly the multi-step processes, to achieve better understand and control over the ratio of reagents. Hopefully, this would result in higher QYs and better particle stability due to a more complete coverage. The use of PEG-based ligands will also potentially aid in the preservation of the QYs due to their higher coverage.[94]

Appendix A

Appendix: InP/ZnS synthesis methods

A.1 Synthesis of QD-530 and QD-610 nm

The method used to synthesise the QDs emitting at 530 nm and 610 nm have been previously published elsewhere.[54]

Briefly, in a three-neck round-bottom flask containing a temperature probe, a 100 mg of $InCl_3$ are mixed with 100 mg of myristic acid, 10 mL of octadecene and 0.4 mL of trioctylamine. This mixture is put under vacuuum and the temperature is set at 120 °C for 1 hour. After 1 hour, the atmosphere is changed to nitrogen and the temperature is increased to 180 °C. In a separate two-neck round-bottom flask, 300 mg of $ZnCl_2$ was mixed with 3 mL of oleylamine and put under vacuuum for 30 minutes at 120 °C. After this, the temperature was increased to 150 °C and the mixture was put under a nitrogen atmosphere. After this temperature was reached, 0.45 mL of $P(DEA)_3$ was added. After 30 mins, 1 mL of octadecene was added. This mixture was then quickly injected into the three-neck flask mixture. The cores were collected 30 minutes after this. The shelling procedure then continued as was stated in Chapter 2. This makes QDs that fluoresce at 530 nm. For QDs that fluoresce at 610 nm, the hot injection was done at 260 °C instead of 180 °C. Then, the temperature was dropped to 240 °C for 20 minutes, after which the QDs were normally shelled.

A.2 Synthesis of QD-500 nm

131 mg of $In(OAc)_3$, 495 mg of $ZnBr_2$, 492 mg of cetyltrimethylammonium bromide (CTAB), and 5 mL oleylamine were mixed in a three-neck round-bottom and put under vacuum at room temperature for 15 minutes. The temperature was then increased to 120 °C and left to degass for 1 hour. The system was put under nitrogen atmosphere and heated to 180 °C before the swift injection of 0.45 mL $P(DEA)_3$. This was allowed to stir for 20 minutes before undergoing the shelling procedure as above.

A.3 Extinction coefficient data

Samples	# of In	# of Zn	Mol. of In	Mol of Zn
InP-500 nm	30.920	8.492	6.25416E-7	1.71765E-7
InP-530 nm	46.560	20.830	1.76348E-6	7.88926E-7
InP- 600 nm	110.526	7.918	1.32209E-6	9.47079E-8
InP-610 nm	116.118	77.420	6.30631E-7	4.20465E-7
InP/ZnS-500 nm	61.118	119.935	7.92966E-6	2.56173E-5
InP/ZnS-530 nm	88.932	225.362	5.22644E-6	2.09564E-5
InP/ZnS-600 nm	129.209	270.054	7.21184E-6	2.23377E-5
InP/ZnS-610 nm	200.862	417.805	4.20371E-6	1.27339E-5

TABLE A.1: Number of In and Zn calculated and mol of In and Zn measured using AAS

Samples	# of crystals	Absorbance	Extinction coefficent
InP-500 nm	2.02267E-8	0.053	2.62029E+6
InP-530 nm	3.78749E-8	0.267	7.04951E+6
InP- 600 nm	1.19618E-8	0.204	1.70543E+7
InP-610 nm	5.43094E-9	0.059	1.08637E+7
InP/ZnS-500 nm	2.13592E-7	0.23	1.49285E+6
InP/ZnS-530 nm	9.29898E-8	0.158	2.17826E+6
InP/ZnS-600 nm	8.27158E-8	0.726	1.15408E+7
InP/ZnS-610 nm	3.0478E-8	0.144	6.33059E+6

TABLE A.2: Calculation of number of crystals and extinction coefficients

Appendix B

Appendix: Ligand exchange and conjugation

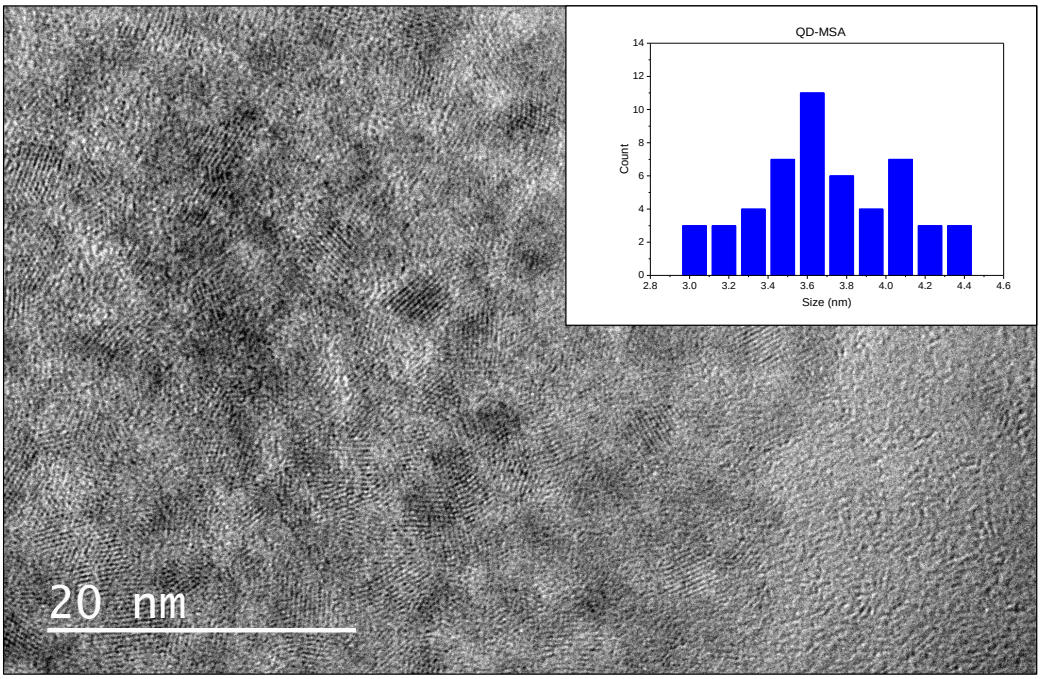

FIGURE B.1: TEM of QD-MSA and size histogram

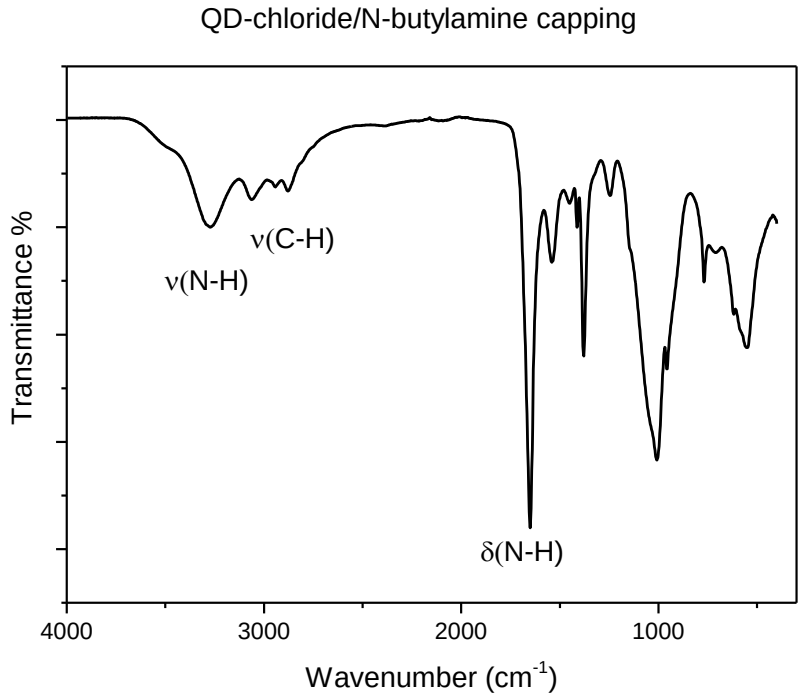

FIGURE B.2: FTIR of QD-chloride/*N*-butylamine

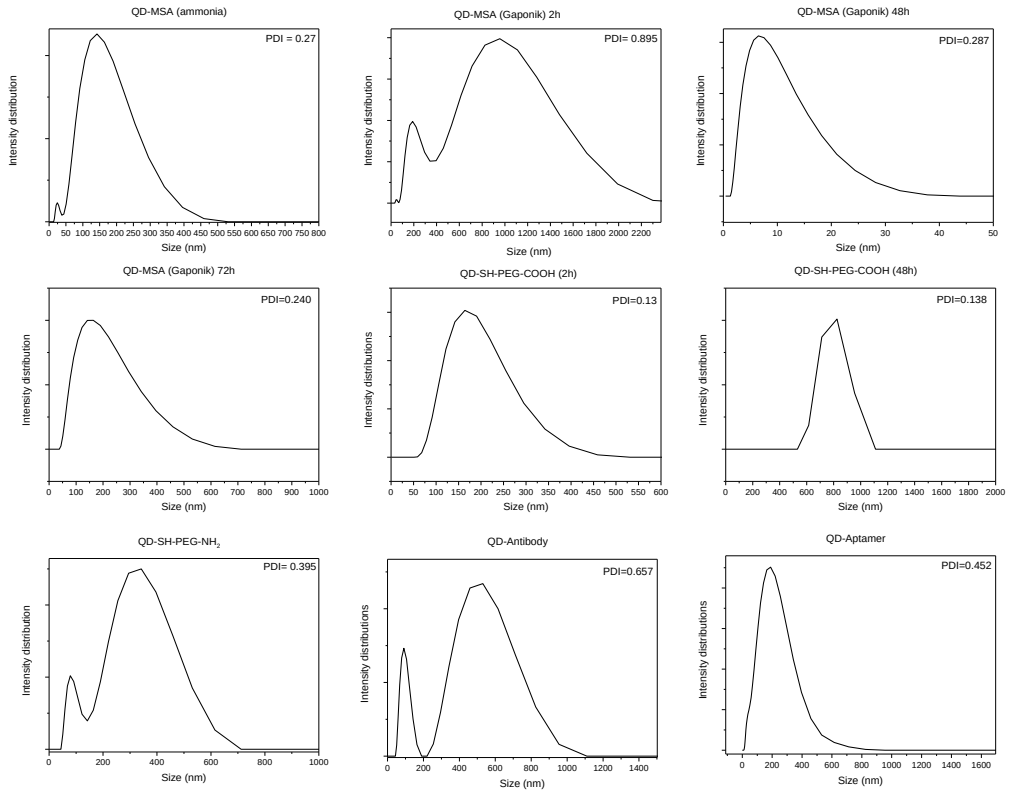

FIGURE B.3: Intensity distributions of all water soluble and conjugated QDs as measured by DLS

Appendix C

Appendix: Breath and saliva exosomes

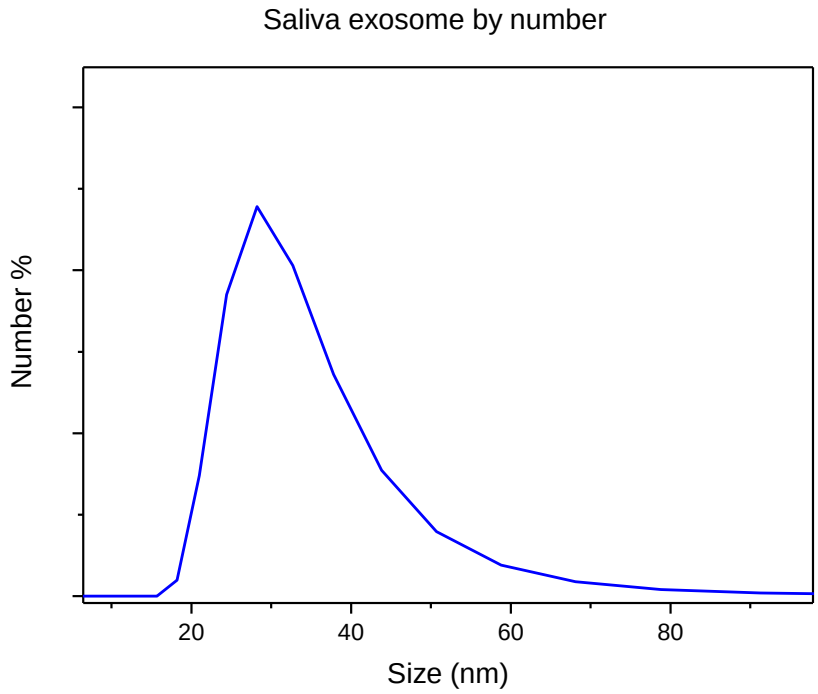

FIGURE C.1: Size as measured by DLS of saliva exosomes

.

.

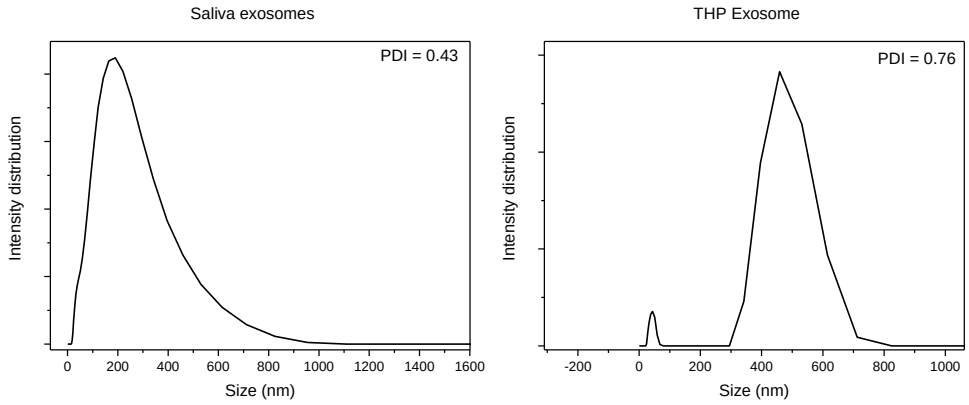

FIGURE C.2: Intensity distribution of saliva and THP exosomes as measured by DLS

Samples	Beads (Intensity/cm^2)	Background (Intensity/cm^2)
Beads	26.62	9.23
QD-Aptamer unwashed	0.63	0.01
QD-Aptamer washed	2.94	0.04
QD-Ab unwashed	9.68	1.00
QD-Ab washed	0.32	0.01
QD-MSA-labelled exosomes	8.24	0.09
QD-MSA SE mixed unwashed	15.91	9.53
QD-MSA SE mixed washed	2.85	0.02
QD-Ab SE unwashed	29.51	0.26
QD-Ab SE washed	37.45	0.05

TABLE C.1: Pixel intensity by area for each sample imaged on the confocal microscope

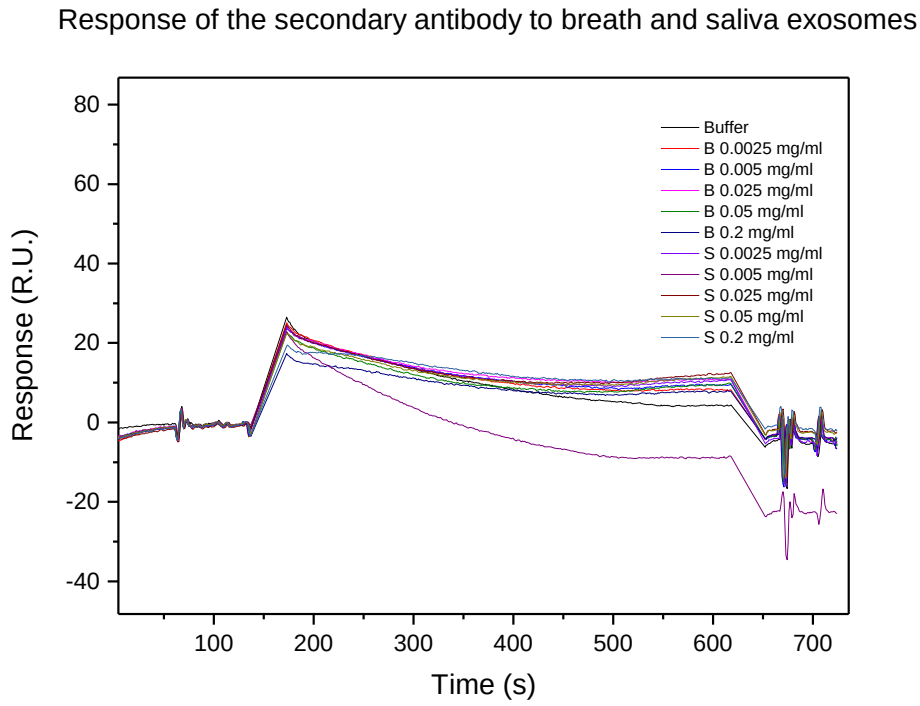

FIGURE C.3: Response of the secondary Ab to breath and saliva exosomes

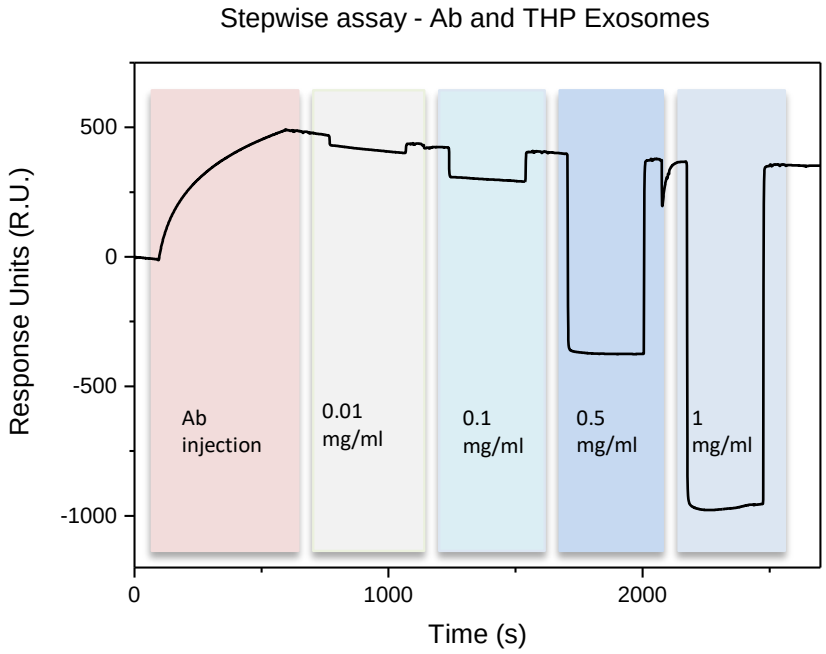

FIGURE C.4: Stepwise assay with injection of Ab first, followed by the injection of different concentrations of exosomes (Denoted with the number). This was conducted on a different gold chip CM5 with longer dextran chains, hence the higher responses.

Bibliography

(1) Goreham, R. V.; Ayed, Z.; Ayupova, D.; Dobhal, G. In *Reference Module in Materials Science and Materials Engineering*; Elsevier: 2018.

(2) Théry, C.; Zitvogel, L.; Amigorena, S. *Nature Reviews Immunology* **Aug. 2002**, *2*, 569.

(3) Vlassov, A. V.; Magdaleno, S.; Setterquist, R.; Conrad, R. Exosomes: Current knowledge of their composition, biological functions, and diagnostic and therapeutic potentials., 2012.

(4) Medintz, I. L.; Uyeda, H. T.; Goldman, E. R.; Mattoussi, H. *Nature Materials* **2005**, DOI: 10.1038/nmat1390.

(5) Andreu, Z. *Frontiers in Immunology* **2014**, *5*, 1–12.

(6) Principe, S.; Hui, A. B.-Y.; Bruce, J.; Sinha, A.; Liu, F.-F.; Kislinger, T. *Proteomics* **2013**, DOI: 10.1002/pmic.201200533.

(7) Muller, L.; Hong, C. S.; Stolz, D. B.; Watkins, S. C.; Whiteside, T. L. *Journal of Immunological Methods* **2014**, 55–65.

(8) Pisitkun, T.; Shen, R.-F.; Knepper, M. A. *PNAS* **2004**, *101*, 13368–13373.

(9) Keller, S.; Rupp, C.; Stoeck, A.; Runz, S.; Fogel, M.; Lugert, S.; Hager, H.-D.; Abdel-Bakky, M.; Gutwein, P.; Altevogt, P. *Kidney International* **2007**, DOI: 10.1038/sj.ki.5002486.

(10) Admyre, C.; Johansson, S. M.; Qazi, K. R.; Filen, J.-J.; Lahesmaa, R.; Norman, M.; Neve, E. P. A.; Scheynius, A.; Gabrielsson, S. *The Journal of Immunology* **2007**, *179*, 1969–1978.

(11) Michael, A.; Bajracharya, S. D.; Yuen, P. S.; Zhou, H.; Star, R. A.; Illei, G. G.; Alevizos, I. *Oral Diseases* **2009**, *16*, 34–38.

(12) Lau, C.; Kim, Y.; Chia, D.; Spielmann, N.; Eibl, G.; Elashoff, D.; Wei, F.; Lin, Y. L.; Moro, A.; Grogan, T.; Chiang, S.; Feinstein, E.; Schafer, C.; Farrell, J.; Wong, D. T. W. *The Journal of biological chemistry* **2013**, *288*, 26888–26897.

(13) Raposo, G.; Stoorvogel, W. *Journal of Cell Biology* **2013**, *200*, 373–383.

(14) Witwer, K. W.; Buzás, E. I.; Bemis, L. T.; Bora, A.; Lässer, C.; Lötvall, J.; Nolte-'t Hoen, E. N.; Piper, M. G.; Sivaraman, S.; Skog, J.; Théry, C.; Wauben, M. H.; Hochberg, F. *Journal of Extracellular Vesicles* **2013**, *2*, 20360.

(15) Pinkerton, M. B.; Chinchilli, V.; Banta, E.; Craig, T. D.; August, A.; Bascom, R.; Cantorna, M.; Harvill, E.; Ishmael, F. T. *Journal of Allergy and Clinical Immunology* **2013**, *132*, 217–219.

(16) Mozzoni, P.; Banda, I.; Goldoni, M.; Corradi, M.; Tiseo, M.; Acampa, O.; Balestra, V.; Ampollini, L.; Casalini, A.; Carbognani, P.; Mutti, A. *Biomarkers* **2013**, *18*, 679–686.

(17) Sinha, A.; Yadav, A. K.; Chakraborty, S.; Kabra, S.; Lodha, R.; Kumar, M.; Kulshreshtha, A.; Sethi, T.; Malik, G.; Pandey, R.; Laddha, S.; Mukhopadhyay, A.; Dash, D.; Balaram, G.; Agrawal, A. *Journal of Allergy and Clinical Immunology* **2013**, *132*, 219–221.

(18) Helwa, I.; Cai, J.; Drewry, M. D.; Zimmerman, A.; Dinkins, M. B.; Khaled, M. L.; Seremwe, M.; Dismuke, W. M.; Bieberich, E.; Stamer, W. D.; Hamrick, M. W.; Liu, Y. *Plos One* **Jan. 2017**, *12*, e0170628.

(19) Böing, A. N.; van der Pol, E.; Grootemaat, A. E.; Coumans, F. A. W.; Sturk, A.; Nieuwland, R. *Journal of extracellular vesicles* **Sept. 2014**, *3*, 10.3402/jev.v3.23430.

(20) Konoshenko, M. Y.; Lekchnov, E. A.; Vlassov, A. V.; Laktionov, P. P. Isolation of Extracellular Vesicles: General Methodologies and Latest Trends., 2018.

(21) Lee, J.; Yoon, Y. J.; Kim, J. H.; Dinh, N. T. H.; Go, G.; Tae, S.; Park, K.-S.; Park, H. T.; Lee, C.; Roh, T.-Y.; Di Vizio, D.; Gho, Y. S. *Frontiers in Microbiology* **2018**, *9*, 2268.

(22) Sharma, S.; Gillespie, B. M.; Palanisamy, V.; Gimzewski, J. K. *Langmuir* **Dec. 2011**, *27*, 14394–14400.

(23) Rupert, D. L. M.; Lässer, C.; Eldh, M.; Block, S.; Zhdanov, V. P.; Lotvall, J. O.; Bally, M.; Höök, F. *Analytical Chemistry* **June 2014**, *86*, 5929–5936.

(24) Van Der Pol, E.; Hoekstra, A. G.; Sturk, A.; Otto, C.; Van Leeuwen, T. G.; Nieuwland, R. *Journal of Thrombosis and Haemostasis* **2010**, *8*, 2596–2607.

(25) Rupert, D. L. M.; Claudio, V.; Lässer, C.; Bally, M. *BBA - General Subjects* **2017**, *1861*, 3164–3179.

(26) Stoner, S. A.; Duggan, E.; Condello, D.; Guerrero, A.; Turk, J. R.; Narayanan, P. K.; Nolan, J. P. *Journal of the International Society for Advancement of Cytometry* **2015**, *89A*, 196–206.

(27) Oliveira-Rodríguez, M.; Serrano-Pertierra, E.; García, A. C.; López-Martín, S.; Yañez-Mo, M.; Cernuda-Morollón, E.; Blanco-López, M. *Biosensors and Bioelectronics* **Jan. 2017**, *87*, 38–45.

(28) Palmieri, V.; Lucchetti, D.; Gatto, I.; Maiorana, A.; Marcantoni, M.; Maulucci, G.; Papi, M.; Pola, R.; De Spirito, M.; Sgambato, A. *Journal of Nanoparticle Research* **2014**, DOI: 10.1007/s11051-014-2583-z.

(29) Chernyshev, V. S.; Rachamadugu, R.; Tseng, Y. H.; Belnap, D. M.; Jia, Y.; Branch, K. J.; Butterfield, A. E.; Pease, L. F.; Bernard, P. S.; Skliar, M. *Analytical and Bioanalytical Chemistry* **2015**, DOI: 10.1007/s00216-015-8535-3.

(30) Hong-Qiang Li The Common AFM Modes., 1997.

(31) Sharma, S.; Rasool, H. I.; Palanisamy, V.; Mathisen, C.; Schmidt, M.; Wong, D. T.; Gimzewski, J. K. *ACS Nano* **2010**, DOI: 10.1021/nn901824n.

(32) Sina, A. A. I.; Vaidyanathan, R.; Dey, S.; Carrascosa, L. G.; Shiddiky, M. J. A.; Trau, M. *Scientific Reports* **2016**, *6*, 30460.

(33) Boriachek, K.; Islam, M. N.; Gopalan, V.; Lam, A. K.; Nguyen, N.-T.; Shiddiky, M. J. A. *The Analyst* **2017**, DOI: 10.1039/C7AN00672A.

(34) Yang, L.; Zhang, X.; Ye, M.; Jiang, J.; Yang, R.; Fu, T.; Chen, Y.; Wang, K.; Liu, C.; Tan, W. *Advanced Drug Delivery Reviews* **2011**, *63*, 1361–1370.

(35) Nimjee, S. M.; White, R. R.; Becker, R. C.; Sullenger, B. A. *Annual Review of Pharmacology and Toxicology* **2017**, DOI: 10.1146/annurev-pharmtox-010716-104558.

(36) Jo, H.; Ban, C. *Experimental & molecular medicine* **2016**, *48*, e230.

(37) Jiang, Y.; Shi, M.; Liu, Y.; Wan, S.; Cui, C.; Zhang, L.; Tan, W. *Angewandte Chemie International Edition* **Aug. 2017**, *56*, 11916–11920.

(38) Bilan, R.; Fleury, F.; Nabiev, I.; Sukhanova, A. *Bioconjugate Chemistry* **2015**, *26*, 609–624.

(39) Hines, M. A.; Sionnest-Guyot, P. *The Journal of Physical Chemistry.* **1996**, *100*, 468–471.

(40) Hildebrandt, N.; Spillmann, C. M.; Algar, W. R.; Pons, T.; Stewart, M. H.; Oh, E.; Susumu, K.; Díaz, S. A.; Delehanty, J. B.; Medintz, I. L. *Chemical Reviews* **Jan. 2017**, *117*, 536–711.

(41) Yong, K. T.; Ding, H.; Roy, I.; Law, W. C.; Bergey, E. J.; Maitra, A.; Prasad, P. N. *ACS Nano* **2009**, *3*, 502.

(42) Ag, D.; Bongartz, R.; Dogan, L. E.; Seleci, M.; Walter, J. G.; Demirkol, D. O.; Stahl, F.; Ozcelik, S.; Timur, S.; Scheper, T. *Colloids and Surfaces B: Biointerfaces* **2014**, DOI: 10.1016/j.colsurfb.2013.09.033.

(43) Dwarakanath, S.; Bruno, J. G.; Shastry, A.; Phillips, T.; John, A.; Kumar, A.; Stephenson, L. D. *Biochemical and Biophysical Research Communications* **2004**, *325*, 739–743.

(44) Satarug, S.; Moore, M. R. *Environmental health perspectives* **July 2004**, *112*, 1099–1103.

(45) Liu, W.; Hak, S. C.; Zimmer, J. P.; Tanaka, E.; Frangioni, J. V.; Bawendi, M. *Journal of the American Chemical Society* **2007**, *129*, 14530–14531.

(46) Brunetti, V.; Chibli, H.; Fiammengo, R.; Galeone, A.; Malvindi, M. A.; Vecchio, G.; Cingolani, R.; Nadeau, J. L.; Pompa, P. P. *Nanoscale* **2013**, *5*, 307–317.

(47) Yang, J. L. *Biological Research* **2014**, *47*, 2–5.

(48) Park, H.; Park, Y.; Kim, W.; Choi, W. *Journal of Photochemistry and Photobiology C: Photochemistry Reviews* **2013**, *15*, 1–20.

(49) Allen, P.; Walker, B.; Bawendi, M. *Angewandte Chemie International Edition* **Jan. 2010**, *49*, 760–762.

(50) Li, L.; Reiss, P. *J. Am. Chem. Soc.* **2008**, *130*, 11588–11589.

(51) Vinokurov, A. A.; Dorofeev, S. G.; Znamenkov, K. O.; Panfilova, A. V.; Kuznetsova, T. A. *Mendeleev Communications* **2010**, *20*, 31–32.

(52) Song, W.-S.; Lee, H.-S.; Lee, J. C.; Jang, D. S.; Choi, Y.; Choi, M.; Yang, H. *Journal of Nanoparticle Research* **2013**, *15*, 1750.

(53) Tessier, M. D.; Dupont, D.; De Nolf, K.; De Roo, J.; Hens, Z. *Chemistry of Materials* **2015**, *27*, 4893–2898.

(54) Laufersky, G.; Bradley, S.; Frécaut, E.; Lein, M.; Nann, T. *Nanoscale* **2018**, *10*, 8752–8762.

(55) Smith, A. M.; Duan, H.; Rhyner, M. N.; Ruan, G.; Nie, S. *Physical Chemistry Chemical Physics* **2006**, *8*, 3895.

(56) Dai, M. Q.; Yung, L. Y. L. *Chemistry of Materials* **2013**, DOI: 10.1021/cm304136a.

(57) Dong, A.; Ye, X.; Chen, J.; Kang, Y.; Gordon, T.; Kikkawa, J. M.; Murray, C. B. *J. Am. Chem. Soc* **2011**, *133*, 998–1006.

(58) Liu, D.; Snee, P. T. *ACS Nano* **Jan. 2011**, *5*, 546–550.

(59) Pong, B.-k.; Trout, B. L.; Lee, J.-y. **2008**, 5270–5276.

(60) Boles, M. A.; Ling, D.; Hyeon, T.; Talapin, D. V. *Nature Materials* **2016**, *15*, 364–364.

(61) Dewi, M. R.; Skinner, W. M.; Nann, T. *Australian Journal of Chemistry* **2014**, *67*, 663.

(62) Rosen, E. L.; Buonsanti, R.; Llordes, A.; Sawvel, A. M.; Milliron, D. J.; Helms, B. A. *Angewandte Chemie - International Edition* **2012**, *51*, 684–689.

(63) Sayevich, V.; Gaponik, N.; Plötner, M.; Kruszynska, M.; Gemming, T.; Dzhagan, V. M.; Akhavan, S.; Zahn, D. R. T.; Demir, H. V.; Eychmüller, A. *Chemistry of Materials* **2015**, *27*, 4328–4337.

(64) Sayevich, V.; Guhrenz, C.; Dzhagan, V. M.; Sin, M.; Werheid, M.; Cai, B.; Borchardt, L.; Widmer, J.; Zahn, D. R.; Brunner, E.; Lesnyak, V.; Gaponik, N.; Eychmüller, A. *ACS Nano* **2017**, *11*, 1559–1571.

(65) Guhrenz, C.; Sayevich, V.; Weigert, F.; Hollinger, E.; Reichhelm, A.; Resch-Genger, U.; Gaponik, N.; Eychmüller, A. *The Journal of Physical Chemistry Letters* **Nov. 2017**, *8*, 5573–5578.

(66) Montenegro, J.-M.; Grazu, V.; Sukhanova, A.; Agarwal, S.; de la Fuente, J. M.; Nabiev, I.; Greiner, A.; Parak, W. J. *Advanced Drug Delivery Reviews* **2013**, *65*, 677–688.

(67) East, D. A.; Mulvihill, D. P.; Todd, M.; Bruce, I. J. *Langmuir* **2011**, *27*, 13888–13896.

(68) Zrazhevskiy, P.; Gao, X. *Nature Communications* **2013**, *4*, 1619.

(69) Jaiswal, J. K.; Mattoussi, H.; Mauro, J. M.; Simon, S. M. *Nature Biotechnology* **2002**, *21*, 47–51.

(70) Yu, J.; Su, J.; Zhang, J.; Wei, X.; Guo, A. *RSC Adv.* **2017**, *7*, 17819–17823.

(71) Suzuki, M.; Udaka, H.; Fukuda, T. *Journal of Pharmaceutical and Biomedical Analysis* **2017**, *143*, 110–115.

(72) Bagalkot, V; Zhang, L; Levy-Nissenbaum, E; Jon, S; Kantoff, P. W.; Langer, R; Farokhzad, O. C. *Nano Letters* **2007**, *7*, 3065–3070.

(73) Madhankumar, A. B.; Mrowczynski, O. D.; Patel, S. R.; Weston, C. L.; Zacharia, B. E.; Glantz, M. J.; Siedlecki, C. A.; Xu, L.-C.; Connor, J. R. *Acta Biomaterialia* **2017**, *58*, 205–213.

(74) Yang, X.; Zhao, D.; Leck, K. S.; Tan, S. T.; Tang, Y. X.; Zhao, J.; Demir, H. V.; Sun, X. W. *Advanced Materials* **Apr. 2012**, *24*, 4180–4185.

(75) Shen, Y.; Tan, R.; Gee, M. Y.; Greytak, A. B. *ACS Nano* **Mar. 2015**, *9*, 3345–3359.

(76) King, L. A.; Riley, D. J. *The Journal of Physical Chemistry C* **Feb. 2012**, *116*, 3349–3355.

(77) Hassinen, A.; Moreels, I.; De Nolf, K.; Smet, P. F.; Martins, J. C.; Hens, Z. *Journal of the American Chemical Society* **Dec. 2012**, *134*, 20705–20712.

(78) Shen, Y.; Gee, M. Y.; Tan, R.; Pellechia, P. J.; Greytak, A. B. *Chemistry of Materials* **July 2013**, *25*, 2838–2848.

(79) Kim, K.; Yoo, D.; Choi, H.; Tamang, S.; Ko, J.-H.; Kim, S.; Kim, Y.-H.; Jeong, S. *Angewandte Chemie International Edition* **Feb. 2016**, *55*, 3714–3718.

(80) Schmelz, O.; Mews, A.; Basché, T.; Herrmann, A.; Müllen, K. *Langmuir* **May 2001**, *17*, 2861–2865.

(81) Yu, W. W.; Qu, L.; Guo, W.; Peng, X. *Chemistry of Materials* **July 2003**, *15*, 2854–2860.

(82) Booth, M.; Brown, A. P.; Evans, S. D.; Critchley, K. *Chemistry of Materials* **June 2012**, *24*, 2064–2070.

(83) Kuçur, E.; Boldt, F. M.; Cavaliere-Jaricot, S.; Ziegler, J.; Nann, T. *Analytical Chemistry* **Dec. 2007**, *79*, 8987–8993.

(84) Baskoutas, S.; Terzis, A. F. *Journal of Applied Physics* **Jan. 2006**, *99*, 013708.

(85) Cho, E.; Jang, H.; Lee, J.; Jang, E. *Nanotechnology* **May 2013**, *24*, 215201.

(86) Dong, A.; Yu, H.; Wang, F.; Buhro, W. E. *Journal of the American Chemical Society* **May 2008**, *130*, 5954–5961.

(87) Wang, L.-W.; Li, J. *Physical Review B* **Apr. 2004**, *69*, 153302.

(88) Gill, R.; Willner, I.; Shweky, I.; Banin, U. *The Journal of Physical Chemistry B* **Dec. 2005**, *109*, 23715–23719.

(89) Stsiapura, V.; Sukhanova, A.; Baranov, A.; Artemyev, M.; Kulakovich, O.; Oleinikov, V.; Pluot, M.; Cohen, J. H. M.; Nabiev, I. *Nanotechnology* **Jan. 2006**, *17*, 581–587.

(90) Zhang, B.; Hu, R.; Wang, Y.; Yang, C.; Liu, X.; Yong, K.-T. *RSC Advances* **2014**, *4*, 13805–13816.

(91) Bharali, D. J.; Lucey, D. W.; Jayakumar, H.; Pudavar, H. E.; Prasad, P. N. *Journal of the American Chemical Society* **Aug. 2005**, *127*, 11364–11371.

(92) Tamang, S.; Beaune, G.; Texier, I.; Reiss, P. *ACS Nano* **Dec. 2011**, *5*, 9392–9402.

(93) Cordero, S. R.; Carson, P. J.; Estabrook, R. A.; Strouse, G. F.; Buratto, S. K. *The Journal of Physical Chemistry B* **Dec. 2000**, *104*, 12137–12142.

(94) Wenger, W. N.; Bates, F. S.; Aydil, E. S. *Langmuir* **Aug. 2017**, *33*, 8239–8245.

(95) Xu, S.; Ziegler, J.; Nann, T. *J. Mater. Chem.* **2008**, *18*, 2653–2656.

(96) Berg, J. C., *An introduction to interfaces & colloids : the bridge to nanoscience / John C. Berg.* Singapore: Singapore, 2010.

(97) Dobhal, G.; Ayupova, D.; Laufersky, G.; Ayed, Z.; Nann, T.; Goreham, R. V. *Sensors* **2018**, *18*, DOI: 10.3390/s18103308.

(98) Trilling, A. K.; Beekwilder, J.; Zuilhof, H. *Analyst* **2013**, *138*, 1619–1627.

(99) Han, H.-S.; Niemeyer, E.; Huang, Y.; Kamoun, W. S.; Martin, J. D.; Bhaumik, J.; Chen, Y.; Roberge, S.; Cui, J.; Martin, M. R.; Fukumura, D.; Jain, R. K.; Bawendi, M. G.; Duda, D. G. *Proceedings of the National Academy of Sciences* **Feb. 2015**, *112*, 1350 LP –1355.

(100) Wang, H.; Wang, X.; Wang, J.; Fu, W.; Yao, C. *Scientific Reports* **Sept. 2016**, *6*, 33140.

(101) Weichelt, R.; Leubner, S.; Henning-Knechtel, A.; Mertig, M.; Gaponik, N.; Schmidt, T.-L.; Eychmüller, A. *Small* **July 2016**, *12*, 4763–4771.

(102) Xing, Y.; So, M.-K.; Koh, A. L.; Sinclair, R.; Rao, J. *Biochemical and biophysical research communications* **Aug. 2008**, *372*, 388–394.

(103) Kim, C.; Galloway, J. F.; Lee, K. H.; Searson, P. C. *Bioconjugate Chemistry* **Oct. 2014**, *25*, 1893–1901.

(104) Tang, Y.; Zeng, X.; Liang, J. *Journal of Chemical Education* **July 2010**, *87*, 742–746.

(105) Grasso, L.; Wyss, R.; Weidenauer, L.; Thampi, A.; Demurtas, D.; Prudent, M.; Lion, N.; Vogel, H. *Analytical and bioanalytical chemistry* **2015**, *407*, 5425–5432.

(106) Liu, Y.; Liu, Q.; Chen, S.; Cheng, F.; Wang, H.; Peng, W. *Scientific Reports* **Aug. 2015**, *5*, 12864.

(107) Ming, K.; Kim, J.; Biondi, M. J.; Syed, A.; Chen, K.; Lam, A.; Ostrowski, M.; Rebbapragada, A.; Feld, J. J.; Chan, W. C. W. *ACS Nano* **2015**, *9*, 3060–3074.